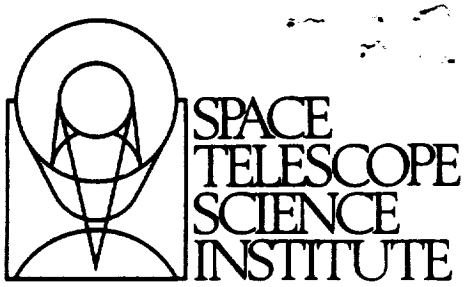

P 114

Hubble Space Telescope

Faint Object Camera Instrument Handbook

Version 2.0

May 1990

Revision History

Handbook Version 1.0	October 1985; edited by Francesco Paresce
Supplement to Version 1.0	May 1989; edited by Francesco Paresce
Handbook Version 2.0	May 1990; edited by Francesco Paresce

The Space Telescope Science Institute is operated by the Association of Universities for Research in Astronomy, Inc., for the National Aeronautics and Space Administration.

FAINT OBJECT CAMERA
INSTRUMENT HANDBOOK

Francesco Paresce
Space Telescope Science Institute
3700 San Martin Drive
Baltimore, MD 21218
and
Astrophysics Division, Space Science Department of ESA,
ESTEC, Noordwijk, Holland

Version 2.0

May 1990

CONTENTS

LIST OF FIGURES

LIST OF TABLES

1.0 INTRODUCTION

The Faint Object Camera (FOC) is a long focal ratio, photon counting device designed to take high resolution two dimensional images of areas of the sky up to 44 by 44 arcseconds squared in size with pixel dimensions as small as 0.007 by 0.007 arcseconds squared in the 1150 to 6500Å wavelength range. Its performance approaches that of an ideal imaging system at low light levels and it will be the only instrument on board HST to fully utilize the unprecedented spatial resolution capabilities of the Optical Telescope Assembly (OTA). The FOC is one of the European Space Agency's contributions to the HST program.

The two prime purposes of the FOC are deep imagery and photometry of very faint celestial objects and imagery of bright objects at the highest possible resolution available from HST. In principle, the FOC is capable of detecting a star of blue magnitude 30 in a 10 hour exposure with a S/N = 5 and to resolve bright sources in the far UV up to an effective angular resolution of $\simeq$0.015 arcseconds.

The main scientific objectives of the FOC include, but are not restricted to, the study of the physics of planets, search for planets and proto-planetary condensations around nearby stars, search for massive black holes in globular clusters, study of the ionization structure of shock waves in the interstellar medium, high spatial resolution studies of very young stars and cataclysmic variables and their interaction with the surrounding interstellar medium, measurements of distances to the Coma Cluster galaxies, the study of stellar content of globular clusters, observation of optical emission associated with radio lobes and jets in galaxies, the observations of velocity dispersion and mass densities in the central regions of normal and compact elliptical galaxies, observation of extended structure around QSOs at high spatial resolution, and the study of gravitational lenses.

The basic aim of this handbook is to make relevant information about the FOC available to a wide group of astronomers, many of whom may wish to apply for HST observing time. It should also help astronomers all over the world to think realistically about preparing for such observations. The FOC, as presently configured, is briefly described and some basic performance parameters summarized in section 2. A more detailed, in-depth perspective on the FOC can be found in section 3. This plan should allow readers to choose the level of detail required to match their previous degree of understanding of the instrument with the degree of complexity of the proposed observing program.

Consequently, users already familiar with the FOC may wish to pass directly to section 3 for the finer points. Others may wish to read section 2 carefully either solely to refresh their memory or to get a general overview and then pass directly to sections 4 and 5. Here the readers will find the detailed FOC performance parameters and instructions on how to derive approximate FOC exposure times for the proposed targets and some useful examples. The last section deals with the expected data products and calibration plans.

2.0 INSTRUMENT OVERVIEW

The Faint Object Camera (FOC) is one of the four axial scientific instruments sharing the HST focal plane. It is located in the −V2, −V3 quadrant (see Figure 5), has overall dimensions of 0.9×0.9 × 2.2 meters, weighs 320 kg and consumes 150W of power on average in operation. An overall operational and data flow block diagram of the instrument is shown in Figure 1 with the FOC itself contained within the dashed line. Radiation from an astronomical source focussed onto the OTA focal plane can be fed into either of two separate and independent cameras each with its own entrance aperture, imaging optics and detector system. One camera magnifies the image on the OTA focal plane by a factor of two to an effective focal ratio of F/48 while the other magnifies the focal plane by a factor of either four or twelve to effective focal ratios of F/96 and F/288, respectively. This transfer is accomplished mainly in order to match the OTA resolution performance with the available detector pixel size.

Each optical relay consists of segments of a full optical figure of revolution the axis of which is perpendicular to the OTA focal plane at the FOC entrance aperture location. Both cameras have the same overall length and operate at the same distance from the OTA optical axis. The re-imaging optics transfers the OTA image onto the photocathode of a photon counting detector with negligible spherical aberration or coma and corrects for the residual OTA off-axis astigmatism. The FOC optical system also provides means for dispersing, filtering, attenuating, polarizing and focussing the image formed by the OTA and for in-flight calibration of the relative and absolute response in the visible.

All the optical elements and both detectors are supported on an optical bench which is rigidly connected to the focal-plane structure of the OTA and is contained within the load-carrying structure which also provides a light-tight enclosure. To meet the image stability requirements, the internal surfaces of the load-carrying structure which enclose the optical bench are actively thermally controlled during an exposure with a stability of better than 0.5° C. An exploded schematic view of the FOC is presented in Figure 2.

The two detectors are two dimensional photon counting devices of identical design. Each consists of a three-stage image intensifier which is optically coupled by a relay lens system to an Electron Bombarded Silicon Target (EBS) TV tube. The tube detects scintillations at the output of the intensifier corresponding to the arrival of individual photons at the first stage photocathode. The central x-y position of each burst of visible light is measured by a dedicated video processing unit (VPU) and a memory location in the scientific data store (SDS) unit associated with that position is incremented by one. At the end of the exposure, the accumulated image in the SDS is sent directly out of the FOC to a dedicated unit in the ST Scientific Instrument Control and Data Handling (SI C&DH) subsystem which consists of a computer with a reprogrammable non-volatile memory. The two detectors on the ground produce a dark noise of $\simeq 1\text{–}5{\cdot}10^{-4}$ counts sec^{-1} pixel^{-1}.

The SDS storage capacity is adapted to an image area of 512 × 512 resolution elements and provides a 16 bit data word for each pixel. This results in a memory capacity of 256K words of 16 bits each or 0.5 Mbyte in total. The word length can also be commanded to 8 bits to store data in a 512 × 1024 pixel format with reduced dynamic range. Because of operational constraints, a time interval of at least 3.7 minutes must elapse between the end of an exposure and the start of the next.

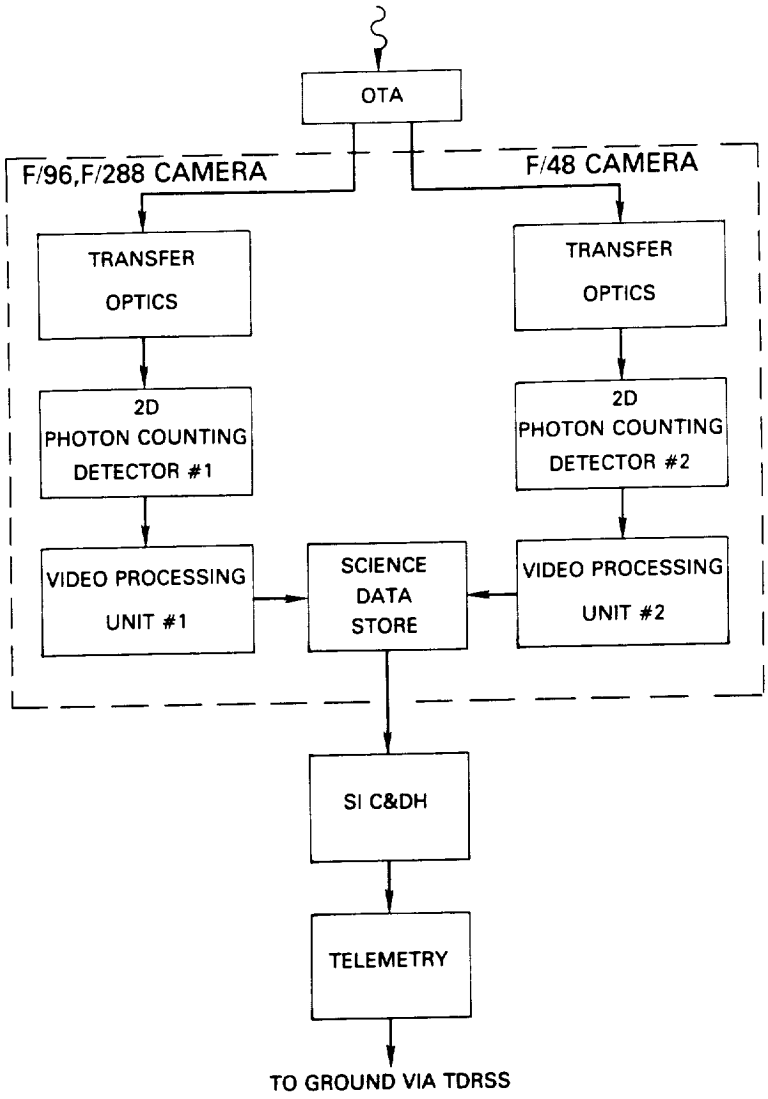

Figure 1. FOC Operational and Data Flow Block Diagram

The detectors are sensitive to radiation between 1150 and 6500Å; the lower limit being set by the MgF_2 input window and the upper limit by the bialkali photocathode material. The useful photocathode area is 40 millimeters in diameter while the size of an independent resolution element (pixel) is on average normally $\simeq$ 24 × 24 microns squared but one dimension can be stretched (zoomed) to $\simeq$ 48 microns. The longer pixel dimension is in the TV frame scan direction and perpendicular to the dispersion direction of all but one (the FOPCD) of the dispersing elements. The plate scales for the F/48, F/96 and F/288 relays are 1.792, 0.896, and 0.299 arcseconds mm^{-1}, respectively.

These parameters, coupled to the quoted maximum SDS capacity, imply that the F/48 camera has a maximum achievable field of view of $\simeq$ 44 × 44 arcseconds squared imaged at an angular resolution of 0.086 × 0.043 arcseconds squared (512 zoomed × 1024, 48 × 24

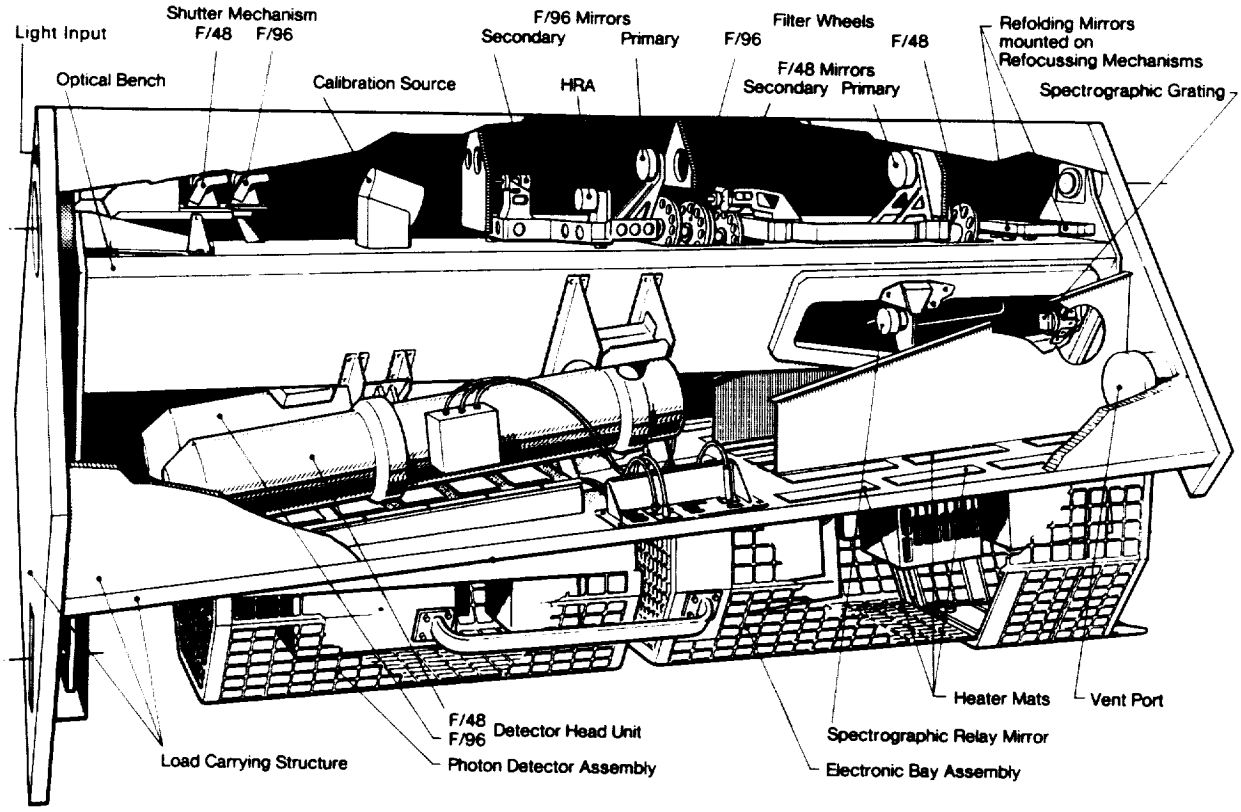

Figure 2. Schematic Drawing of the FOC

micron squared pixels with 8 bit words). The corresponding values for the F/96 relay are $\simeq$ 22 $\times$ 22 and 0.044 $\times$ 0.022 arcseconds squared and for the F/288 relay $\simeq$ 7.3 $\times$ 7.3 and 0.015 $\times$ .0072 arcseconds squared. Smaller fields can be imaged at higher spatial resolution and extended dynamic range (see Table 4 for a partial list).

In summary, the key operating features of the FOC are its low noise, high angular resolution, high sensitivity in the UV range and extreme versatility due to its occultation, apodization, long slit spectroscopic, polarization, objective prism and cross dispersion capabilities. Its most significant limitations, on the other hand, are its relatively small field of view and the non-linearity of response at high count rates which limits its application to objects yielding less than $\simeq$ 10 counts sec^{-1} pixel^{-1} corresponding to a $B \simeq 20$ A0V star observed through the F430W filter, for example. A summary of the most important performance characteristics of the FOC as presently known is given in Tables 1 and 2 for the imaging and spectrographic modes, respectively.

Table 1.
Summary of FOC Performance Characteristics I. Imaging

Optical Modes:	F/48	F/96	F/288
Operating Range (Å):	1150-6500	1150-6500	1150-6500
Number of Bandpass Filters:	11	39	39
Bandpass FWHM (Å) Max:	2700	2600	2600
Min.	300	34	34
Maximum ND attenuation (mag.):	0	9	9
Field of View (arcsec) Max:	44 × 44	22 × 22	7.3 × 7.3
Field of View (arcsec) Min:	5.5 × 5.5	2.8 × 2.8	0.9 × 0.9
Unzoomed Pixel Size (arcsec):	0.044	0.022	0.007
Minimum Wavelength for Critical Sampling (Å):	10400	5200	1700
Maximum Achievable Spatial Resolution (mas):	150	50	20
Peak Efficiency (%):	8.1	10.4	7.0
Peak Wavelength (Å):	3100	3100	3900
Limiting Magnitude, Point Source[1]:	30	30	29
Limiting Magnitude Arcsec^{-2}, Extended Source[2]:	25.5	25.5	24.5
Maximum Achievable S/N:	400	400	400
Dynamic Range, Point Source[3] (mag):	22-28	21-30	18.5-29
Dynamic Range, Extended Source[4] (mag arcsec^{-2})	18.5-25.5	17.5-25.5	14.5-24.5
Overload Magnitude:	9	9	9
Number of Polarizing Prisms[5]:	0	3	3

1. S/N = 5, 3 hour integration, U band. pixel^{-1} upper limit
2. Same as 1. over $0.1'' \times 0.1''$ area
3. 5 counts s^{-1} pixel^{-1} upper limit
4. 0.5 counts s^{-1}
5. 0°, 60° and 120° directions of polarization

Table 2. Summary of FOC Performance Characteristics II. Spectroscopy

Spectral Modes:	F/48-FUVOP	F/48-NUVOP	F/96-FUVOP	F/96-NUVOP	F/48-SP	F/48 SP-CD	F/48 SP-SS
Operating Range (Å):	1250-3000	1700-4000	1150-3000	1700-4000	3600-5400(1) 1800-2700(2) 1200-1800(3) 1150-1350(4)	3600-5400(1) 1800-2700(2) 1200-1800(3) 1150-1350(4)	3300-5100(1) 1650-2550(2) 1150-1700(3) 1150-1350(4)
Maximum Field of View (arcsec):	44 × 44	44 × 44	22 × 22	22 × 22	20 × 0.1	20 × 0.1	35 × 15
Number of Bandpass or Order Sorting Filters Available:	11	11	39	39	11	11	11
Number of ND Filters Available:	0	0	9	9	0	0	0
Spatial resolution (arcsec):	0.15	0.15	0.05	0.05	0.1 × 0.15	0.1 × 0.15	0.15
Resolving Power: Wavelength (Å):	50 1500	100 2500	50 1500	100 2500	1150 (1)-(4)	1150 (1)-(4)	1150 (1)-(4)
Spectrum Length (pix):	55	90	160	450	1024	1024	850
Spectrum Width (pix):	2	2	4	4	≤ 450	≤ 450	≤ 350
Maximum Spectral Resolution (Å):	10	21	5	14	4 (1) 2 (2) 1.3(3) 1.0(4)	4 (1) 2 (2) 1.3(3) 1.0(4)	4 (1) 2 (2) 1.3(3) 1.0(4)
Peak Efficiency (%):	7.8	7.1	10.0	9.4	1.5 (1) 0.82(2) 0.25(3) 0.20(4)	1.5 (1) 0.76(2) 0.21(3) 0.12(4)	1.5 (1) 0.82(2) 0.25(3) 0.20(4)
Limiting Flux, Point Source[1] (ergs cm^{-2} s^{-1})	$2 \cdot 10^{-16}$	$5 \cdot 10^{-17}$	$2 \cdot 10^{-16}$	$5 \cdot 10^{-17}$	$8 \cdot 10^{-17}$(1) $3 \cdot 10^{-16}$(2) $2 \cdot 10^{-15}$(3) $3 \cdot 10^{-15}$(4)	$8 \cdot 10^{-17}$(1) $4 \cdot 10^{-16}$(2) $3 \cdot 10^{-15}$(3) $4 \cdot 10^{-15}$(4)	$4 \cdot 10^{-17}$(1) $2 \cdot 10^{-16}$(2) $1 \cdot 10^{-15}$(3) $2 \cdot 10^{-15}$(4)
Limiting Flux, Extended Source[2] (ergs cm^{-2} s^{-1} $arcsec^{-2}$):	$2 \cdot 10^{-14}$	$4 \cdot 10^{-15}$	$5 \cdot 10^{-14}$	10^{-14}	10^{-14} (1) $5 \cdot 10^{-14}$(2) $3 \cdot 10^{-13}$(3) $4 \cdot 10^{-13}$(4)	10^{-14} (1) $6 \cdot 10^{-14}$(2) $4 \cdot 10^{-14}$(3) $5 \cdot 10^{-14}$(4)	$5 \cdot 10^{-15}$(1) 10^{-14} (2) $2 \cdot 10^{-13}$(3) $2 \cdot 10^{-13}$(4)

1. S/N = S, 3 hour integration, flux in emission line at 1500Å(FUVOP) and 2500Å(NUVOP). 2. Same as 1. over 0.1″ × 0.1″ area.
SP = Spectrograph; SP-CD = Cross Dispersion Spectrograph; SP-SS = Slitless Spectrograph

3.0 DETAILED INSTRUMENT DESCRIPTION

3.1 TRANSFER OPTICS

A component block diagram of the FOC transfer optics is shown in Figure 3. A conceptual schematic optical layout in a plane containing the V1 axis and the chief ray is shown in Figure 4. Radiation from the OTA enters the FOC through a baffled tube that leads to a field defining entrance aperture located in a plane tangential to the OTA focal surface and centered on or near the best focus point at the position of each relay. Just beyond the entrance aperture, the radiation encounters a light tight shutter mechanism that, in its closed position, introduces a calibration mirror into the beam to intercept light emitted by an internal source of visible radiation and to uniformly illuminate the FOC object plane.

Once past the shutter, radiation impinges on a two element aplanatic optical system consisting of a spherical concave primary and an elliptical convex secondary mirror. This optical system magnifies the OTA focal plane by a factor of two for the F/48 camera and four for the F/96 camera with negligible spherical aberration or coma. The mirrors are all made of Zerodur and overcoated with Al + MgF_2 for a reflection efficiency exceeding 0.7 above 1200Å.

An apodizer mask mounted on a small Cassegrain telescope can be moved on command into the optical beam just past the secondary mirror along the optical path and, with the beam in focus, right on the F/96 relay exit pupil. This device (the high resolution apodizer or HRA) reduces the scattered light induced by diffraction at the OTA secondary mirror spider and primary mirror mounting pads. It also provides an additional magnification of the F/96 image by a factor of three giving an effective focal ratio for this configuration of F/288. To partly compensate for the OTA off-axis astigmatism, a cylindrical MgF_2 lens is mounted in front of the Cassegrain. The HRA will also be used in conjunction with an appropriately placed 0.4 arcsecond wide occulting finger located in the field aperture mask (see Figure 6).

Near the exit pupil and just following the HRA in the F/96 camera are located four independently commandable rotating filter wheels. Two such wheels are located at or near the exit pupil in the F/48 camera. The F/96 filter wheels each have 12 equidistant working positions while the F/48 wheels each have 8 equidistant positions. Each wheel has one clear position. These devices carry a full complement of wide, medium and narrow bandpass and neutral density filters, polarizing and objective prisms.

In order to fold the light beam back onto the detector and to focus the FOC, a cylindrical concave mirror is placed into the slowly converging beam past the filter wheels. This mirror also corrects for the residual off-axis OTA astigmatism and is made of the same materials as the primary and secondary mirrors. This mirror is mounted on a commandable focussing mechanism that allows it to internally compensate for variations in optical path length introduced by the OTA focus variations, FOC internal stability and by the differing optical thicknesses of the various optical elements on the filter wheels. The focussing mechanism changes the length of the optical path by ± 16 millimeters maintaining the position of the image on the detector within 0.05 millimeters whatever the location of the mirror along the stroke. The FOC focal plane is designed to coincide with the detector photocathode plane. The detector samples an area of 24.6 × 24.6 millimeter squared corresponding to 1024 × 1024 pixels, each $\simeq$ 24 micron squared in size, averaged over the field of view.

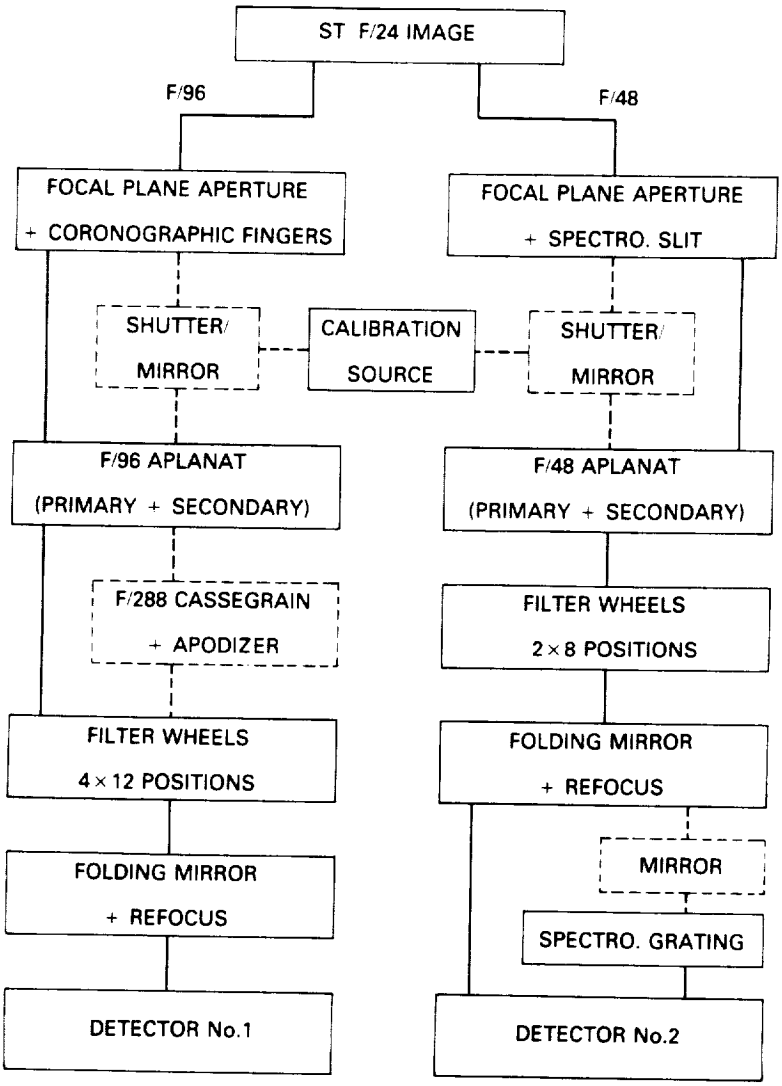

Figure 3. The Transfer Optics Block Diagram. The removable components are shown in the dashed frames.

Absolute image position on the FOC focal plane can be referred to a grid of 17 × 17 reseau marks, each 75 × 75 microns squared in size evaporated on the inner surface of the photocathode MgF_2 window. The overall wavefront distortion of the FOC optical system is less than $\lambda/10$ for the F/48 camera and less than $\lambda/15$ for the F/96 camera at λ6328Å. In all cases, the computed FOC point spread function by itself for sources anywhere in the field of view is much smaller than the detector pixel size of 24 × 24 microns squared.

In the F/48 camera, the beam from the folding mirror may be relayed by a removable toroidal convex mirror to a fixed spherical concave reflection grating which re-images a spectrum of a portion of the field of view onto the detector photocathode. This portion contains a fixed width rectangular slit that is located on the entrance aperture (see Figure

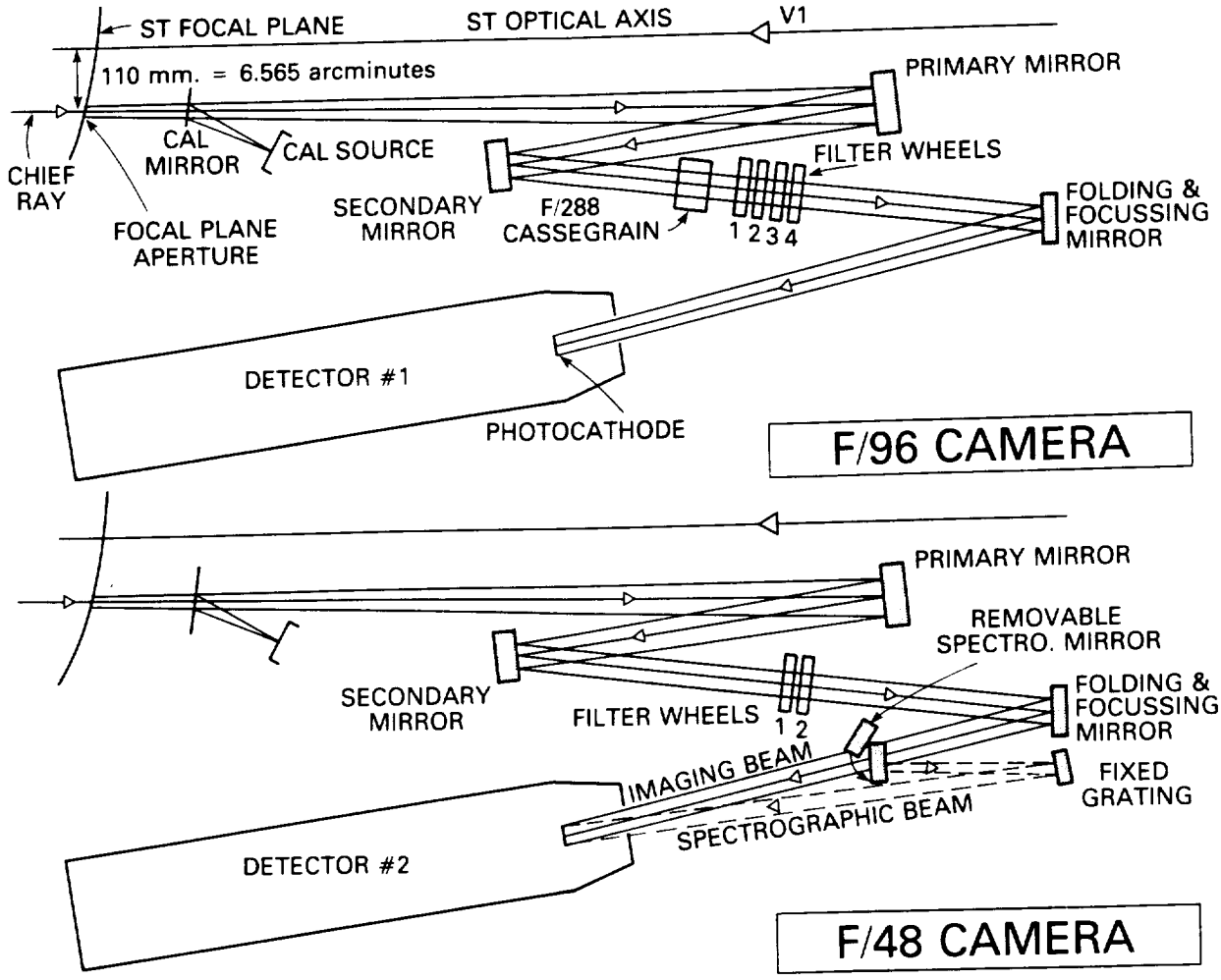

Figure 4. The schematic optical layout of the two cameras in the planes containing the V1 axis and the chief rays.

7). The grating works with a divergent beam in the Rowland condition at fixed wavelength ranges in the first (3600–5400Å), second (1800–2700Å), third (1200–1800Å) and fourth (900–1350Å) order at a resolution $\lambda/\Delta\lambda \simeq 1000$. Only the 1150–1350Å portion of the fourth order spectrum can be measured in practice, of course, due to the MgF_2 cut-off of the detector. Wavelength range selection is accomplished by introducing suitable bandpass filters into the F/48 optical path or by using the objective prism (FOPCD) whose dispersion axis is oriented at $\simeq 90°$ to the grating dispersion direction as a cross disperser.

3.2 FOCAL PLANE APERTURES

The two FOC field defining entrance apertures are each located in a plane tangent to an OTA focal surface at the center point of the aperture. The projection of these apertures onto the plane of the sky is shown in Figure 5. In this figure, the V1 axis runs into the paper at the center of the WF/PC field of view and V1, V2, V3, U2, and U3 are the HST axes

defined in the Call for Proposals and Proposal Instructions. The center of each aperture is located at a linear distance of 110 millimeters or an angular distance of 6.565 arcminutes from the V1 axis at the OTA best focus point for the F/48 camera and at the tangential focus for the F/96 camera. At these locations, the focal plane makes an angle of 10.05° with the normal to the ST axis. The axes of symmetry of the two FOC cameras D96 and D48 that run through the center of the apertures, perpendicular to and intersecting on the V1 axis form an angle of 30°. The D96 axis forms an angle of 30° with the + V2 axis and D48 an angle of 30° with the + V3 axis.

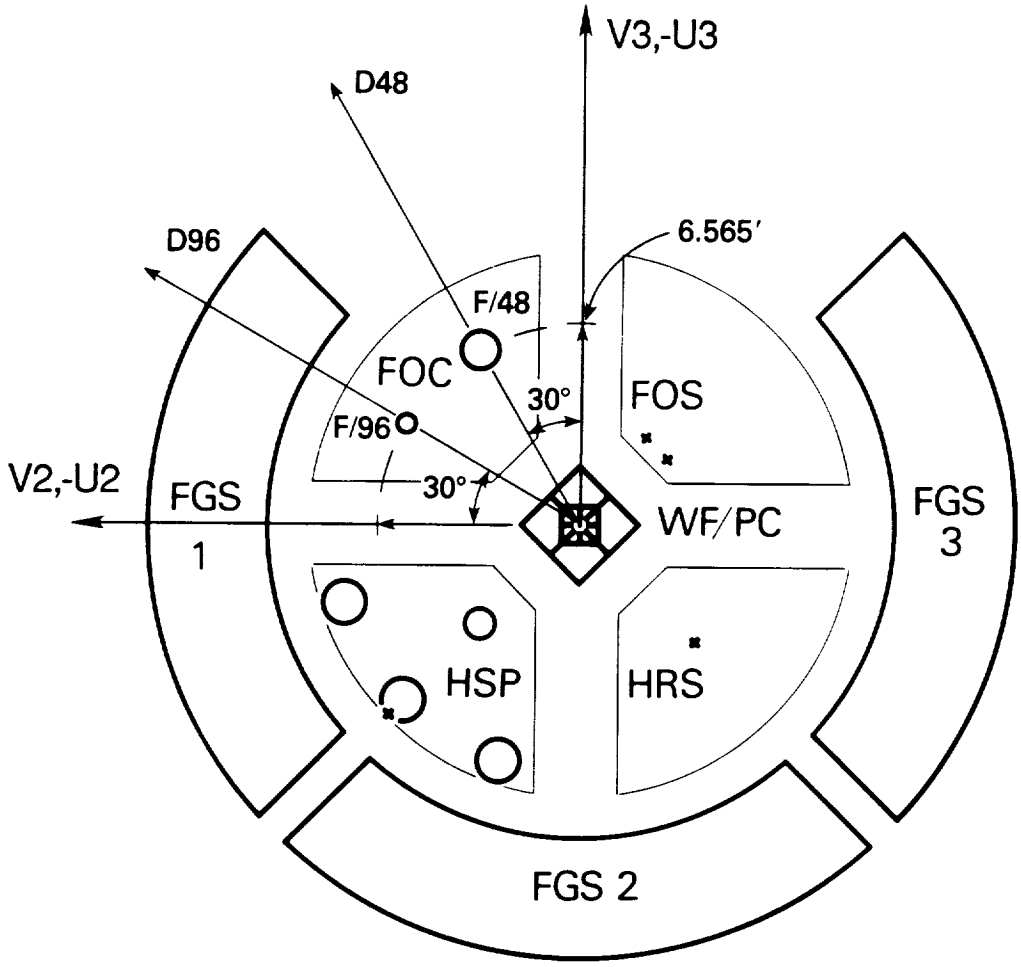

Figure 5. The location of the FOC entrance apertures on the HST focal plane projected onto the plane of the sky. In this perspective V1 is directed into the paper at the center of the WF/PC pattern. V1, V2 and V3 form the HST right handed coordinate system defined in the Call for Proposals.

An expanded view of the two apertures in exactly the same perspective is shown in Figures 6 and 7. The F/96 camera aperture is a circular diaphragm of 10.5 millimeters in diameter corresponding to 37.6 arcseconds on the sky centered at point O with two 2 millimeter-long protruding opaque metal fingers oriented 30° to the D96 line and parallel to the V2 axis. The finger on the right is 0.112 millimeters thick (0.4 arcseconds in the sky) while the other is 0.223 millimeters thick (0.8 arcseconds in the sky). The directions of increasing sample (S) and line (L) numbers for the extended SDS format define the image coordinate system with its center at point C_{96}. This system is aligned with the X, Y reference system used to designate the orientation of the apertures on the sky in the Proposal Instructions. The sample direction makes an angle of 4° with D96; the corners ABCD of the 512 × 1024 zoomed format are marked on Figure 6. The large 22 × 22 arcsecond square marks the limit of the extended format. The opaque coronographic fingers are indicated by the hatched regions. The V1 axis is 6.565 arcminutes from O in the direction indicated to V1. The HRA extended 7.3 × 7.3 arcseconds squared format location with its center C_{288} is also shown in this figure in the upper right hand corner.

The F/48 entrance aperture is shown in Figure 7. The center O of the main aperture coincides with the center of the SDS format and lies on the tangential focus while the center J of the slit lies on the sagittal focus of the OTA. The main aperture is essentially a circular diaphragm with a diameter of 21 millimeters corresponding to 75.2 arcseconds in the sky except for an oblique truncation at points E and H. A thin, 0.23 arcsec wide opaque finger points to O from point G and is used mainly for target acquisition (see section 4.2). A 5.689 millimeters (20 arcsecond) long, 0.028 millimeters (0.1 arcsecond) wide slit centered at J is located between points I and K. This slit forms the defining aperture of the F/48 spectrograph. The corners of the 512 × 1024 zoomed 44 × 44 arcsecond squared extended imaging format are given on Figure 7 as points A, B, C and D. When the spectrograph mirror is in place, the aperture is imaged onto the extended SDS format as shown in Figure 7 with the dashed lines representing the inner and outer edge of the spectrally dispersed image of the slit and the edge of the main aperture drawn for the specific case of the Hg line at 4358Å. The opaque target acquisition finger is indicated by the dark region. V1 is 6.565 arcminutes from O in the direction indicated to V1. A part of the dispersed main aperture falls in the right hand quarter of the extended format and may be eliminated by tailoring the observing format to the region inside the slit area. Wavelength increases in the direction indicated by λ from 3600Å to 5400Å in first order. Slitless spectroscopy can be performed in the clear region to the right of the dashed lines (see Section 3.6).

In order to predict reasonably accurately the location and orientation of an extended source in the FOC fields of view and to determine whether or when the required instrument orientations are compatible with the HST roll angle restrictions, it may be useful to locate with respect to the S, L axes on figures 6 and 7 the celestial reference axes for that particular target and viewing configuration. To accomplish this, simply follow the procedures described in the Call for Proposals with the transparent POSS overlay provided therein. Then, position a transparent copy of figures 6 and 7 on top of the overlay in such a way that point O coincides with the appropriate center of the small FOC circular fields reproduced on the overlay and that the D96 axis passes through the center of the WFPC pattern. In that particular position, the N and E directions of the POSS print can be directly translated onto the FOC field of view.

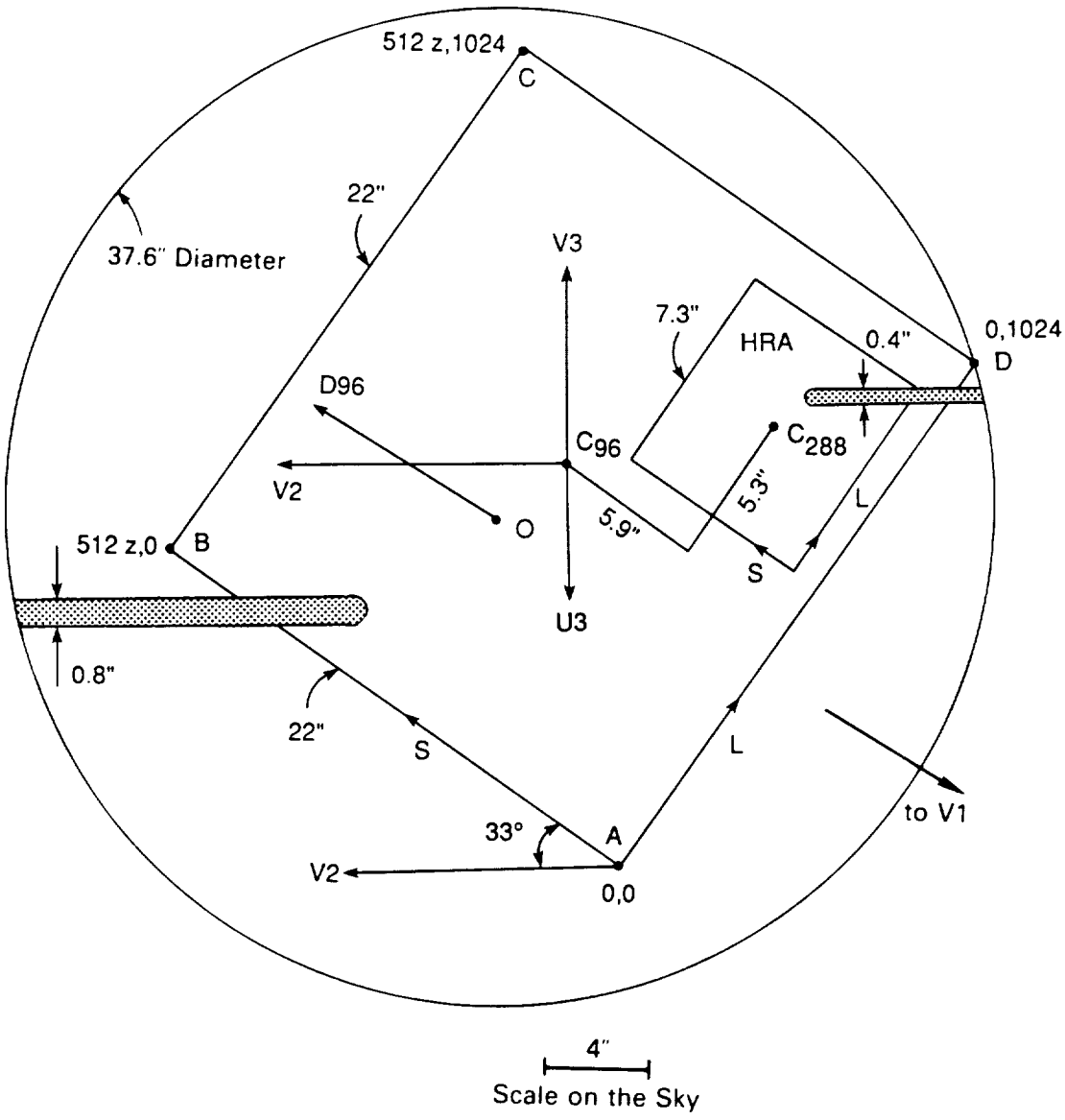

Figure 6. The F/96 camera entrance aperture projected onto the sky.

To specify a particular orientation of the apertures with the ORIENT special requirement of the exposure logsheets (see Proposal Instructions), place the object to be observed in the proper configuration on the entrance aperture shown in Figures 6 and 7. This will determine the desired positions of the N and E directions on the same apertures. The angle between these directions and the $-$V3 or U3 axis drawn on these figures (measured E from N) is the angle to specify in this special requirement. To illustrate this technique, an outline of the extended F/48 format as given in Figure 7 is superimposed on a photograph of NGC 4486 (M87) with the same scale in Figure A1 of the Appendix. The orientation of the format

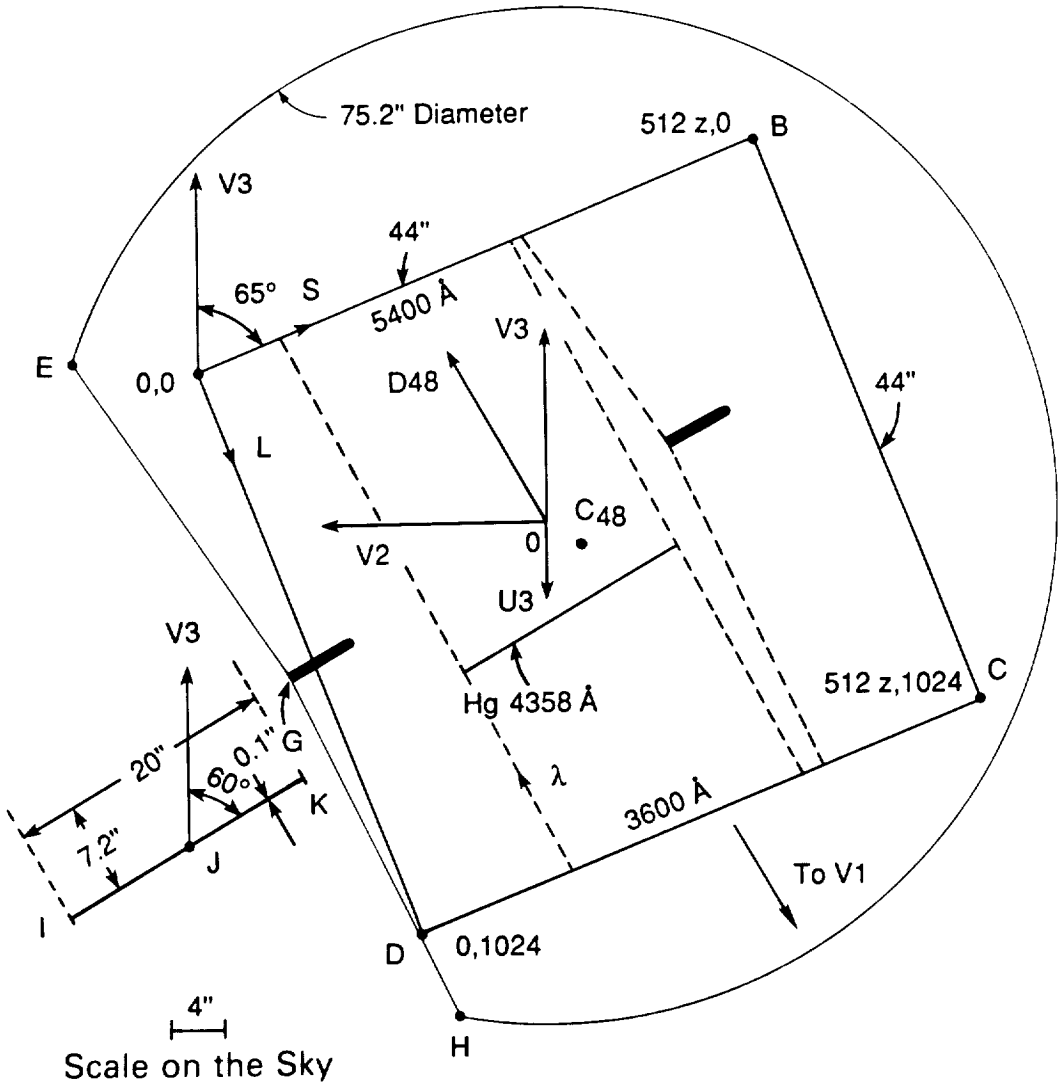

Figure 7. The F/48 camera entrance aperture projected onto the sky. KI along the spectrograph slit coincides with the reference axis x that is used to designate the orientation of the apertures on the sky in the Proposal Instructions.

is chosen such that the jet located at p.a. 291° is placed antiparallel to L as indicated for optimum imaging performance. Since the axis L makes an angle of 21° with East and 25° with U3, the position angle of U3 with respect to North is exactly 90° + 21° + 25° = 136°. Thus, one would enter ORIENT 136D±10D in the Special Requirements column in the exposure logsheet to ensure the proper orientation of ST during the exposure. Only slightly more tricky would be the orientation for a long slit spectrum of the M87 jet. Rotating the outline shown in Figure A1 so that the jet lies within the slit as much as possible, one finds that the p.a. of U3 in this case is 291° − 60° = 231° where 291° is the p.a. of the jet and 60° is the angle between the slit and U3. Of course, the opposite direction of 51° is just as good,

in principle, but is better in practice because that way the bright nucleus of the galaxy falls well out of the F/48 extended aperture thereby reducing or eliminating a serious source of possible scattered light contamination (see Section 3.6).

The aperture configurations described in this section correspond to the nominal position determined during extensive ground calibrations of the FOC. As a result of subsequent instrument configuration changes, launch stress, in-flight environmental conditions (especially zero gravity) and OTA and detector refocussing effects, however, the precise in-flight aperture geometry may turn out to be somewhat different from that shown here. As a rule of thumb, one can expect shifts of the position of any projected physical feature on the photocathode plane of up to ± 1 millimeter. This corresponds to angular uncertainties of ±2, ±1, and ±0.3 arcseconds in the F/48, F/96, and F/288 relays, respectively. Thus, any FOC observing program requiring finer tolerances than these cannot be performed before the precise aperture, finger and slit locations have been determined in-flight during orbital and science verification.

Actual images of the extended 512 zoom × 1024 pixels squared F/48, F/96, F/288, and F/48 spectrograph fields obtained on the ground with external flat field illumination of the FOC entrance apertures are shown in Figures A2–A5 in the Appendix. The images are displayed in a 512 × 512 format so every other line L is not displayed in these figures in the vertical axis. The occulting fingers, spectrograph slit, reseaux marks appear clearly together with some blemishes and large scale response inhomogeneities. The latter are discussed in more detail in section 5.9.

3.3 INTERNAL CALIBRATION SYSTEM

When the shutter is closed, an Al + MgF_2 mirror (see Figure 4) reflects the light beam from a light emitting diode (LED) calibration source into the optical path of the relay. The position of the source and the curvature of the mirror insure a quasi flat field illumination of the object plane. The unit consists of seven LEDs (two red, two yellow, two green and one blue) illuminating an integrating sphere. Their normalized emission spectra are shown in Figure 8. The unit is capable of illuminating both calibration mirrors simultaneously. Each LED output can be set to 256 separately commandable intensity levels. The calibration system will be used to determine the detector's intensity transfer function, the uniformity of response, the FOC response to visible light and the geometric distortion. A comparison between external and LED flat field illumination of the detectors at the same wavelengths shows that the spatial variations of LED illumination are less than ±3% peak to peak over most of the field of view. The only exception is due to one edge of the circular mirror on the back of the F/48 shutter preventing LED light from illuminating the lower right hand corner of the F/48 frame.

3.4 HIGH RESOLUTION APODIZER

The high resolution apodizer (HRA) Cassegrain telescope consists of aspherical primary and secondary mirrors overcoated with Al+MgF_2 and separated by a light weight spacer. The secondary mirror is supported by a spider. All these elements are made of Zerodur and are assembled by optical contacting. The physical layout of the HRA is shown in Figure 9 with the V2, V3 axes parallel to the spacecraft V2, V3 axes. The MgF_2 cylindrical lens,

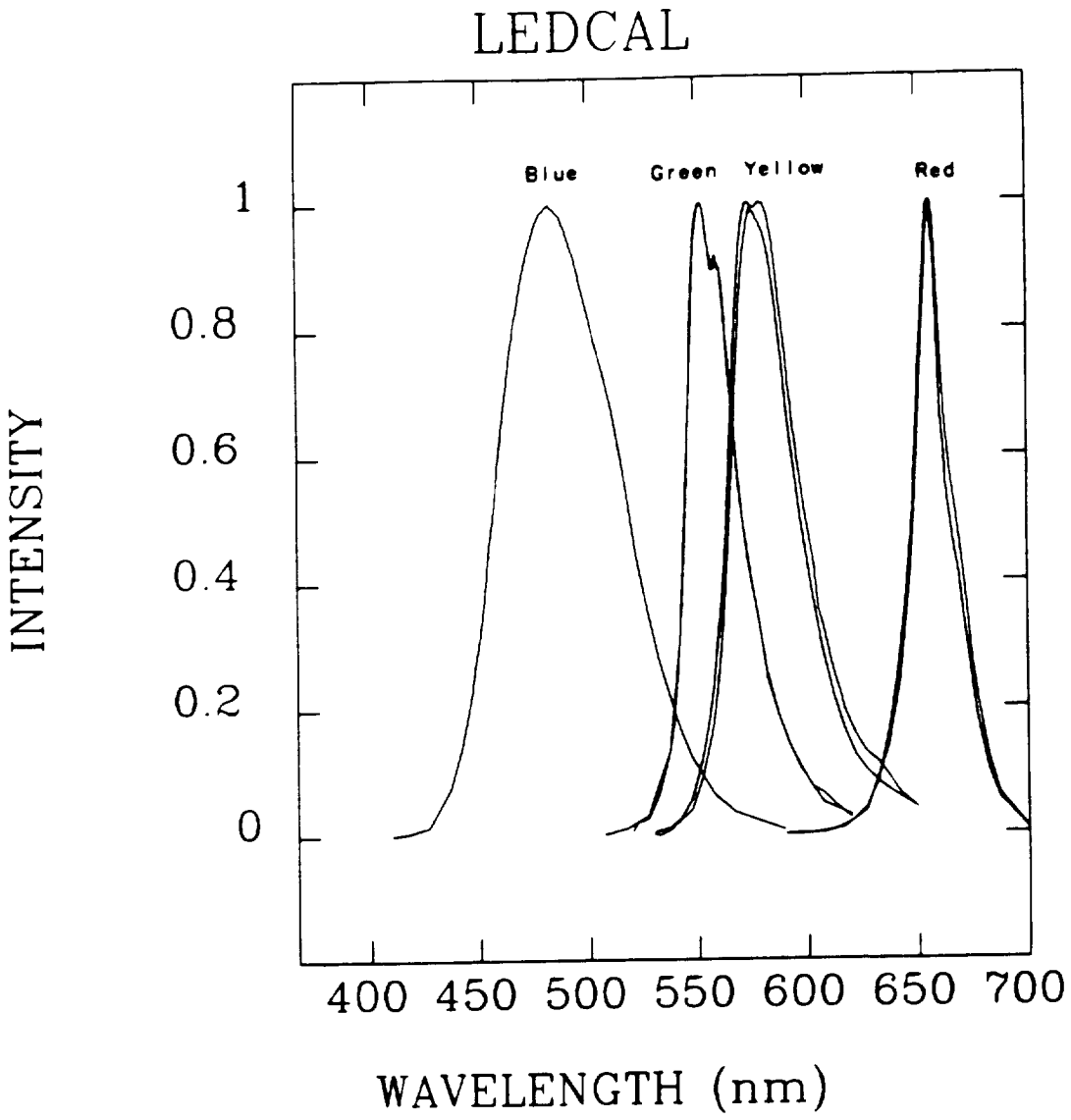

Figure 8. Normalized Emission Spectra of the Calibration LEDs

the apodizer mask and the Invar mount are glued to the spacer. The focal length of the Cassegrain is −701 mm.

The design of the apodizer mask is determined by the OTA entrance pupil geometry. The obscuration ratio defined as the ratio of the useful area of the FOC exit pupil with and without the mask is 29%. The HRA field of view location on the plane of the sky is shown in Figure 6. The HRA extended field of view is 7.3 × 7.3 arcsecond squared in size and is offset with respect to the F/96 field of view in order to image the 0.4 arcsecond coronographic finger in one quadrant of the detector faceplate. The 0.8 arcsec coronographic finger can only be used without the apodizing and magnifying functions of the small Cassegrain. The F/96 optical relay is designed to correct the OTA astigmatism at the center of the detector by means of the cylindrical folding mirror. When the HRA is inserted in the beam, however, the

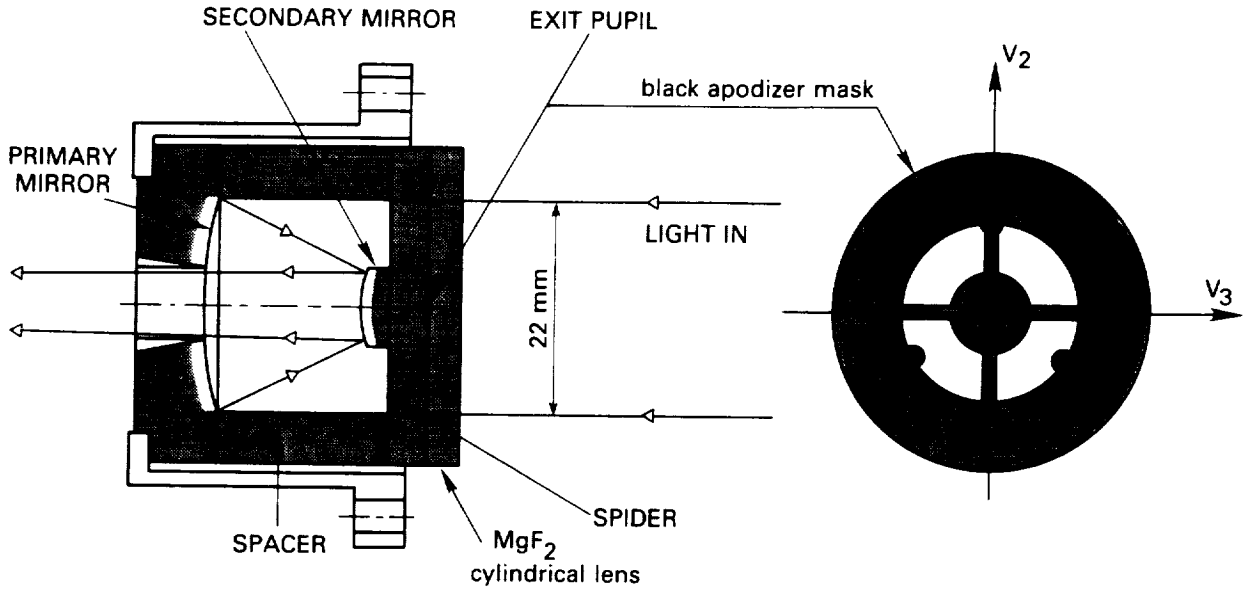

Figure 9. Physical Layout of the HRA

beam diameter falling on the folding mirror becomes approximately one third of its normal size, as shown in Figure 9. The MgF_2 lens in the HRA is designed to solve this problem by exactly cancelling the residual astigmatism at 1700Å. The result is a small chromatic astigmatism at other wavelengths reaching up to about 21mm and −13mm rms at 1300 and 6000Å, respectively but should not result in a significant loss of resolution. The apodizer mask should reduce light in the wings of the PSF especially the prominent diffraction spikes due to the spider supporting the OTA secondary mirror provided that, of course, diffraction is the dominant effect. For a more detailed discussion of this point see Section 5.1.

3.5 FILTER WHEELS

The FOC has six commandable rotating filter wheels holding 58 optical elements and six clear apertures. Four wheels are on the F/96 relay and two on the F/48 relay. The F/96 camera wheels have 3 long pass, 9 wide band, 20 medium band, 2 narrow band and 5 neutral density filters. They also contain 3 polarizers and 2 objective prisms. The F/48 camera wheels contain 3 long pass, 8 wide band, and 3 objective prisms. A complete list of the optical elements ordered by increasing peak wavelengths λ_o is given in Tables 3 and 4. In these tables, FW indicates the filter wheel number (1-4 for F/96, 1-2 for F/48), camera indicates the appropriate relay (F/96, F/288, or F/48), ID the filter identification code, λ_o the wavelength at the peak of the curve representing the convolution of the filter transmission (T) with the OTA + FOC response function, (Q) described in Section 5.3, $\Delta\lambda$ the full width at half maximum of this curve, and $T(\lambda_0)$ is the filter transmission at λ_0, and $QT(\lambda_0)$ is $T(\lambda_0)$ multiplied by Q. Δm gives the magnitudes of attenuation of the neutral density filters at 3000Å. These filters are placed on the wheels in such a way as to allow beam attenuation in increments of 1 magnitude from 1 to 9 magnitudes.

Table 3. F/96 and F/288 Optical Element Characteristics Ordered by Peak Wavelength

FW	Camera	ID	λ_o(Å)	$\Delta\lambda$(Å)	T(λ_o)	QT(λ_o)	Comments
3	F/96	F120M	1230	86	0.10	0.003	Medium band
	F/288	F120M	1230	82	0.09	0.001	Medium band
3	F/96	F130M	1280	88	0.10	0.003	Medium band
	F/288	F130M	1280	88	0.10	0.001	Medium band
2	F/96	F140W	1360	278	0.21	0.009	Wide band
	F/288	F140W	1360	298	0.21	0.003	Wide band
3	F/96	F140M	1390	170	0.08	0.003	Medium band
	F/288	F140M	1390	170	0.07	0.001	Medium band
3	F/96	F152M	1500	188	0.08	0.003	Medium band
	F/288	F152M	1510	196	0.07	0.001	Medium band
3	F/96	F165W	1640	878	0.28	0.010	Wide band
	F/288	F165W	2116	944	0.27	0.005	Wide band
3	F/96	F170M	1760	186	0.18	0.006	Medium band
	F/288	F170M	1760	182	0.18	0.003	Medium band
2	F/96	F175W	1730	714	0.24	0.009	Wide band
	F/288	F175W	1740	789	0.23	0.004	Wide band
3	F/96	F195W	2100	898	0.42	0.021	Wide band
	F/288	F195W	2198	700	0.4	0.013	Wide band
3	F/96	F190M	1990	274	0.15	0.007	Medium band
	F/288	F190M	2042	312	0.15	0.003	Medium band
3	F/96	F210M	2150	212	0.18	0.011	Medium band
	F/288	F210M	2160	202	0.18	0.007	Medium band
2	F/96	F220W	2260	470	0.39	0.028	Wide band
	F/288	F220W	2250	442	0.38	0.018	Wide band
3	F/96	F231M	2330	228	0.18	0.014	Medium band
	F/288	F231M	2330	230	0.18	0.009	Medium band
4	F/96	F253M	2540	236	0.18	0.017	Medium band
	F/288	F253M	2550	232	0.18	0.011	Medium band
2	F/96	F275W	2740	594	0.4	0.039	Wide band
	F/288	F275W	2740	578	0.4	0.027	Wide band
4	F/96	F278M	2790	314	0.26	0.026	Medium band
	F/288	F278M	2790	310	0.26	0.018	Medium band

Table 3. F/96 and F/288 Optical Element Characteristics Ordered by Peak Wavelength (continued)

FW	Camera	ID	λ_o(Å)	$\Delta\lambda$(Å)	T(λ_o)	QT(λ_o)	Comments
4	F/96	F307M	3070	326	0.26	0.029	Medium band
	F/288	F307M	3070	328	0.26	0.019	Medium band
4	F/96	F130LP	3402	2604	0.92	0.11	Long pass ($\lambda \geq$ 1300Å)
	F/288	F130LP	4000	2666	0.92	0.073	Long pass ($\lambda \geq$ 1300Å)
2	F/96	F320W	3360	926	0.89	0.10	Wide band, ghost, image shift
	F/288	F320W	3360	938	0.89	0.067	Wide band, ghost, image shift
2	F/96	F342W	3400	706	0.81	0.093	Wide band, U filter
	F/288	F342W	3420	712	0.81	0.061	Wide band, U filter
4	F/96	F346M	3450	432	0.58	0.066	Medium band, u filter
	F/288	F346M	3480	434	0.58	0.044	Medium band, u filter
4	F/96	F372M	3700	412	0.73	0.081	Medium band
	F/288	F372M	3710	412	0.73	0.056	Medium band
2	F/96	F430W	3960	870	0.74	0.081	Wide band, B filter
	F/288	F430W	4000	890	0.73	0.061	Wide band, B filter
2	F/96	F370LP	4020	1072	0.83	0.088	Long pass ($\lambda \geq$ 3700Å)
	F/288	F370LP	4040	1158	0.84	0.065	Long pass ($\lambda \geq$ 3700Å)
4	F/96	F410M	4100	194	0.58	0.059	Medium band, v filter
	F/288	F410M	4100	194	0.58	0.043	Medium band, v filter
4	F/96	F437M	4290	446	0.71	0.063	Medium band, ghost
	F/288	F437M	4290	446	0.71	0.047	Medium band, ghost
4	F/96	F470M	4710	210	0.79	0.045	Medium band, b filter
	F/288	F470M	4710	208	0.79	0.036	Medium band, b filter
2	F/96	F486N	4870	34	0.63	0.028	Interference filter centered on Hβ line
	F/288	F486N	4870	34	0.63	0.023	Interference filter centered on Hβ line
4	F/96	F502M	4850	406	0.82	0.033	Medium band
	F/288	F502M	4920	422	0.82	0.027	Medium band
2	F/96	F501N	5010	74	0.68	0.022	Interference filter centered on [O III] line, ghost
	F/288	F501N	5010	74	0.68	0.02	Interference filter centered on [O III] line, ghost
2	F/96	F480LP	4940	680	0.82	0.027	Long pass ($\lambda \geq$ 4800Å), V filter
	F/288	F480LP	4970	644	0.82	0.024	Long pass ($\lambda \geq$ 4800Å), V filter
4	F/96	F550M	5460	188	0.77	0.012	Medium band, y filter
	5F/288	F550M	5460	188	0.77	0.01	Medium band, y filter

Table 3. F/96 and F/288 Optical Element Characteristics Ordered by Peak Wavelength (continued)

FW	Camera	ID	λ_o(Å)	$\Delta\lambda$(Å)	T(λ_o)	QT(λ_o)	Comments
1	F/96	F600M	5800	412	0.8	0.007	Medium band
	F/288	F600M	5800	612	0.8	0.006	Medium band
1	F/96	F630M	6384	208	0.67	0.001	Medium band
	F/288	F630M	6502	266	0.58	0.004	Medium band
1	F/96	CLEAR	3400	2606	1.0	0.12	Clear aperture
	F/288	CLEAR	3802	2676	1.0	0.08	Clear aperture
1	F/96	F8ND	3204	2442	9×10^{-4}	10^{-4}	Neutral density,Δm =8.0
	F/288	F8ND	4000	2572	9×10^{-4}	7×10^{-5}	Neutral density,Δm =8.0
1	F/96	POL120	3402	2580	0.91	0.11	Polarizer, 120°
	F/288	POL120	3960	2656	0.92	0.072	Polarizer,20°
1	F/96	F2ND	3250	2486	0.19	0.023	Neutral density,Δm =2.0
	F/288	F2ND	3402	2574	0.2	0.015	Neutral density, Δm =2.0
1	F/96	POL0	3400	2580	0.92	0.110	Polarizer, 0°
	F/288	POL0	3950	2656	0.92	0.073	Polarizer, 0°
1	F/96	F4ND	3400	2498	0.03	0.004	Neutral density, $\Delta = m$ =4.0
	F/288	F4ND	4000	2628	0.029	0.002	Neutral density, Δm =4.0
1	F/96	F6ND	2402	3236	0.005	4.7×10^{-4}	Neutral density, Δm =6.0
	F/288	F6ND	2602	2520	0.005	3×10^{-4}	Neutral density, Δm =6.0
1	F/96	PRISM2	3400	2544	0.94	0.108	Near UV objective prism (NUVOP)
	F/288	PRISM2	3950	2636	0.94	0.074	Near UV objective prism (NUVOP)
1	F/96	POL60	3402	2456	0.92	0.11	Polarizer, 60°
	F/288	POL60	3840	2540	0.93	0.073	Polarizer, 60°
1	F/96	PRISM1	3400	2620	0.94	0.11	Far UV objective prism (FUVOP)
	F/288	PRISM1	4000	2682	0.94	0.073	Far UV objective prism (FUVOP)
3	F/96	F1ND	3400	2512	0.39	0.044	Neutral density, Δm =1.0
	F/288	F1ND	3402	2596	0.39	0.029	Neutral density, Δm =1.0

Table 4 F/48 Optical Element Characteristics Ordered by Peak Wavelength

FW	Camera	ID	λ_o(Å)	$\Delta\lambda$(Å)	T(λ_o)	QT(λ_o)	Comments
1	F/48	F140W	1320	302	0.20	0.008	Wide band
1	F/48	F150W	1400	606	0.23	0.011	Wide band
1	F/48	F175W	1720	664	0.18	0.006	Wide band
1	F/48	F195W	2108	1096	0.36	0.019	Wide band
1	F/48	F220W	2250	480	0.36	0.026	Wide band
2	F/48	F275W	2750	654	0.29	0.026	Wide band
2	F/48	F130LP	3400	2726	0.94	0.085	Long pass ($\lambda \geq$ 1300Å)
2	F/48	F180LP	3400	2706	0.92	0.083	Long pass ($\lambda \geq$ 1800Å)
2	F/48	F342W	3400	706	0.83	0.075	Wide band, U filter
1	F/48	F305LP	3440	1680	0.92	0.080	Long pass ($\lambda \geq$ 3050Å)
2	F/48	F430W	3940	936	0.75	0.058	Wide band, B filter
1	F/48	CLEAR	2802	2704	1.0	0.09	Clear aperture
1	F/48	PRISM3	3350	2726	0.96	0.087	Far UV Cross Disperser Objective Prism (FOPCD)
2	F/48	PRISM2	3350	2706	0.88	0.08	Near UV Objective Prism (NUVOP)
2	F/48	PRISM1	3080	2738	0.96	0.087	Far UV Objective Prism (FUVOP)

The F/96 camera filter wheel system allows, in principle, up to 12^4 or 20,736 and the F/48 system up to 8^2 or 64 different combinations of optical elements. Clearly, only a fraction of these will find a useful astronomical application. Observing configurations requiring more than one filter on the same wheel are not possible, of course. Filter positions on the wheels were carefully selected in order to minimize this possibility. The time required to change some filter combinations may reach 3 minutes. This implies a considerable expense in overhead time for programs requiring extensive cycling between filters.

3.5.1 Bandpass and Neutral Density Filters

In general, the wide band filters are Schott colored glass combined with a low pass filter, the broad band filters are metallic UV filters, the narrow band filters are multi-dielectric multi-element with ZnS-Th F_4 layers, and the interference filters are multi-dielectric multi-element with ZnS chiolithe layers. The measured transmission versus wavelength curves for all the F/96 and F/48 relay filters and attenuators are shown in Figures 10–14.

In order to suppress ghost images, the external faces of all mono-element filters are parallel to within 5 arcseconds or better. For multi-element filters the tolerance is 1 arcminute. The cemented elements have a wedge angle of 1° or less. In order to minimize losses in the

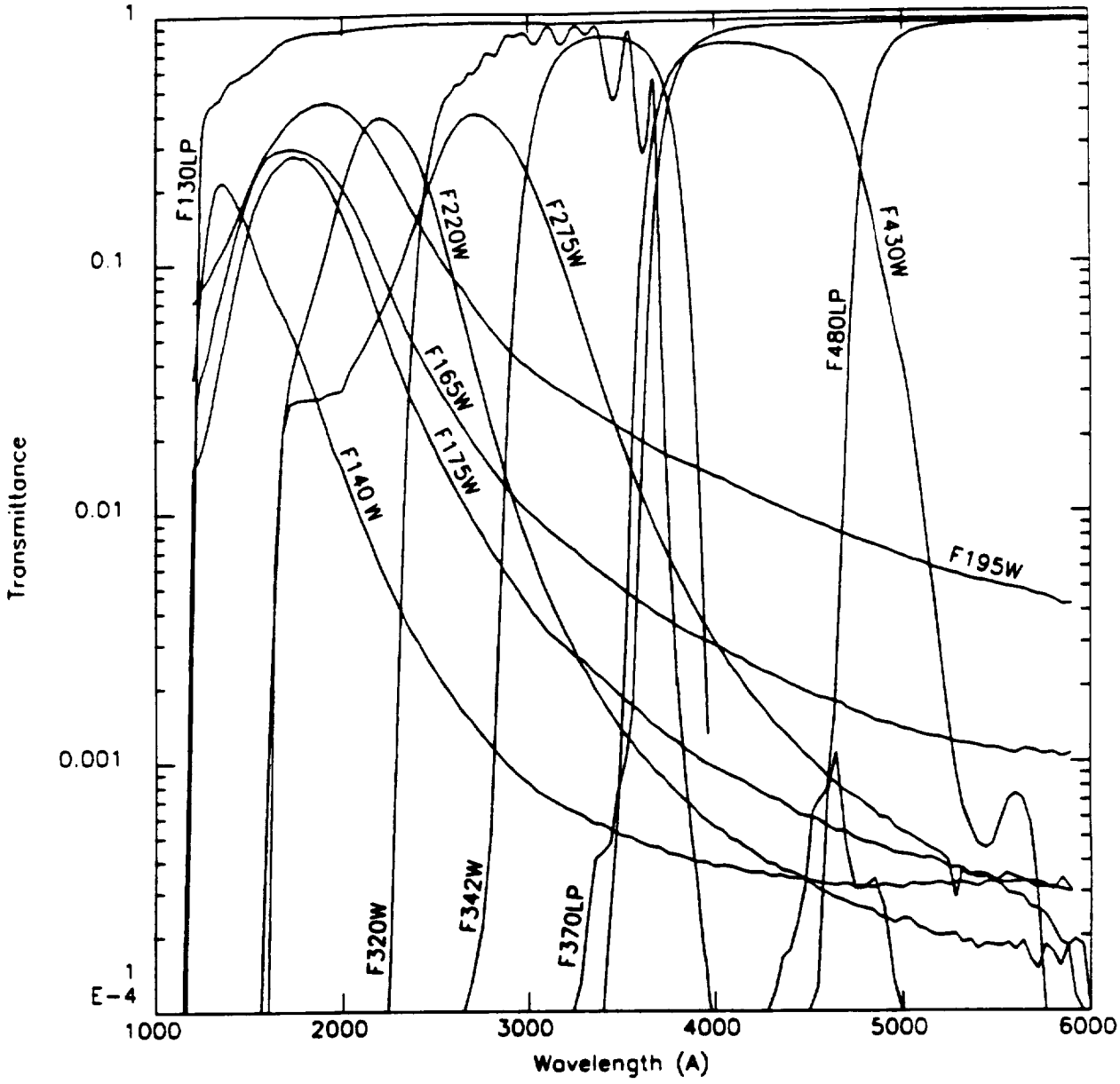

Figure 10. Transmittance of the long pass and wide band filters on the F/96 filter wheels as a function of wavelength.

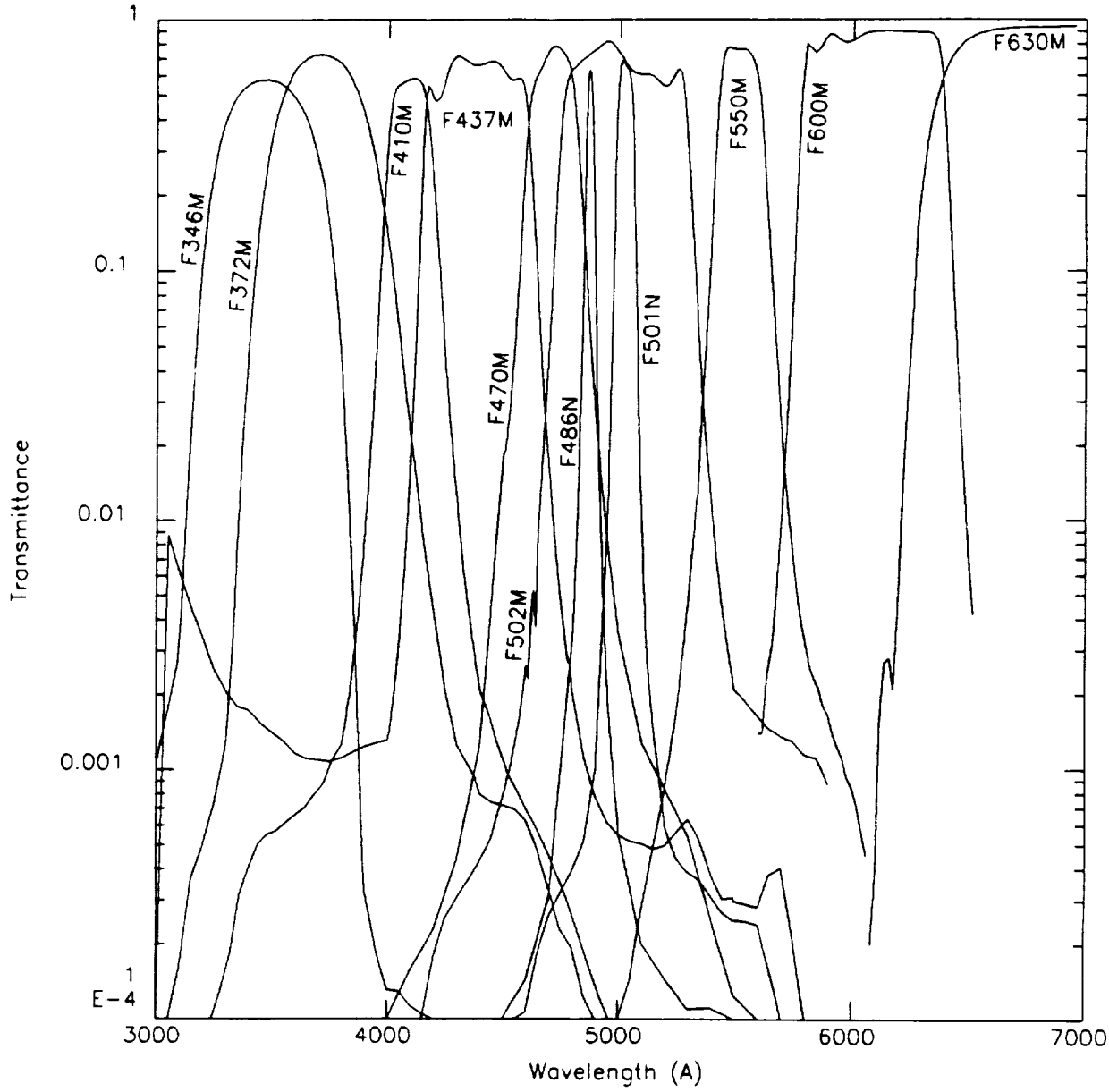

Figure 11. Transmittance of the visible medium and narrow band filters in the F/96 filter wheels as a function of wavelength.

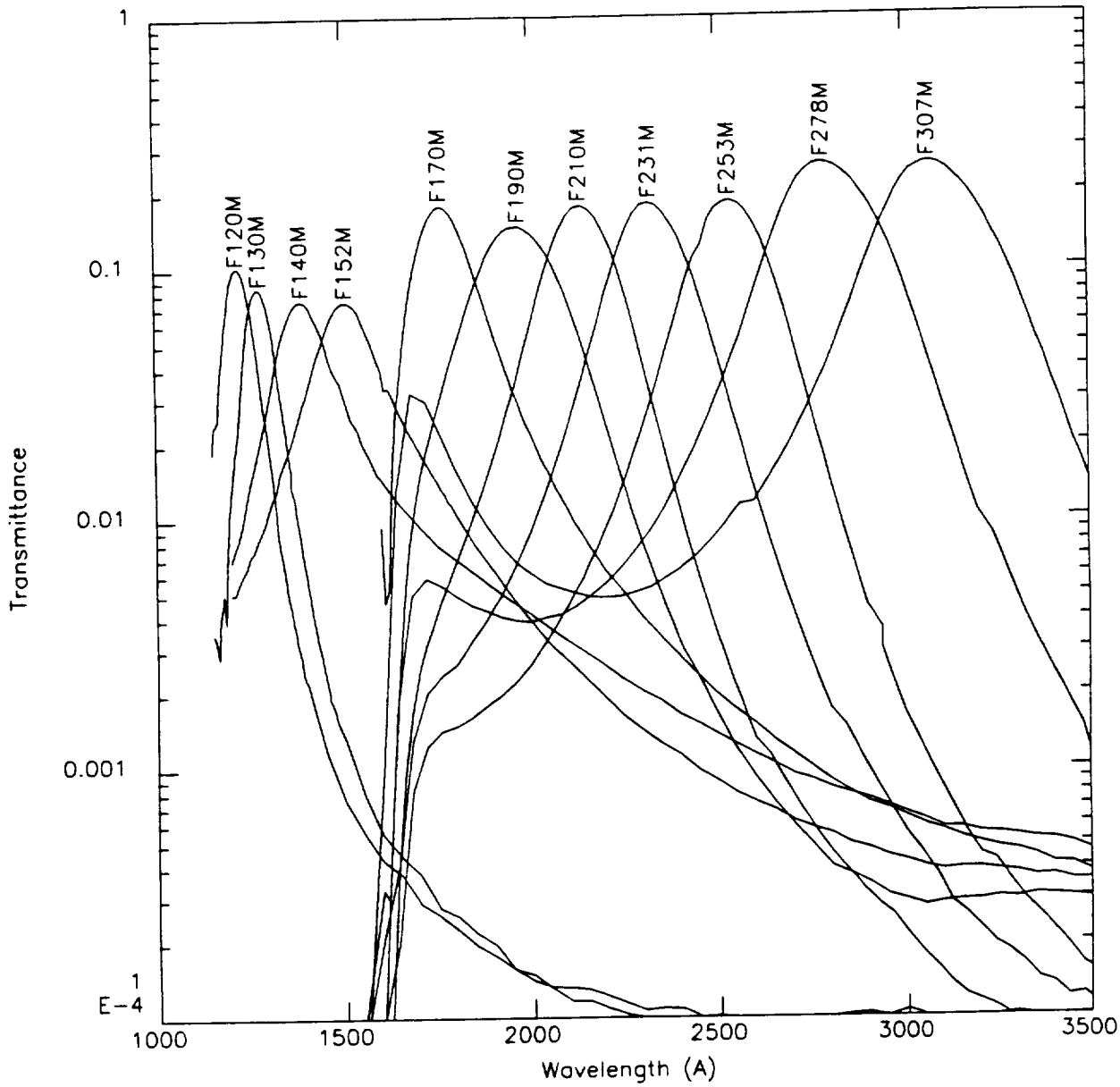

Figure 12. Transmittance of the UV medium band filters on the F/96 filter wheels as a function of wavelength. The F120M and F130M filter transmission curves remain essentially flat at 10^{-4} beyond $\simeq$ 2500Å.

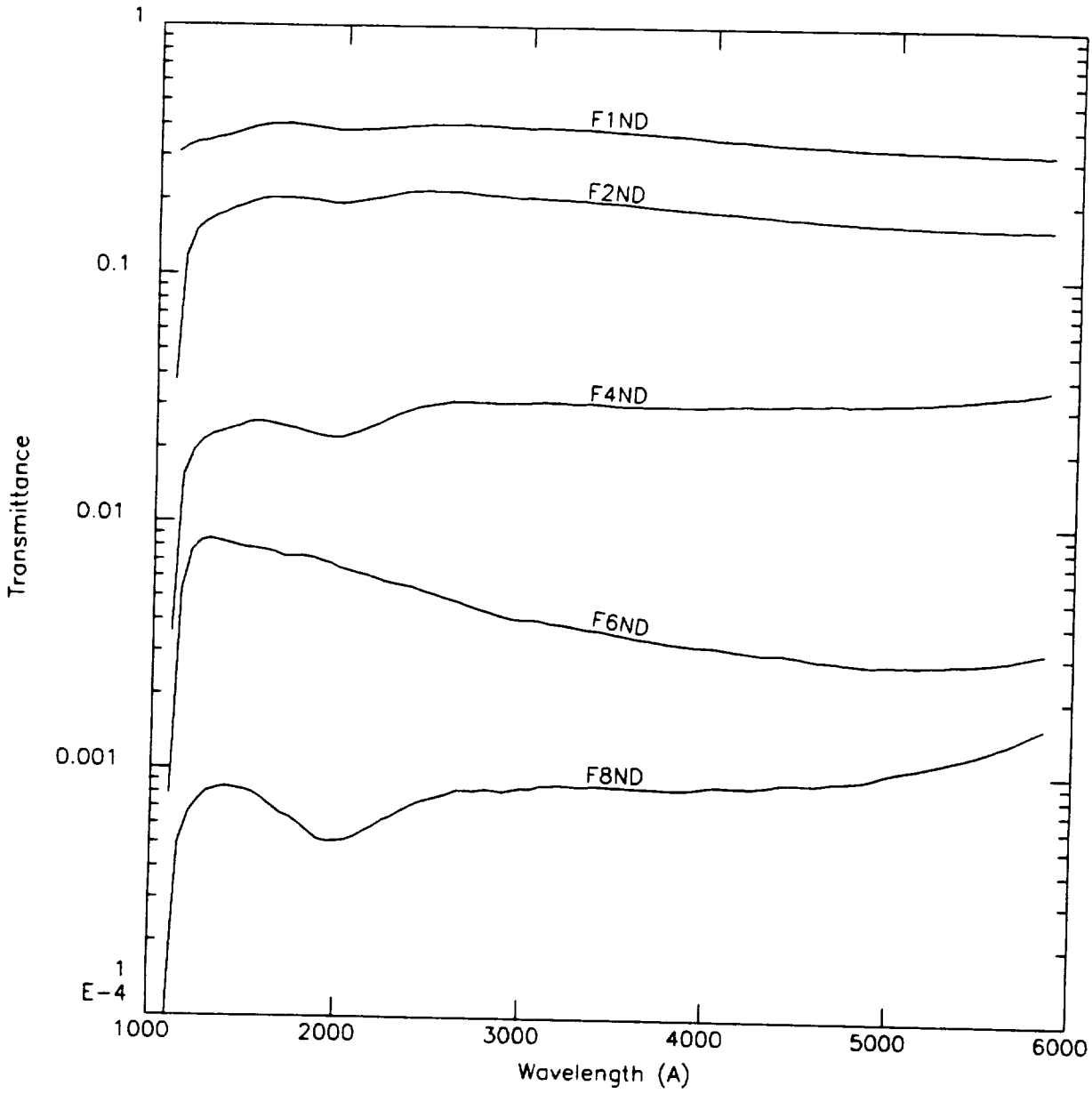

Figure 13. Transmittance of the neutral density filters on the F/96 filter wheels as a function of wavelength.

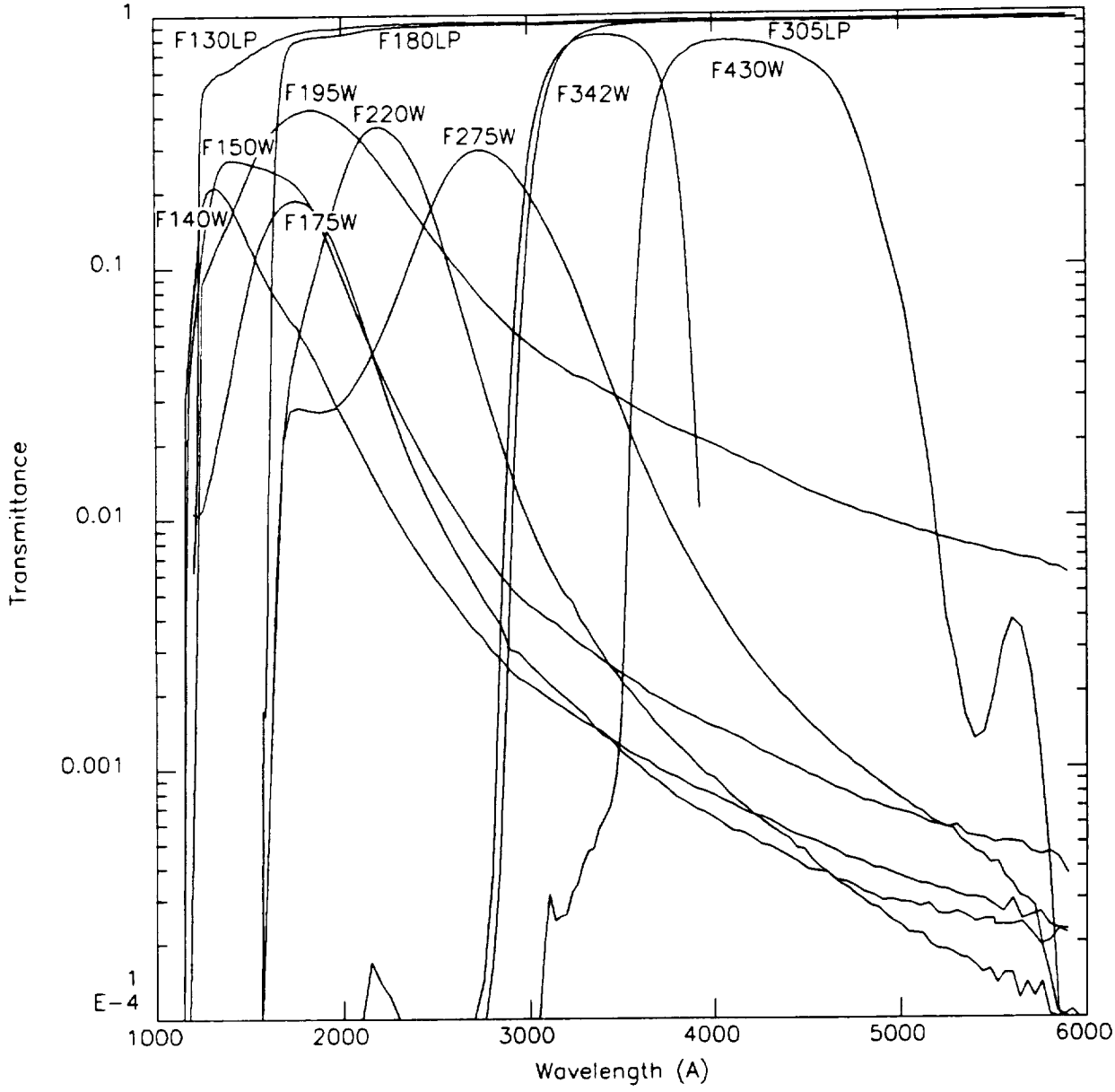

Figure 14. Transmittance of all the filters on the F/48 filter wheels as a function of wavelength.

modulation transfer function, the external faces are flat to $\lambda/5$ peak to peak at 6300Å and the internal faces in the multi-element filters are flat to $\lambda/2$ peak to peak. The refractive index is homogeneous to a level of $\Delta n < 2 \cdot 10^{-5}$ to be consistent with the $\lambda/5$ flatness constraint. These conditions have been complemented by the introduction of appropriate tilt angles of the different filter wheels themselves. Transmission non-uniformities are held to within ±5% over the whole surface. Ground tests of the FOC with a point source projector have been performed with all filters. A few have been found to exhibit faint ghost images and image shifts. These filters are flagged in the Comments column.

3.5.2 Objective Prisms

The objective prisms consist of either a single 30 millimeter diameter, 3 millimeter thick wedged crystal of MgF_2 (the FUVOP and FOPCD, called PRISM 1 and PRISM 3 in the Instructions) or a combination of two wedged crystals of MgF_2 and SiO_2 glued together (the NUVOP called PRISM 2 in the Instructions). The former operates down to 1150Å with a wavelength dispersion $\lambda/\Delta\lambda \simeq 50$ at 1500Å while the latter has a dispersion $\lambda/\Delta\lambda \simeq 100$ at 2500Å but transmits only above $\simeq$ 1600Å. All of the prisms disperse in a direction oriented roughly anti-parallel to the increasing line number (L) direction except FOPCD on FW # 1 of the F/48 camera that, instead, disperses in a direction roughly perpendicular to L or about 90° to the the others. This last one is meant as a cross disperser (CD) for the long slit spectrograph (see section 3.6). The MgF_2 prisms (FUVOP and FOPCD) on the F/48 relay (Prisms 1 and 3) are both preceded by a 3 mm. thick CaF_2 window in order to reduce geocoronal Lyman alpha contamination. These prisms, therefore, have negligible transmissions below $\simeq$ 1250 Å.

The essential features of the FOC objective prism facility are listed in Table 5 and illustrated schematically in Figure 15 for the F/96 FUVOP. The left hand side of this diagram corresponds to a view of the F/96 extended format in the same orientation as the one shown in Figure 6 and approximately to scale. The direction of dispersion of the prism is represented by the vector $\overrightarrow{I}$ emanating from the center C_{96} of the format and making an angle θ with −L with θ increasing clockwise from −L. The spectrum of an object located at C_{96} will lie along the line defined by $\overrightarrow{I}$. The position of any specific wavelength is defined then by giving the linear coordinate x in pixels from C_{96} on this line with negative values for positions above C_{96} (towards +L), positive below it (towards −L) consistent with the $\overrightarrow{I}$ directions shown in Figure 15.

A blow-up of this spectrum extending from 1200 to 6000 Å as dispersed by the FUVOP is shown on the right hand side of this figure where the solid curve gives the position x along $\overrightarrow{I}$ of any wavelength for this case. The reciprocal of the slope of this curve yields the resolution R in Å/pixel given in the figure for several representative wavelengths. Values of the linear coordinate $x(\lambda)$, $R(\lambda)$, $T(\lambda)$ the transmission of the prism and the value of θ for

each prism is listed in Table 5 as a function of wavelength. Please note that the angle θ for the F/96 prisms increases clockwise from −L while it increases counterclockwise from −L for the F/48 prisms due to the different orientation of the F/48 format shown in Figure 7. The position of the entire dispersed FOV with respect to the undispersed FOV is also shown in Figure 15. The former is displaced upwards by 5.88 millimeters at the red limit at 6000Å at the upper edge and 9.96 millimeters at the far UV limit at 1200Å at the lower edge of the field.

An overall view of the F/48 objective prisms' geometrical configurations is shown in Figure A6 in the Appendix. In this 512 × 512 centered format, the star is placed at position *U* in the field (undispersed position) and dispersed by the NUVOP, the FUVOP and the FOPCD as indicated. The data were obtained during ground based calibration using a point source and a *Zn* emission line source.

It should also be apparent from an inspection of Figure 15 and Table 5 that careful consideration must be given to the positioning of the format and/or the target object in the format in order to ensure that the ensuing spectrum falls on the correct part of the frame. This is especially critical for the FUVOP's that have a large offset and a spectrum length which is a sizeable fraction of a typical field of view. The simplest way to handle this problem is through judicious use of the POS TARG special requirement described in the Proposal Instructions. Suppose, for example, that one desires to place a particularly interesting feature in the spectrum of an object located at $\simeq$ 1500 Å close to the center of the standard F/96 512 × 512 format listed in Table 6 using the FUVOP. According to the data given in Table 4 and the situation illustrated in Figure 15, one would specify a POS TARG 0, −6.9 because 1500Å falls 312 pixels or 6.9 arcseconds from the undispersed position of the object in the negative Y(or L) direction specified on Figure 7a of the Proposal Instructions.

Another possibility that does not involve any, possibly uncertain, movement of the target and is particularly suited to the situation in which one wishes to take a first exposure of the target without dispersion to establish the exact geometry of a complex field involves the use of the 512 × 512 –UF format listed in Table 6. This places the undispersed object at the position $S \simeq 512$, L$\simeq$ 256. Then, the dispersed exposure with the F/96 FUVOP can be specified for the standard 512 × 512 –DF format where 1200Å would fall around L = 670 and 3000Å around L = 506, comfortably within the central regions of this field.

3.5.3 Polarizers

The FOC polarimeter consists of three MgF_2 double Rochon prisms located on FW1 in the F/96 relay. Each prism consists of an optically contacted double Rochon prism combination acting as a three element birefringent beam splitter. The pass directions of the prisms are at 0°, 60°, and 120°. A schematic drawing of the device is shown in Figure 16.

Table 5. FOC Objective Prism Characteristics

F/96 FUVOP $\theta = 9°$ x(pix);R(Å/pix) T	F/96 NUVOP $\theta = 6°$ x(pix);R(Å/pix) T	F/48 FUVOP $\theta = 12°$ x(pix);R(Å/pix) T	F/48 NUVOP $\theta = 12°$ x(pix);R(Å/pix) T	F/48 FOPCD $\theta = 100°$ x(pix);R(Å/pix) T	λ(Å)
−415;1.3 0.44					1200
−360;2.6 0.58		−183;5.1 0.61		−208;5.1 0.62	1300
−330;4.5 0.64		−168;8.8 0.69		−191;8.8 0.70	1400
−312;7.0 0.73		−159;13.7 0.76		−181;13.7 0.76	1500
−300;9.9 0.85		−153;19.5 0.82		−174;19.5 0.82	1600
−292;13.2 0.88		−149;25.9 0.86		−169;25.9 0.86	1700
−285;16.0 0.91	−325;– 0.77	−145;33.0 0.9	−50;– 0.78	−165;33.0 0.9	1800
−279;20.7 0.92	−230;– 0.79	−142;40.7 0.92	−46;– 0.79	−161;40.7 0.91	1900
−275;25.0 0.93	−147;4.0 0.8	−140;49.2 0.92	−32;15.7 0.8	−159;49.2 0.92	2000
−271;29.8 0.95	−113;2.7 0.82	−138;58.6 0.94	−19;10.5 0.82	−157;58.6 0.93	2100
−268;35.1 0.95	−78;3.0 0.83	−137;69.0 0.95	−11;11.6 0.84	−156;69.0 0.94	2200
−261;54.7 0.96	−1.4;5.3 0.86	−133;107.6 0.96	5;20.9 0.86	−151;107.6 0.96	2500
−255;103 0.96	64;10.7 0.88	−130;203 0.96	23;41.8 0.88	−148;203 0.96	3000
−251;177 0.94	101;17.4 0.94	−128;348 0.97	33;67.9 0.89	−145;348 0.96	3500
−249;282 0.94	125;25.3 0.94	−127;554 0.98	40;99 0.89	−144;554 0.97	4000
−246;606 0.94	155;43.0 0.94	−125;1192 0.98	47;168 0.89	−142;1192 0.97	5000
−245;1117 0.92	175;63.3 0.9	−125;2192 0.98	52;247.5 0.85	−142;2197 0.85	6000

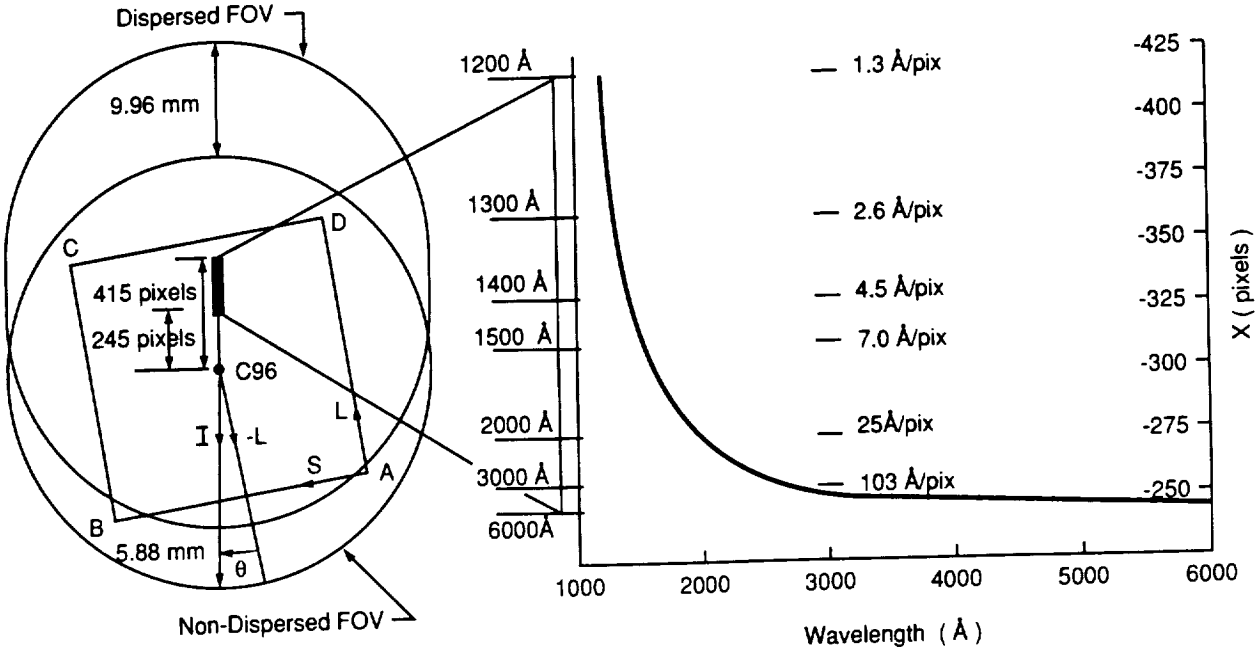

Figure 15. Optical layout of the F/96 focal plane with the FUVOP inserted in the beam. The star is assumed located at C_{96} in the entrance aperture of Figure 6.

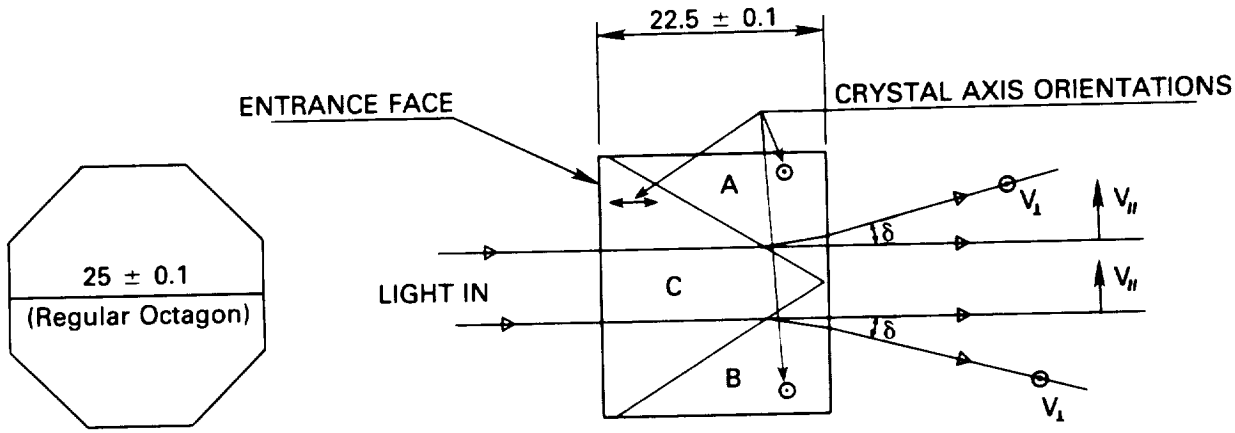

Figure 16. The Physical Layout of the FOC Polarizers. Dimensions are in millimeters.

The optical axes of the outer components A and B are oriented perpendicular to the optical beam axis while the central component C has its optical axis parallel to the beam axis. The entrance face is at the apex of the central prism. In this configuration, the ordinary ray is transmitted without deviation while the extraordinary rays are deviated by the interface between the outer and central prisms. Thus, three exit beams emerge from the polarizer. The orientation of polarization is parallel to the face of the octagon to within

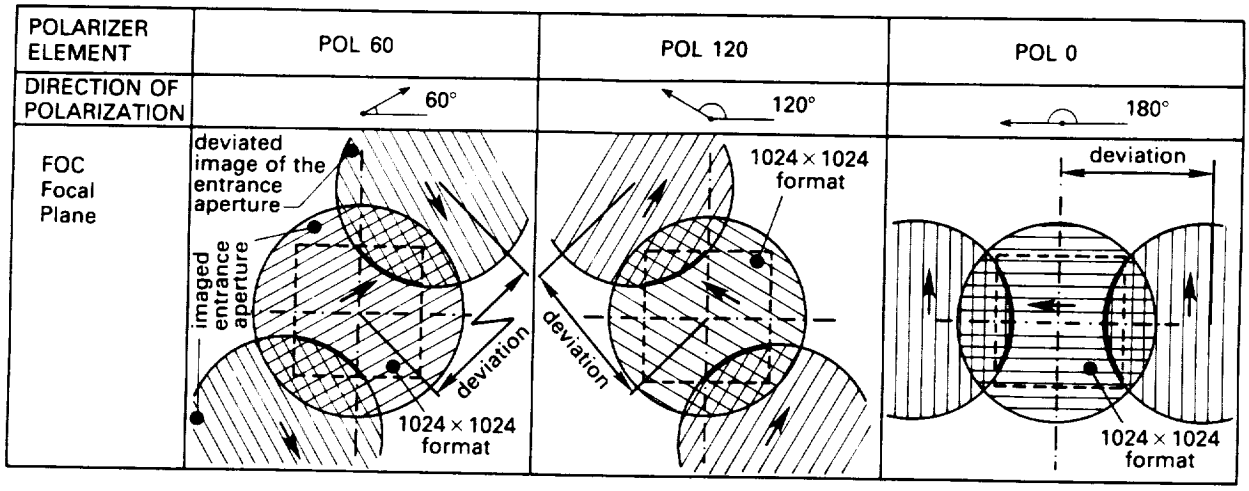

Figure 17. Image Configurations on the F/96 Focal Plane for the Three Polarizers.

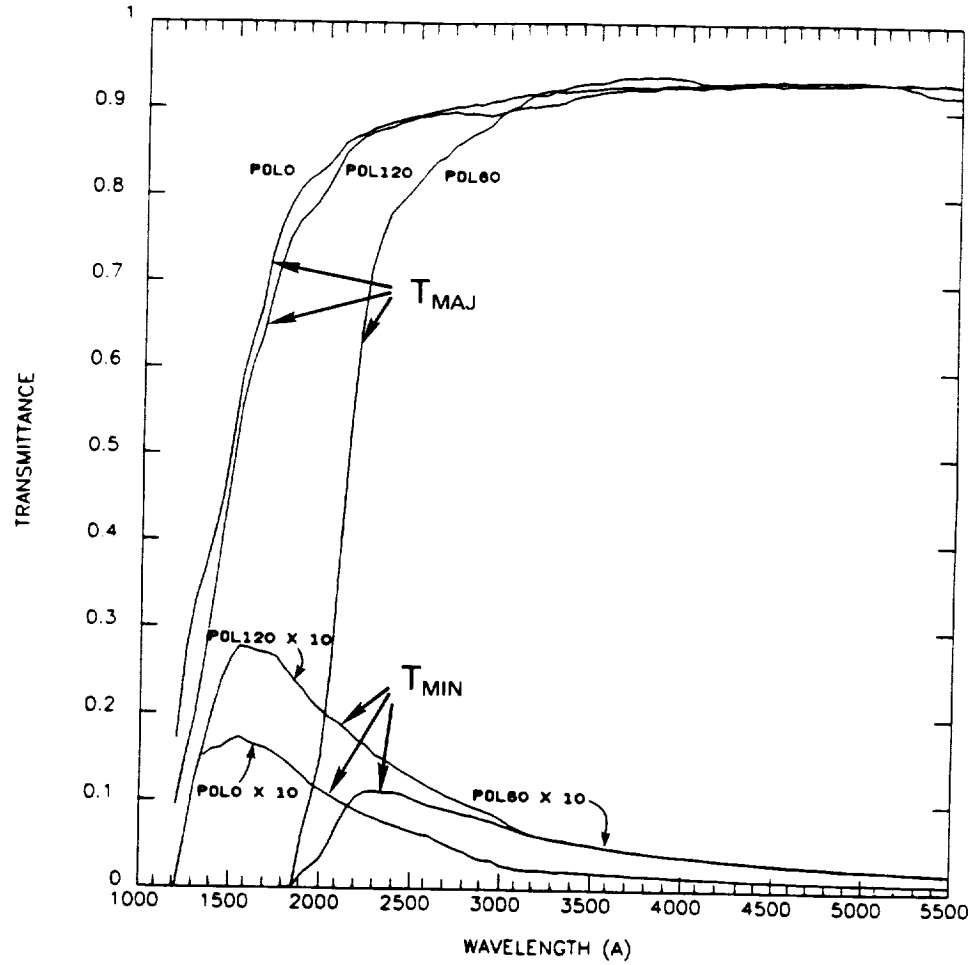

Figure 18. The major principal transmittance T_{MAJ} and the minor principal transmittance T_{MIN} of the three FOC polarizers as a function of wavelength.

$\pm$ 5 arcminutes and the external faces are parallel to within $\pm$ 5 arcseconds. This insures that the wavefront distortion is less than $\lambda/10$ at λ 6328Å. The beam deviation δ depends on the ordinary and extraordinary indices of refraction and the prism wedge angle. These parameters were chosen such that the angular separation of the beams will yield a central undeviated 11 arcseconds squared image without overlap of the two orthogonally polarized beams. Thus, $\delta = 1.155°$ for λ =1300Å and 1.165° for λ =6328Å. In these conditions, the images on the F/96 focal plane will be located as shown in Figure 17 for the three prisms.

The major principal transmittance (T_{MAJ}) of the undeviated beam through the three prisms and the minor principal transmittance (T_{MIN}) of the normal nonpolarized light are given in Figure 18. Notice that one of the polarizers (POL60) does not transmit below $\simeq$ 1800Å.

3.6 LONG SLIT SPECTROGRAPHIC FACILITY

This facility consists of the following four elements:

1. a rectangular (0.1 $\times$ 20 arcsecond) slit placed on the F/48 camera entrance aperture at the OTA tangential focus as shown in Figure 6,
2. order sorting bandpass filters and/or a cross dispersing objective prism on the F/48 filter wheels,
3. a removable toroidal convex mirror which picks off the F/48 beam between the folding mirror and the DHU and reflects it towards
4. a fixed spherical concave reflection grating which reimages the slit spectrum onto the DHU photocathode as shown in Figure 4.

The last two optical elements are slightly tilted and decentered with respect to the F/48 optical relay axis in order to center the spectrum of the slit onto the photocathode. Since, as shown in Figure 7, the slit is considerably offset from the extended 44$\times$44 arcseconds squared normal imaging F/48 field, its image falls outside the scanned area of the photocathode in the normal F/48 imaging mode. Only when the convex mirror is placed into the F/48 beam does the dispersed image of the slit become visible on the scanned area in the position indicated in Figure 7. The effective wavelength range of the device in first order is 3600–5400Å, in second 1800–2700Å, in third 1200–1800Å and in fourth 900–1350Å. The MgF_2 window of the detector limits this last range to 1150-1325Å.

The spectrograph mirror and the grating are both made of Zerodur overcoated with Al + MgF_2 with a reflection efficiency exceeding 0.7 beyond 1200Å. The grating is ruled with 150 grooves mm^{-1} and a blaze angle of 1.94° for maximum efficiency at 4500Å in first order. Its radius of curvature is 94cm and the angle of diffraction is 2.6°. This implies a linear dispersion at the photocathode of 71, 36, 24, and 18 Å mm^{-1} and, with a beam diameter of $\simeq$ 20 mm., a theoretical resolving power of $\simeq$ 3000, 6000, 9000 and 12000 for the four orders,

respectively. The FOC spectrograph resolution, however, is limited, in practice, by the slit size and the OTA Point Spread Function (PSF) that correspond to $\simeq$ 2 to 3, 24 micron pixels. Using the Rayleigh resolution criterion, the actual resolving power of the instrument is $\simeq$ 1150 in all orders with a spectral resolution of 4, 2, 1.3, and 1Å for first, second, third, and fourth orders respectively. These values have been confirmed by ground-based calibration using line source stimulation.

Both the spectrograph mirror and the grating work with unit magnification. The convex mirror corrects the astigmatism introduced by the spectrograph's optical elements. The resulting image is nearly free of astigmatism and image tilt with respect to the photocathode plane. The only residual aberration is a pseudo coma given by the relay working in an off-axis condition. An image taken in $512z \times 1024$ format when the spectrograph was illuminated by a mercury lamp is shown in Figure A5 of the Appendix.

The fixed grating configuration of the long slit spectrograph implies that light from all orders falls simultaneously on the same area of the detector. Because of the limitations of the UV bandpass filters, any order may be contaminated with light from another, resulting in possible ambiguities in line identification and degradation of achievable signal to noise ratio (S/N) due to line or continuum overlap. This can be a serious problem in some applications, especially those involving objects with a bright visible spectrum where the spectrograph's overall quantum efficiency peaks.

Even in the most complicated situations, however, it is still possible, at least in principle, to separate the different orders by executing a number of exposures with judiciously chosen bandpass filters. Light from the first order, for example, can be unambiguously identified by means of the F305LP filter that completely blocks radiation below 3000Å. Since the filter transmissions are well known, shorter wavelength information can be recovered from a confused spectrum by appropriately subtracting the calibrated data. The F220W for the second order, F150W for the third and F140W for the fourth may be considered as the standard FOC spectrograph order sorting filters but others may be selected, at the discretion of the observer, instead of or in addition to these for more specialized applications. This procedure can always be used at the expense of increased observation time required by the multiple exposures and of degraded S/N due to the effectively increased background uncertainty. For extended sources larger than 1.6 arcsecond in size this is the only viable alternative.

For objects of limited spatial extent (including point sources), the four overlapping orders can be spatially separated by using the FOPCD objective prism as a cross disperser. The position of the four orders on the F/48 detector field in this case is shown in Figure 19. The prism dispersion direction PD is orthogonal to the grating dispersion direction GD and close to antiparallel to the increasing sample number direction S. The reader is referred to Figure 7 for a broader perspective of this viewing configuration. The largest achievable

physical separation between orders is 0.33 arcseconds between the first (I) and second (II), 0.68 arcseconds between the second and third (III) and 1.63 arcseconds between the third and fourth (IV) order. The background is significant only for wavelengths which are harmonics of bright geocoronal lines like OI, 1304Å. This option is very attractive because of its high efficiency due to the spectral multiplex gain of a factor of 4 and to the gain of a factor of 3 – 5 resulting from the elimination of the bandpass filters. The CaF_2 blocking filter on the FOPCD effectively removes the contaminating effect of the bright geocoronal line at Lyman α at 1216Å.

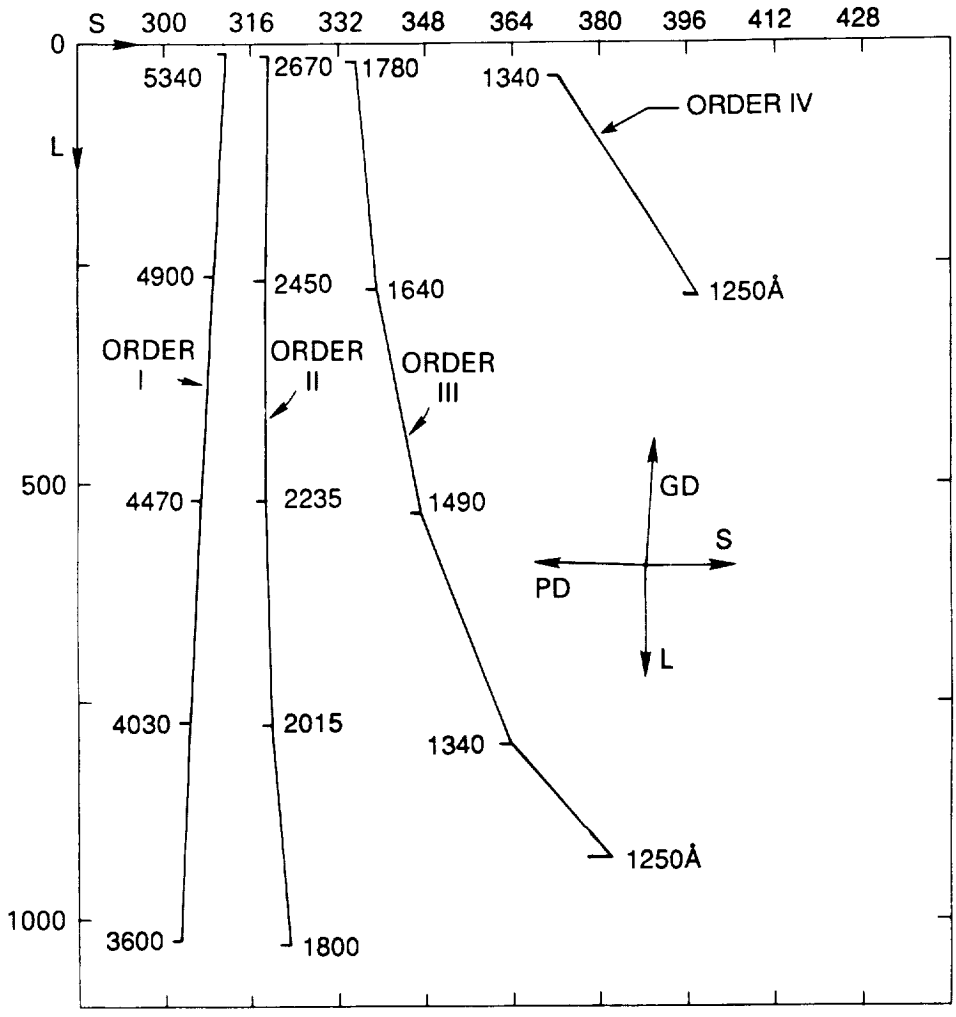

Figure 19. Optical layout of the F/48 focal plane in the spectrograph mode and the FOPCD in the beam. The coordinates are line numbers (L) as ordinates and sample numbers (S) as abscissae. Notice the different scales for S and L.

The open area to the right of the dotted line in the F/48 extended format in the spectrograph mode shown in Figure 7 and Figure A5 of the Appendix is normally blanked out by selecting the $256z \times 1024$ format with initial sample and line positions 160 and 0 as shown in Figure A7 of the Appendix. It should be kept in mind, however, that dispersed light from this part of the aperture is still falling on the photocathode and, if the field here is very bright (a bright galactic nucleus, or the central part of a nebula, for example), some contamination of the right edge of the slit spectrum due to scattering should be expected. On the other hand, this area can be exploited for slitless high spatial and spectral resolution observations of compact sources. For this purpose, the user should specify the standard format 512×1024-CD described in Table 6.

Provided the undispersed source is placed with a POS TARG special requirement near the end of the opaque spectrograph finger in the F/48 image aperture shown in Figure 7, a full two dimensional series of quasi monochromatic images of the object will appear in this special format which has the initial sample and line positions set at 512,0. Because of the 7.2 arcseconds offset of the slit from the finger along the L direction, the wavelength range covered by the slitless mode is slightly different than that of the standard slit mode *i.e.*, $\simeq$ 3300 to 5100Å in first, 1650 to 2550Å in second, 1150 to 1700Å in third and 1150 to 1275Å in fourth. The slitless mode is, obviously, most advantageous when dealing with compact line emission sources that minimize the risk of overlapping monochromatic image contamination and is not recommended for extended continuum sources. One important advantage of the slitless mode for point sources is the elimination of the uncertain slit function which depends on the OTA PSF at the time of observation and the accuracy of the target acquisition procedure that places the object on the narrow spectrograph slit.

3.7 DETECTORS

The transfer optics described in section 3.1 relays the image produced on the OTA focal plane to the photocathode of a two dimensional photon counter drawn schematically in Figure 20. The detector consists of three basic parts: a three stage image intensifier tube, a coupling lens, and a TV camera tube.

3.7.1 Image Intensifier and Coupling Lens

The intensifier is an EMI 9614 three stage tube magnetically focussed by means of a permanent magnet. The first-stage photocathode (like the following two) is a hot bialkali for the highest quantum efficiency in the UV-blue region and the lowest dark-count rate at 17°C. It has a useful diameter of 40mm and is deposited on a MgF_2 input window.

The photoelectrons generated at the first stage are accelerated by a 12 kilovolt potential and impinge on a P11 phosphor layer coupled by a 4 micron thick mica membrane to the second photocathode. This amplification process is repeated in the second and third stages

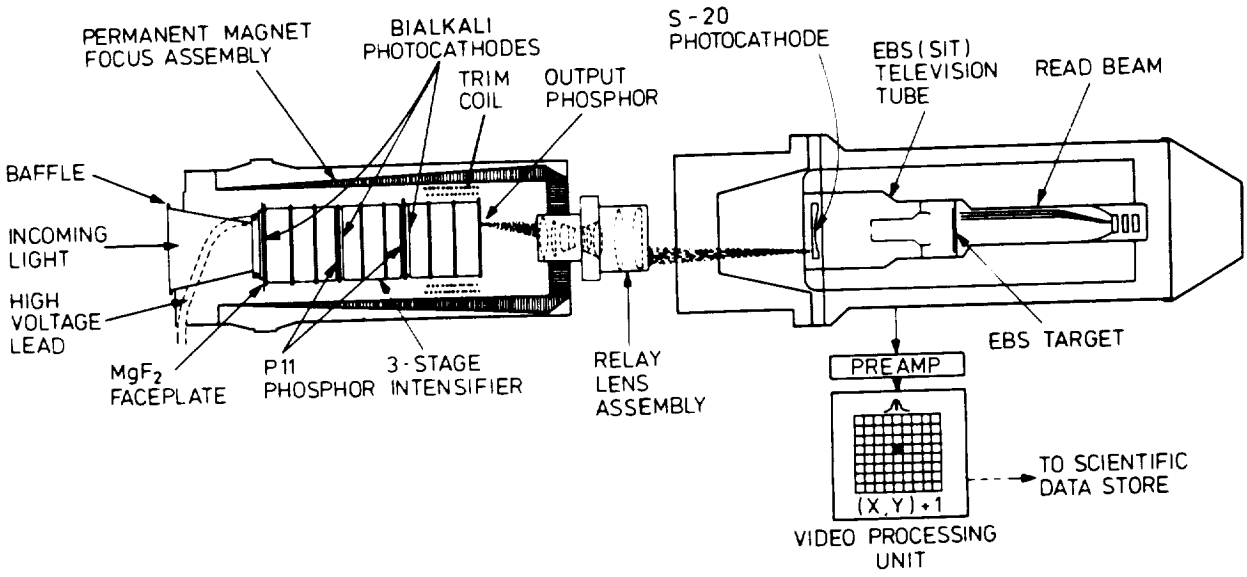

Figure 20. Physical Layout of the Imaging Photon Counting Detectors

to achieve an overall photon gain of 1.3 $\times 10^5$. Focussing of the intensifier electrons is accomplished with a carefully shaped permanent magnet assembly and a trimcoil is added around the third stage for fine adjustments.

The limiting spatial resolution of the intensifier is 35 line-pairs per millimeter. The dark current at an ambient temperature of 17° C is less than 10 counts cm^{-2} s^{-1} (10^{-4} counts $pixel^{-1}$ s^{-1} in the normal mode). Both of these characteristics are essentially limited by the first stage of the intensifier tube.

A lens assembly consisting of 9 components in a double Gaussian design is used to transfer the image from the output phosphor of the intensifier to the fibre-optic faceplate of the TV camera. It is designed to operate at f/2.7 with a slight magnification (1.15) to compensate for the demagnification of the image intensifier. The 80% energy width for point object images varies between 22 and 35 microns over the whole of the useful area and the light transmission is more than 60%.

3.7.2 TV Tube

The camera tube is a Westinghouse WX32719 low-light TV tube. This is a high-sensitivity, high resolution EBS tube (Santilli and Conger in *Photo-Electronic Devices*, AEEP, ed. L. Marton, **33A**, 1972) with a 25 millimeters square diode array target, magnetic

focus and deflection coils and an electrostatically focussed image section with a 40 millimeter diameter useful photocathode area. The S-20 photocathode is evaporated onto the concave inner surface of the input fibre-optic faceplate. The emitted photoelectrons are accelerated by a potential of up to 12 kilovolts and focussed onto the target which is an N-type silicon wafer with diffused P-type regions arranged in an hexagonally-packed diode array.

During operation each diode is reverse biased. Incoming photoelectrons generate electron-hole pairs which discharge the diodes. An amplified charge pattern corresponding to the image is then stored in the diodes. The charge flowing in the target lead, when the scanning beam recharges the diodes, is the signal current. The target gain is about 2500 and the modulation transfer function is 50% at 8 line-pairs per millimeter. The video signal coming from the TV tube is amplified by the preamplifier and then transmitted to the Video Processing Unit (VPU).

3.8 VIDEO PROCESSING UNIT

Each camera has its dedicated VPU which accepts the amplified signals from the camera preamplifier. The purpose of the VPU is to determine the x-y centroid of each event, determine if a true photon event has occurred and to increment the SDS memory address corresponding to the location where the photon event was detected. During any one scan of a frame of duration of 30 milliseconds for the 512 × 512 format down to 520 microseconds for the smallest 64 × 64 format there will only be a few scattered photon events. A photon event is typically a spot with a diameter of 3 or 4 pixels. It is read by the scanning beam on successive lines of the raster scan. Figure 21 illustrates how such a signal would look using the z axis to represent the magnitude of the charge.

As a line is scanned, a gaussian shaped pulse is produced. As successive lines are scanned, additional pulses, corresponding to slices of the event, increase in peak amplitude until a maximum is reached. The pulse amplitude then decreases. This video signal is amplified and presented to the VPU which takes the incoming video lines and produces two signals needed to analyze the waveform, Peak Signal and Extent Signal. The Peak Signal corresponds to the point of maximum amplitude of an event on a single scan line or slice. The Extent Signal is used to determine the time or extent of the event during a single line.

A true photon event is present on several successive lines. Analysis of these events characterized by the peak and extent signals on successive lines is the task of the VPU. By using delay lines and shift registers, each event is examined in a 4 × 9 pixel area by real time analysis so that the same event on successive lines can be analyzed. The z dimensional event center is tagged in the x and y direction. The Pattern Recognition Logic analyzes the event's shape to determine true photon events and reject other noise and ion events.

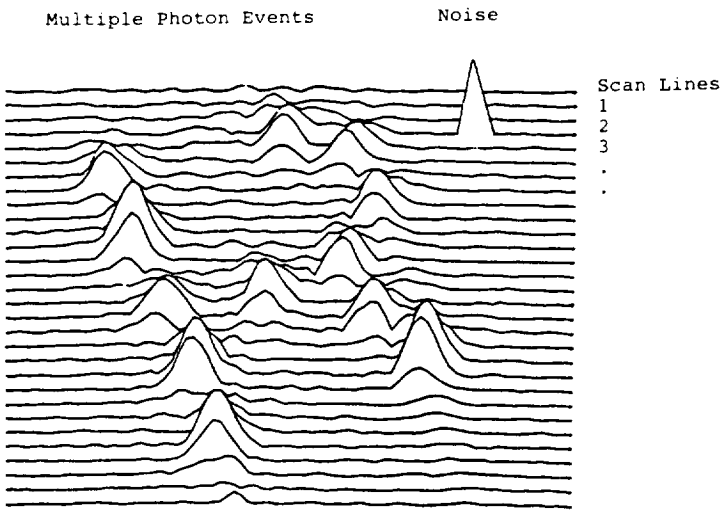

Figure 21. Schematic Drawing of a Typical Raster Scan Output of the Detectors

3.9 SCIENCE DATA STORE

As an event is detected and classified as valid, the video processing unit causes the science data store (SDS) to increment by one the memory location corresponding to the event centroid. The image is gradually built up over the exposure time. After stopping the exposure, the SDS can be read out without disturbing the stored image, if desired. The SDS can accept a 512 × 512 line image in the 16 bit word mode or a 512 × 1024 line image in the 8 bit word mode. The cycle time for the SDS is compatible with the camera scan rate of $\geq 10^6$ pixels per second. This rate is maintained for all formats and zoom. In this latter mode, the camera read beam scans the target twice as fast in the line direction as it does in the normal imaging mode but the pixels are twice as long. The detector generates an increment command for every pixel in which a photon event has been detected. A scan of 256K pixels occurs in less than 30 milliseconds while a scan of 4K pixels (*i.e.*, a 64 × 64 pixel squared format) takes place in approximately 512 microseconds.

There are two sets of SDS electronics (SDS-1 and SDS-2), with unit 1 dedicated to the F/48 camera and unit 2 to the F/96 camera. The SDS memory is physically divided into 22 modules of 16K 16-bit data words each holding 32 words from each of 512 lines, but only 16 modules are active at any given time. These 16 modules are accessed in sequence to reduce the required memory cycle time. Each SDS word has 22 bits, with the extra 6 bits being used for "single-bit" error correction and "two-bit" error detection. Included in the engineering telemetry are error detection and correction bits set for each logical module. If more than 6 SDS memory modules fail, the memory can still be operated in a reduced data mode. In this case, zeros will appear in the downlink for those modules that are not available. Data loss occurs from the "right-hand" side, so if only 15 modules are up, words 0-479 for each of the PDA lines of 512 pixels would be obtained.

The SDS can be operated in either the normal imaging mode or the SDS dump mode so it is necessary to interrupt the pixel increment commands from the detector to read out the SDS memory to the downlink. Each readout is a dump of the 256K 16-bit words of SDS memory, and hence contains 4M data bits regardless of the image format. Readout of science data is normally done under control of the NSSC-1, which controls the gating of signals to the Remote Interface Unit (RIU) of the SI C&DH including the Science Data Formatter (SDF). From the SDF, the data is fed to the downlink or the tape recorder. For target acquisition, however, the science data is dumped to the NSSC-1 which uses the information in a 64 pixels $\times$ 60 lines image to calculate the location of the "point" with the maximum count number.

4.0 OBSERVING ARRANGEMENTS

4.1 IMAGING, OCCULTATION AND SPECTROGRAPHIC MODES

Operationally, the observation of an astronomical source with the FOC is defined once the following physical parameters are specified:

1. The configuration or optical relay (F/96 or F/48 camera)
2. The positions of the filter wheels (4 for the F/96, 2 for the F/48 camera)
3. The HRA position (in or out of F/96 beam)
4. The spectrograph mirror position (in or out of F/48 beam)
5. The S×L imaging format (S≤512, L≤1024 pixels with S the number of SDS pixels in the line scan direction and L the number of SDS pixels in the increasing L direction)
6. The word length (8 or 16 bits per word)
7. The pixel size (normal 24 × 24 microns squared or zoomed 48 × 24 microns squared)
8. The position (S_0, L_0) of the starting pixel. This can be specified with a least increment corresponding to 0.25 pixel both in the S and L directions. Telemetry monitoring, however, can only verify the starting pixel with an accuracy of 32 pixels.
9. The position of the target in the chosen format.

In general, selections 5, 6, and 7 have to be made consistent with the 4 Mb SDS memory size limitation. This means that, for all practical purposes, the word length is completely defined, once the format is selected, as any format larger than 512 × 512 pixels squared will automatically require an 8-bit word length while any format of that size or less will be imaged with 16-bit words.

Obviously, only a small fraction of all the possible observational modes allowed in principle by the FOC will find practical astronomical application and, therefore, be accurately and extensively understood and calibrated prior to use. Table 6 lists the main characteristics of the anticipated standard F/96, F/288 and F/48 imaging and spectrographic observing modes. The second column in this table gives the format size (S×L), the third the pixel size in microns and arcseconds squared in the sky, the fourth the starting pixel (S_0, L_0), the fifth the word length, the sixth the zoom configuration, the seventh the overall field of view in arcseconds squared for that format, the eighth the maximum count rate per pixel N_{MAX} for that format (see section 5.2),and the last column lists the main scientific justification for the selection, the mode names used in the Proposal Instructions for HST, if appropriate, and the proposal entry required for that format. S_0 is given in the 1–1024 range on a dezoomed extended format. The format names in parentheses in the Comments column are used by the project data base to identify specific FOC apertures for calibration. These names are

used in the FOC calibration handbook to identify formats and associated calibration files and should not be confused with mode names for the exposure logsheet entries.

For the F/48 spectrographic modes, the pixel size and the FOV are given in units of arcseconds × Angstroms in first order. The pixel size (selection 7 in the list above) is considered an optional parameter in the Exposure Logsheet of the ST Proposal Forms. The default value, if none is specified, is 24 × 24 microns squared for imaging and 48 × 24 microns squared for spectroscopy. The position and orientation of the target in the aperture (selection 9) should be specified in the Special Requirements column of the Exposure Logsheets.

4.2 TARGET ACQUISITION MODES

Three acquisition modes are available for use with the FOC as described in the Proposal Instructions: INTeractive ACQuisition (Mode I), ONBOARD ACQuisition (Mode II), and blind pointing (Mode III). In addition, an EARLY ACQuisition can be specified where an examination of the field is necessary prior to science exposures to help measure a target in a crowded field or to determine a slit alignment angle, for example.

4.2.1 Mode I Target Acquisition - INTeractive ACQuisition

Designed to be the most accurate acquisition procedure for use with the coronographic fingers, the slit or small image formats, this procedure requires the involvement of the observer, in real-time, to identify the field and measure the center of the target on an FOC image. First, using a blind pointing acquisition, the target is placed in a standard field of view and an image is taken, with instrument parameters such as filters and exposure time selected by the user. The resulting image of the field is then read down for immediate display in the Observation Support System (OSS) area at ST ScI. Once the observer identifies the target using an interactive image display system and measures the target position from the display screen, a slew request is generated and up-linked, and the telescope is maneuvered to place the target in the selected destination. There is no verification of the subsequent field unless specifically requested by the observer on the exposure logsheets.

INTeractive ACQuisition is expected to be the standard acquisition procedure for OCC mode. For the long slit spectrograph, which has a slit width of only 0.1 arcseconds, INTeractive ACQuisition is the only safe way to ensure proper centering of a point source. The procedure also may be useful in IMAGE mode when an object needs to be placed in a particular place in one of the imaging apertures or when using very small fields of view.

In OCC mode, objects of 9th magnitude or brighter require a more accurate INTeractive ACQuisition strategy to ensure the safety of the detector. The following steps will be automatically scheduled whenever an INTeractive ACQuisition is required with a target brighter than 9th magnitude:

TABLE 6
F96 IMAGE or OCC Modes

Format (FxL)	Pixel size (μm^2) (arcsec^2)	Offset (S_0,L_0)	Word Length	Zoom	FOV (arcsec^2)	N_{MAX} (cs^{-1})	Comments/Proposal Entry
512×1024	50×25 (0.044×0.022)	0,0	8 bit	on	22×22	0.16	Largest FOV. IMAGE or OCC Mode. 512 × 1024, PIXEL = 50 × 25, (X96ZLRG)
512×1024	25×25 (0.022×0.022)	256,0	" "	off	11×22	"	Largest FOV with highest resolution IMAGE Mode. 512 × 1024, (X96NLRG)
512×512	"	256,256	16 bit	"	11×11	0.33	Highest photometric accuracy. IMAGE Mode. 512 × 512, (X96N512)
512×512	"	0,512	" "	"	"	"	Covers 0.4″ coronographic finger. OCC Mode. 512 × 512–F0.4, (X96N512_4)
512×512	"	421,0	" "	"	"	"	Covers 0.8″ coronographic finger. OCC Mode. 512 × 512–F0.8, (X96N512_8)
512 × 512	"	256,0	" "	"	11 × 11	0.33	Undispersed format for FUVOP, 512 × 512–UF, (X96N512_UF)
512 × 512	"	256,512	" "	"	" "	0.33	Dispersed format for FUVOP, 512 × 512–DF, (X96N512_DF)
256×256	"	384,384	" "	"	5.6×5.6	1.3	Wider dynamic range, highest photometric accuracy. IMAGE Mode. 256 × 256, (X96N256)
"	"	128,640	" "	"	"	"	Covers 0.4″ Coronographic finger. OCC Mode. 256 × 256–F0.4, (X96N256_4)
"	"	549,12	" "	"	"	"	Covers 0.8″ Coronographic finger. OCC Mode. 256 × 256–F0.8, (X96N256_8)
128×128	"	448,448	" "	"	2.8×2.8	5.3	Widest dynamic range. IMAGE Mode. 128 × 128, (X96N128)

Table 6 (continued)

F/48 IMAGE Modes

Format (FxL)	Pixel size (μm^2) (arcsec^2)	Offset (F_0,L_0)	Word Length	Zoom	FOV (arcsec^2)	N_{MAX} (cs^{-1})	Comments/Proposal Entry
512×1024	50×25 (0.088×0.044)	0,0	8 bit	On	44×44	0.16	Largest FOV. (X48ZLRG) 512 × 1024, PIXEL = 50 × 25
512×1024	25×25 (0.044×0.044)	256,0	" "	Off	22× 44	"	Largest FOV with highest resolution. 512 × 1024 (X48NLRG)
512×512	"	256,256	16 bit	"	22×22	0.33	Highest photometric accuracy. 512 × 512, (X48N512)
256×256	"	384,384	" "	"	11×11	1.3	Wider dynamic range. 256 × 256, (X48N256)
128×128	"	448,448	" "	"	5.6×5.6	5.3	Widest dynamic range. 128 × 128 (X48N128)

TABLE 6 (continued)

F/48 SPEC Modes

Format (FxL)	Pixel size (μm^2) (arcsec×Å)	Offset (F_0,L_0)	Word Length	Zoom	FOV (arcsec×Å)	N_{MAX} (cs^{-1})	Comments/Proposal Entry
512×1024	50×25 (0.088×1.8)	0,0	8 bit	On	44×1800	0.16	Widest field for main aperture correction. 512 × 1024–SLIT (X48ZLRGS)
512×1024	25×25 (0.044×1.8)	256,0	" "	Off	22× 1800	"	Highest spatial and spectral resolution with widest spectral range. 512 × 1024, PIXEL = 25 × 25 (X48NLRGS)
512 × 1024	"	512,0	" "	"	" "		Slitless spectrograph format 512 × 1024–CD, PIXEL = 25 × 25 (X48NLRG_CD)
512×512	"	256, 256	16 bit	"	22×900	0.33	Highest spatial and spectral resolution with widest dynamic (X48N512S) range. 512 × 512–SLIT, PIXEL = 25 × 25
256×1024	50×25 (0.088×1.8)	160,0	"	On	22×1800	"	Widest dynamic and spectral range. 256 × 1024–SLIT (X48ZRECS)
256×1024	25×25 (0.044×1.8)	384,0	" "	Off	11×1800	"	Widest dynamic range and highest (X48NRECS) spatial resolution. 256 × 1024–SLIT, PIXEL = 25 × 25

TABLE 6 (continued)

F/288 IMAGE or OCC Modes

Format (FxL)	Pixel size (μm^2) (arcsec^2)	Offset (F_0,L_0)	Word Length	Zoom	FOV (arcsec^2)	N_{MAX} (cs^{-1})	Comments/Proposal Entry
512×1024	50×25 (0.015×0.007)	0,0	8 bit	On	7.6×7.6	0.16	Largest FOV. IMAGE or (X28ZLRG) OCC Mode. 512 × 1024, PIXEL = 50 × 25
512×1024	25×25 (0.007×0.007)	256,0	" "	Off	3.8×7.6	0.33	Largest FOV with highest resolution. IMAGE Mode. 512 × 1024 (X28NLRG)
512×512	"	256,256	16 bit	"	3.8×3.8	0.33	Highest photometric accuracy. IMAGE Mode. 512 × 512 (X28N512)
512×512	"	152,460	" "	"	"	"	Covers the coronographic finger. OCC Mode. 512 × 512–F0.4 (X28N512_4)
256×256	"	280,588	" "	"	1.9×1.9	1.3	Widest dynamic range and highest photometric accuracy. IMAGE Mode. 256 × 256 (X28N256_4)

- Step 1 will be the first INTeractive ACQuisition exposure taken with sufficient neutral density and colour filters to ensure the FOC is operating in a safe regime. The image is downlinked to OSS where the observer has a decision time of 15 min. to identify the target on the displayed FOC image. The conclusion of this step will be the maneuver of the telescope to place the target on the chosen finger. As for the normal INTeractive Acquisition, configuration and exposure times for the acquisition image are selected by the user.
- Step 2 will be a verification exposure, in OCC mode, with the aperture centered on the selected finger, again using neutral density and colour filters to avoid over-illumination in case the target is not correctly centered on the finger. This second exposure will also be read down to OSS where the user will quickly verify the result of the initial maneuver.
- If the target has been successfully acquired under the finger the program will start the first science OCC exposure without the neutral density filters. If the acquisition has failed, the observation is not performed. No possibility exists, at the moment, to calculate and execute a second correction manouver in case the first is not successful.

The interactive nature of this acquisition, requiring TDRSS links, means that the procedure is classed as a "limited resource" in the Proposal Instructions. Furthermore, our initial testing of the acquisition procedure suggests that it is extremely time consuming for the user, and therefore must be used only when strictly required. The current estimates of the overhead times give 40 minutes for the normal target Mode I TA, and about 1 hour for the bright target Mode I.

4.2.2 Mode II Target Acquisition – ONBOARD ACQuisition

Onboard acquisition is designed for point-source acquisitions in OCC and SPEC modes and can only be used in conjunction with either the F/96 0.4 arcseconds or 0.8 arcseconds coronograph finger or the F/48 slit. Note that no onboard acquisition to the 0.4 arcseconds finger is possible in the F/288 mode. The procedure is fully automatic with no real-time intervention and no target verification after the acquisition. The execution time for a Mode II TA is currently estimated to be $\simeq$ 10 minutes.

The method proceeds as follows. First, the target is placed in the Mode II target acquisition aperture by blind pointing. Each coronograph finger and the slit has its own acquisition aperture (128×128 pixels camera format) which is located close to the appropriate destination. See Table 7 for a complete list. The initial size of the acquisition aperture is 2.8 × 2.8 arcseconds squared in F/96 and 5.6 × 5.6 arcseconds squared in F/48, although the target must fully lie within the central 64 × 60 pixels squared area. Next, the image is read out from the FOC Science Data Store and read into the NSSC-1 where it is reduced in size to 1.4 × 1.3 arcseconds squared in the case of the F/96 relay. The resulting image is

smoothed and then searched to find the pixel with the largest number of counts. This pixel represents the center of the target and is the basis for the subsequent small angle maneuver of the telescope with the slew calculation based on detector coordinates of the target and finger or slit. In principle, it is also possible to acquire a reference object and then slew to the target, assuming that the user provides the precise offset between the two. No pattern recognition, image modelling, or "peak-up" is used by this procedure.

Upon completion of the procedure, no automatic validation is carried out to check whether the target has indeed gone to the required location. Where necessary, the user may want to carry out a verification exposure; if so, the exposure will have to be specified on the exposure logsheet. Because of the risk to the detector due to over-illumination, ONBOARD ACQuisition cannot be used for targets of 9th magnitude or brighter without real-time verification (see Mode I).

The procedure works strictly in detector coordinates; without in-flight experience it is not possible to state how accurately the coronograph fingers and slit position can be defined in the detector coordinate frame and their long term stability. The additional concern associated with the finite probability of successfully blind pointing the target in such a small size acquisition aperture makes the use of Mode II risky especially in the early phases of the mission. After launch, the procedure will be fully tested and, after Science Verification, we should have a more accurate evaluation of its performance.

4.2.3 Mode III Target Acquisition – Blind Pointing

Mode III is the default acquisition procedure for the FOC. When no target acquisition is specified in the Special Requirements section on the proposal exposure logsheets, the telescope performs a straight-forward blind pointing on the coordinates provided by the user. After the acquisition, no explicit verification of the target position in the fields of view aperture is performed. No overhead time in addition to the guide stars lock time is charged to the user for this acquisition.

Mode III is expected to be the standard acquisition procedure for IMAGE mode in all three instrument configurations, FOC/48, FOC/96, and FOC/288 for most fields of view except the smallest (< 3 arcseconds squared size), providing the target has a coordinate position measured with the Guide star selection system Astrometric Support Package (GASP) ensuring best accuracy with respect to the guide star astrometric catalogue. The procedure will not be useful for point sources in either OCC or SPEC modes, at least early in the mission, because blind pointing is unlikely to provide the precision needed to accurately place a target on the F/48 slit (width = 0.1 arcseconds) or on one of the coronographic fingers. However, for extended objects where accurate pointing is not important, blind pointing can be used. Again, targets of magnitude 9 and brighter cannot be acquired on the fingers using blind pointing. In this case, see Mode I.

4.2.4 EARLY ACQuisition

When necessary, it is possible to take an acquisition image some time before the scientific observation. The acquisition image can be used for a better identification of the field, or a better evaluation of the source flux, etc. In order to update the observation parameters, a minimum turnaround time of two months is necessary between the acquisition and the science exposure.

Presently, the system does not have the capability to select for the science observation the same pair of guide stars successfully used for the acquisition exposure, thus eliminating the possibility of using the acquisition image to measure the target coordinates at the accuracy level required to perform, for example, a blind pointing on the F/48 0.1 arcseconds slit. This capability might be available after the first year after launch, providing, therefore, an efficient alternative to INTeractive ACQuisition for all the observations requiring SPEC mode.

4.3 THE FOC TARGET ACQUISITION APERTURES

For convenience, a number of special formats to be used in the Mode I and II acquisition exposures have been defined. These formats (listed in Table 7) have offsets that have been chosen in order to optimize the small angle maneuvers necessary to move the targets to the required locations, and are different for each Mode. Their position will be well calibrated during SV and monitored for stability and electronic distortions to ensure good pointing accuracy.

For Mode I, in addition to the usual centered formats, a number of acquisition formats which are conveniently located close to the 0.4 arcseconds and 0.8 arcseconds fingers (F/96), and to the F/48 slit finger have been defined. Different sizes are available for each of these combinations, but it is strongly recommended to use the larger images due to the initial position error of the targets coordinates with respect to the Guide Stars ($\simeq$ 0.33 arcseconds). For the acquisition to the F/48 spectrographic slit, the SF formats are required with the optional parameter PIXEL= 50×25.

For Mode II, only the 128×128 format can be chosen. As for Mode I, different offsets have been defined to place the onboard acquisition formats conveniently close to the 0.4 arcseconds and 0.8 arcseconds fingers, and to the F/48 slit finger.

Table 7; Target Acquisition Formats

Relay	Name	Size	USE
Mode I Target Acquisition and Early Acquisition			
F/96	512×512-A0.4	512×512	0.4″ finger
F/96	256×256-A0.4	256×256	0.4″ finger
F/96	128×128-A0.4	128×128	0.4″ finger
F/96	512×512-A0.8	512×512	0.8″ finger
F/96	256×256-A0.8	256×256	0.8″ finger
F/96	128×128-A0.8	128×128	0.8″ finger
F/288	512×512-A0.4	512×512	0.4″ finger
F/288	256×256-A0.4	256×256	0.4″ finger
F/288	128×128-A0.4	128×128	0.4″ finger
F/48	512×512-SF	512×512	0.1″ slit
F/48	256×256-SF	256×256	0.1″ slit
F/48	128×128-SF	128×128	0.1″ slit
Mode II Target Acquisition			
F/96	128×128-A0.4	128×128	0.4″ finger
F/96	128×128-A0.8	128×128	0.8″ finger
F/48	128×128-ASLIT	128×128	0.1″ slit

5.0 INSTRUMENT PERFORMANCE

5.1 THE POINT SPREAD FUNCTION (PSF)

At any wavelength λ in millimeters, the maximum frequency signal transmitted by the FOC is $(\lambda F)^{-1}$ cycles per millimeter, if F is the focal ratio of the appropriate relay (F=48, 96 or 288). Consequently, the minimum or critical sampling rate required to satisfy the uniform sampling theorem in this case is $2(\lambda F)^{-1}$ pixels per millimeter at the FOC focal plane. This last quantity is plotted as a function of λ for the three relays in Fig. 22. From this figure, it is apparent that the F/288 relay oversamples the system PSF for $\lambda > 1750$Å, the F/96 relay only for $\lambda > 5200$Å and the F/48 relay undersamples the system PSF for all wavelengths in the FOC bandpass. The radius of the Airy disk $(1.22\lambda/D)$ corresponding to the unobstructed circular OTA aperture varies between $0.067''$ at $\lambda = 6400$Å at one end of the FOC range to $0.013''$ at $\lambda = 1200$Å at the other. In principle, *i.e.*, if the OTA+FOC optical system were absolutely perfect, one would expect $\simeq 60\%$ of the incident radiation from a point source to fall within this radius and, therefore, the FOC to be able to obtain high S/N oversampled images at the telescope diffraction limit in most of its UV-visible operating range.

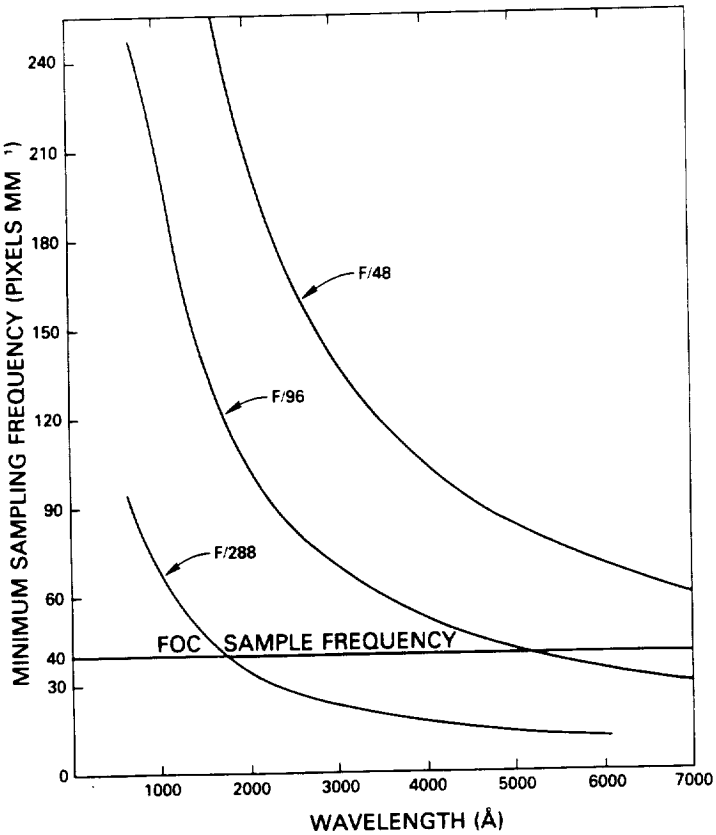

Figure 22. The minimum sampling rate required to uniquely determine the source function as a function of wavelength for the three optical relays in the FOC.

In practice, of course, the situation is not that straightforward owing to the image degrading effects of beam obstructions, aberrations, figure and position errors, pointing jitter, dust on the mirrors and mirror surface defects. Reliable estimates of the magnitude of most of these effects can be obtained by calculations using the most up-to-date information available on manufacturing specifications, tolerances, and techniques, interferometric and reflectance measurements of the optical surfaces or strategically placed witness samples and the known optical prescription of the entire optical system. A detailed discussion of the optical modelling procedures and data can be found in the OTA Instrument Handbook. Schematically, the real PSF is obtained by first using a commercial ray tracing package to trace rays geometrically through the OTA+FOC optical system over a 22×22 grid of points in the field of view at specified wavelengths using the known positions, aspheric coefficients, tilts, decenters, curvatures and refractive indices of every optical surface. This first step produces spot diagrams at the FOC focal plane and the wavefront error (WFE) defined as the deviation of the true corrugated wavefront from the corresponding spherical wavefront over the exit pupil or in other words, the optical path difference of the specified ray from the chief ray. Zernike polynomials are used to best fit analytically the WFE obtained this way.

The next step is to compute a wavefront map on a user-specified grid using the Zernike polynomials. Then, a function that contains this wavefront map as a phase and the aperture function consisting of the spider arms, mirror pads, secondary mirror obstruction etc. as an amplitude is constructed. The Fourier transform of this function yields the complex amplitude spread function (ASF) on which must be superposed the effects of dust, pointing jitter and mirror surface irregularities. The amplitude squared of the ASF gives the critically sampled PSF while a resampling onto and integration over the appropriate FOC pixels finally leads to the expected fractional monochromatic PSF. This PSF can be used as input to the FOC simulator FOCSIM (see section 7) to generate the actual counts per second per pixel expected from any specific point source through any of the FOC observing configurations provided the bandpass is narrow enough to permit the use of a representative monochromatic PSF. This technique is expected to give good results for all the category M and N filters for which the appropriate PSF is chosen to be that corresponding to the peak wavelength of the overall response but much poorer results for the wideband optical elements.

The largest uncertainty in this whole procedure stems from the treatment of the primary mirror surface irregularities. The formally correct procedure would be to compute the ASF by Fourier transforming the convolution of the WFE at the exit pupil with the precise mirror ripple power spectrum. Unfortunately, however, only the expectation value of this spectrum is known with any kind of accuracy. Consequently, it is easier to compute the product of the amplitude squared of the Fourier transform of the WFE and ripple spectrum. The final result is an ensemble average PSF pertaining to many different primary mirrors rather than to the specific HST primary. The PSF computed this way could closely

approximate reality if the mirror ripples were to randomly vary during a long exposure due to minute thermal or mechanical stresses.

The PSF obtained this way is shown in Figure 23 for the three relays and three representative wavelengths from the far UV to the red. The nine panels shown in this figure each represent a 64 × 64 pixel squared image of point sources obtained with FOCSIM (see section 7) and whose fluxes are chosen such that both the total number of counts from the source and the maximum count rate in the central pixel (5 counts sec^{-1} $pixel^{-1}$) are the same for each relay. This normalization ensures that variations in system response with wavelength are corrected for and do not influence the comparison of various wavelength images. In all cases, a nominal HST jitter of 7 milliarcseconds FWHM, a zodiacal light background of 100 S10, a detector background of 5×10^{-4} counts s^{-1} $pixel^{-1}$ and a PSF centered on the center $x = 32$, $y = 32$ pixel are assumed.

The upper row of images corresponds to the expected point source images through the F140W, F275W and F430W filters on the F/48 relay. The field of view (FOV) of the individual images displayed in the upper row correspond to 2.8 × 2.8 arcseconds squared. The display scale is logarithmic from 0 to 5000 counts at the peak of the F275W image. The middle and lower rows of images correspond to the expected point source images through the F140M, F307M, and F502M filters on the F/96 and F/288 relays, respectively. In these two cases, the FOV displayed correspond to 1.4 × 1.4 and 0.45 × 0.45 arcseconds squared, respectively. The total number of counts under the PSF from the sources used in the simulation is 1.4×10^4 for F/48, 3.1×10^4 for F/96, and 2.3×10^5 for F/288. Clearly, the best image quality with the brightest and narrowest central peak occurs in the range 2500–3000Å. The expected improvement in image quality in the far UV ($\lambda < 2500$Å) is somewhat offset by undersampling and, especially, by the severe redistribution of light from the core to the wings of the profile due to scattering caused by the mirror irregularities. The high background evident in the F430W, F/48 image is due to its high sensitivity to zodiacal light. For brighter objects or longer integrations, it is expected that the effect of the OTA secondary mirror support spiders is to produce spikes in four orthogonal directions inclined at 33° to the L direction.

A more quantitative perspective on these issues is obtained by examination of the data shown in Figures 24a–c and in Tables 8–10. The azimuthally averaged number of counts per pixel around the central pixel as a function of the number of pixels from the center is plotted in Figures 24 for the F/48(a) F/96(b) and F/288(c) relays for each of the three images shown in Figure 23. The numbers listed in Tables 8–10 correspond to the energy fraction of the PSF contained within an increasingly larger area of size n pixels around and centered on the central pixel at various wavelengths from 1200 to 6130Å for the three relays for normal unzoomed pixels. Thus, the first row in these tables represents the energy fraction intercepted by the central pixel by itself ($n = 1$), the second row the energy fraction

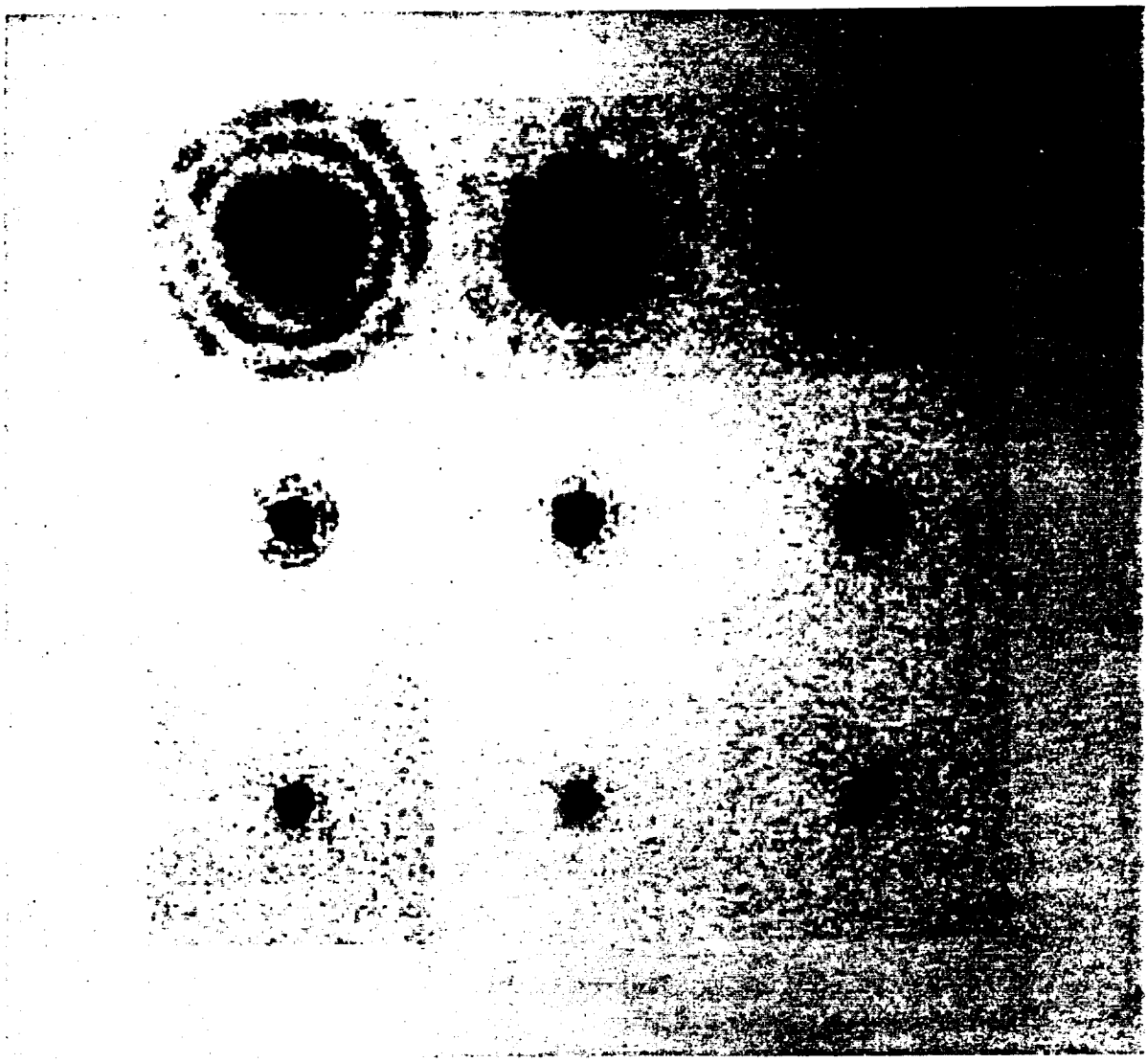

Figure 23. The expected point source images in the F/48 (top row), F/96 (middle row) and F/288 (bottom row) relays for three representative wavelengths: far UV (left column, middle UV (middle column), and visible (right column).

intercepted by the central 3×3 pixel squared area ($n = 9$), the third row that intercepted by the central 5×5 pixel squared area ($n = 25$) and so on. The second column gives the radial distance from the central pixel in arcseconds defined as the radius of the circle having the same area as the corresponding box. The sharply increasing fraction of light lost from the core to the wings with decreasing wavelength is quite evident from this data.

The ensemble average PSF used in this simulation, although perfectly adequate for most applications, does have the drawback that it tends to wash out the effects of the

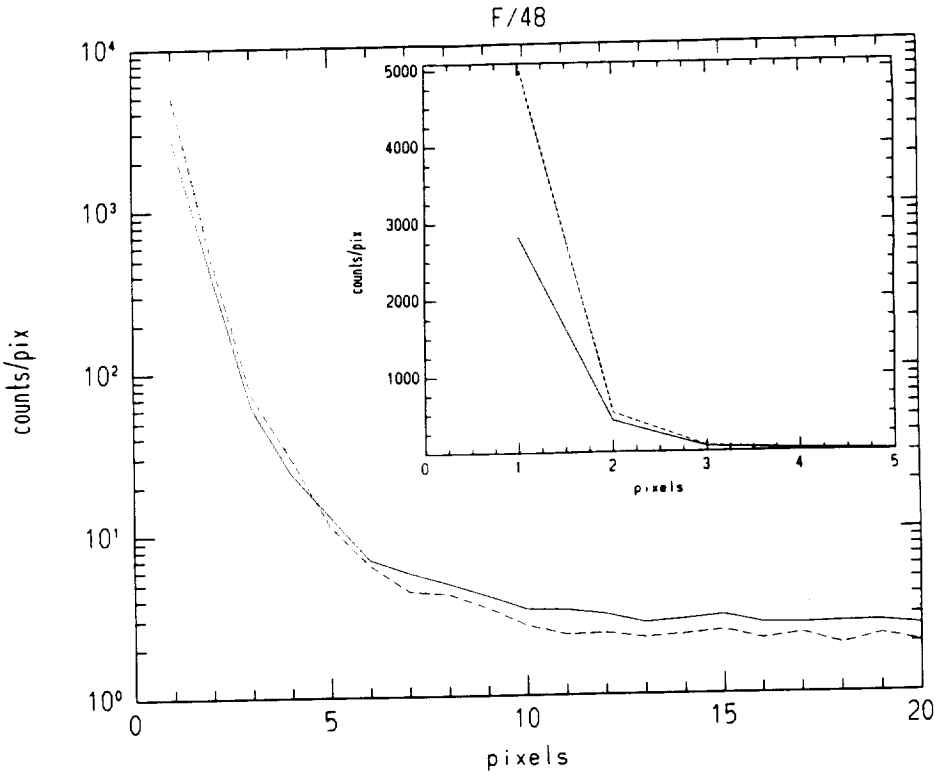

Figure 24*a*. Azimuthally averaged number of counts per pixel around the central pixel of the point sources shown in the top row of Figure 23 for the F/48 relay. The solid line represents the F140W, the dashed line the F275W and the dotted line the F430W filters. The inset on the upper right of this figure shows the F/48 PSF on a linear scale near the core. Each pixel is 44 milliarcseconds in size.

expected interference fine structure (speckles) of the actual PSF. These speckles should have a characteristic diameter of $\simeq 0.02$ arcseconds at 2000Å, a contrast of almost 100% and enclose, perhaps, $\simeq 1\%$ of the total energy. This type of pattern is expected to be particularly noticeable in F/288 images where a speckle is oversampled by a 3×3 grid of 0.007 arcsecond pixels and where the deviations from the simulation described become critical. For this reason the expected PSF for the HRA for a specific but realistic primary mirror ripple distribution has been estimated. To obtain the ripple diffraction distorted wavefront, they added together the distorted wavefronts corresponding to three different gaussian-shaped low pass filters having plausible mean ripple sizes, standard deviations and relative powers. The total power in the ripples down to a minimum size of 2 cm was assumed to be 2500 waves cm^2 as suggested by the OTA Handbook. These normalized wavefronts were then multipled by the pupil mask derived from the system ASF computed in the standard way at 2200Å. An inverse Fourier transform finally yields the aberration and ripple distorted PSF for these input conditions. The resultant speckled PSF and the corresponding ensemble average PSF

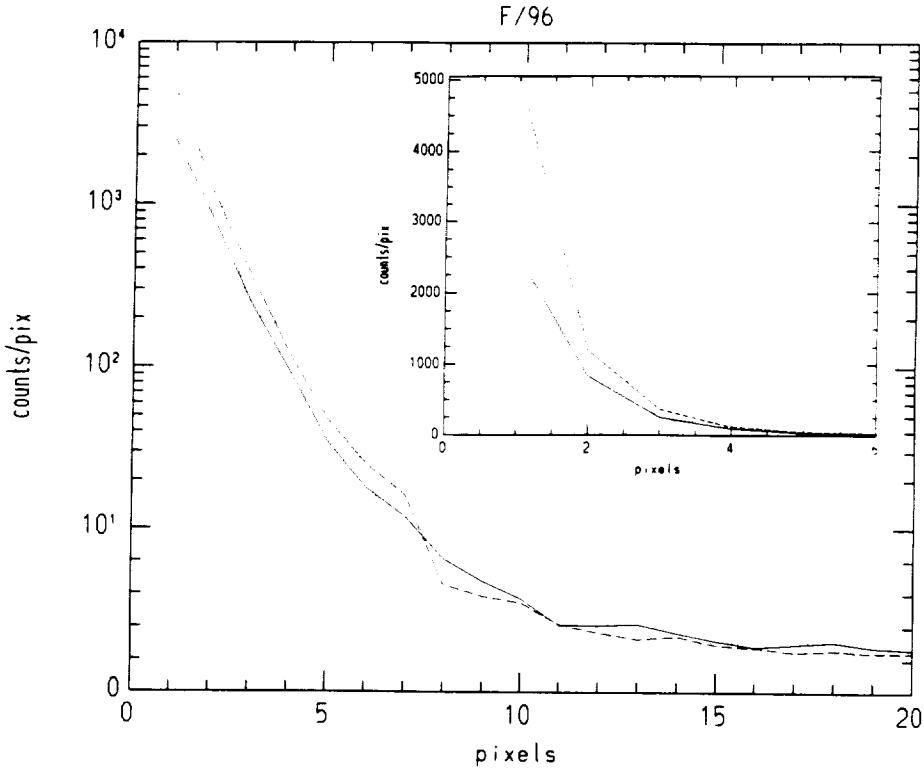

Figure 24*b*. Azimuthally averaged number of counts per pixel around the central pixel of the point sources shown in the middle row of Figure 23 for the F/96 relay. The solid line represents the F140M, the dashed line the F307M and the dotted line the F502M filters. The inset on the upper right of the figure shows the F/96 PSF on a linear scale near the core. Each pixel is 22 milliarcseconds in size.

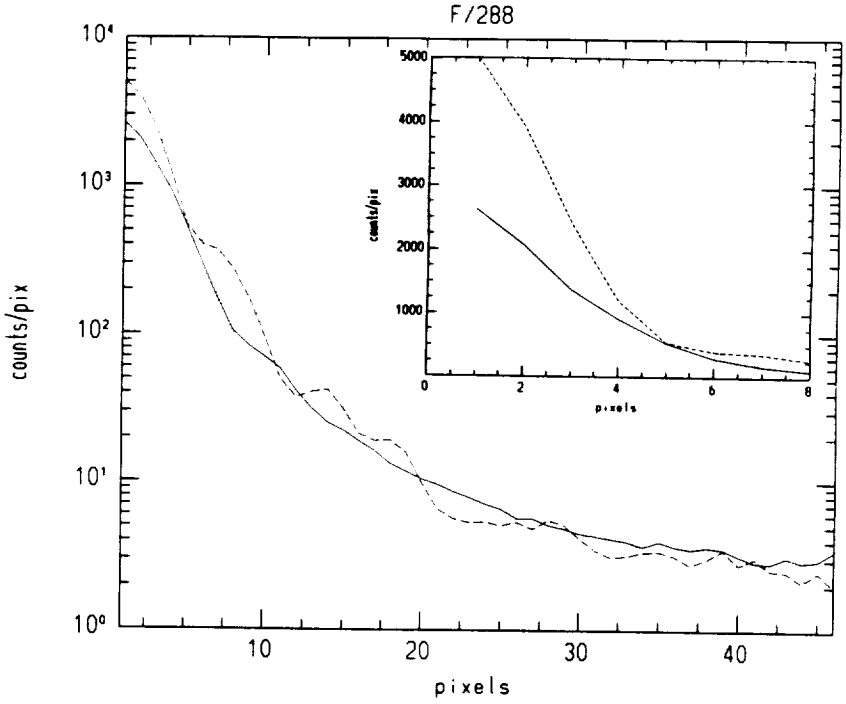

Figure 24*c*. Same as Figure 24*b* for the F/288 relay. Each pixel is 7 milliarcseconds in size.

for the F/288 relay computed in the standard way are shown in Figures 25*a* and *b*. The azimuthally averaged PSFs for the two cases are plotted as a function of distance from the center in Figure 26.

It is worth emphasizing here that the simulated speckled PSF for the HRA shown in Figure 25, although certainly closer to reality than the average one, is still only one possibility out of many. The actual one can only be determined in orbit after extensive calibrations with standard sources of differing brightness. Moreover, the effect of ripples of size smaller than 2 cm is not taken into consideration at all in the speckled simulation. Thus, a detailed comparison of what are probably the two extreme cases presented here yields the following conclusions. The simple ensemble average PSFs, examples of which are shown in Figures 23 and 24, should be quite realistic representations of the actual imaging situation for both the F/48 and F/96 relays out to a few tenths of an arcsecond essentially because of the clearly undersampled or marginally sampled speckle pattern in these cases. Beyond that, the increasing effect of small ripples on the wings of the PSF render any simulations rather uncertain with errors as large as a factor of up to ten or more at large distances (> 0.5 arcseconds) to be expected. Precise calculations of the observability of a faint source near a bright object based on these considerations alone, therefore, should be used with some caution. The HRA, on the other hand, does require a more realistic PSF for sophisticated simulation especially if image enhancement techniques such as roll deconvolution or speckle masking are applied to significantly affect faint source detectability. Finally, background levels in the vicinity of a bright object in the HRA given by the curves shown in Figure 26 should fall, in reality, somewhere in between the two extreme cases. This critical parameter can only be inferred from observation but this figure is useful in indicating the possible uncertainty range as a function of radial distance.

Figure 25*a*. The expected image of a point source in the F/288 relay at 2200Å using the ensemble average PSF and an integrated ripple power of 2500 waves cm^2.

Figure 25*b*. The expected image of a point source in the F/288 relay at 2200Å using a specific ripple power distribution with an integrated power of 2500 waves cm^2.

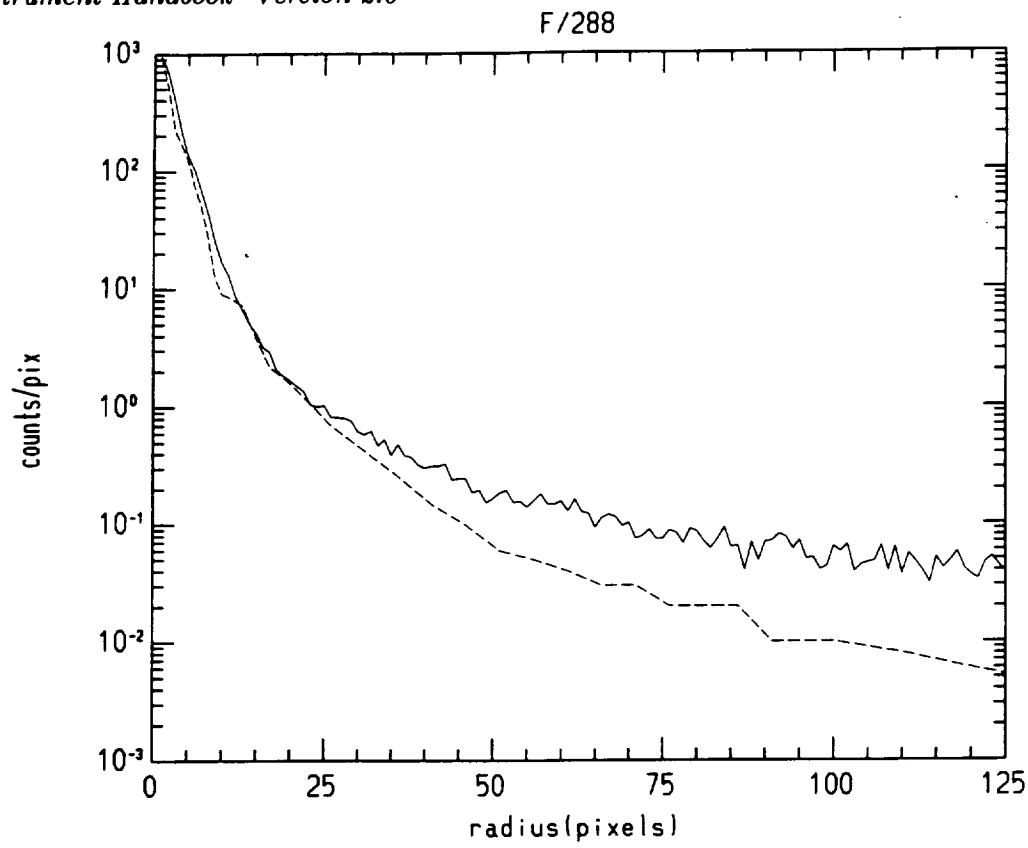

Figure 26. Azimuthally averaged number of counts per pixel around the central pixel for the two cases shown in Figures 25*a* and *b*. The solid line is the ensemble average case, the dashed line represents the specific ripple case. Each pixel is 7 milliarcseconds in size.

Table 8. Expected energy fraction $\epsilon(\lambda)$ for F/48 relay. Pixel centered. Normal pixel.

n	r''	1200Å	1440Å	1720Å	2060Å	2460Å	2960Å	3550Å	4260Å	5110Å	6130Å
1	0.025	0.15	0.20	0.26	0.30	0.34	0.37	0.37	0.36	0.32	0.27
9	0.074	0.34	0.44	0.52	0.58	0.63	0.67	0.69	0.68	0.64	0.60
25	0.124	0.40	0.50	0.58	0.65	0.71	0.74	0.76	0.78	0.79	0.79
49	0.174	0.43	0.53	0.61	0.68	0.74	0.77	0.80	0.81	0.81	0.82
81	0.22	0.45	0.55	0.63	0.70	0.75	0.79	0.82	0.84	0.84	0.84
121	0.27	0.47	0.56	0.65	0.72	0.77	0.80	0.83	0.85	0.86	0.86
169	0.32	0.48	0.58	0.66	0.73	0.78	0.81	0.84	0.86	0.86	0.87
225	0.37	0.50	0.59	0.67	0.74	0.78	0.82	0.85	0.86	0.87	0.88
289	0.42	0.51	0.60	0.68	0.74	0.79	0.83	0.85	0.87	0.88	0.88
361	0.47	0.53	0.61	0.69	0.75	0.80	0.83	0.86	0.88	0.89	0.89
441	0.52	0.54	0.62	0.69	0.76	0.80	0.84	0.86	0.88	0.89	0.90
529	0.57	0.56	0.63	0.70	0.76	0.81	0.84	0.87	0.88	0.90	0.90
625	0.62	0.57	0.64	0.71	0.77	0.81	0.84	0.87	0.89	0.90	0.90
729	0.67	0.59	0.65	0.72	0.77	0.81	0.85	0.87	0.89	0.90	0.91
841	0.72	0.61	0.66	0.72	0.78	0.82	0.85	0.87	0.89	0.90	0.91

Table 9. Expected energy fraction $\epsilon(\lambda)$ for F/96 relay. Pixel centered. Normal pixel.

n	r''	1200Å	1440Å	1720Å	2060Å	2460Å	2960Å	3550Å	4260Å	5110Å	6130Å
1	0.012	0.05	0.08	0.11	0.14	0.16	0.16	0.15	0.13	0.11	0.08
9	0.037	0.22	0.30	0.37	0.42	0.45	0.47	0.48	0.49	0.48	0.45
25	0.062	0.32	0.41	0.49	0.55	0.60	0.64	0.64	0.61	0.58	0.57
49	0.087	0.36	0.46	0.55	0.61	0.66	0.69	0.72	0.73	0.71	0.66
81	0.11	0.39	0.49	0.57	0.65	0.70	0.73	0.75	0.77	0.78	0.76
121	0.14	0.40	0.51	0.59	0.66	0.72	0.76	0.78	0.79	0.80	0.80
169	0.16	0.42	0.52	0.61	0.68	0.73	0.77	0.80	0.81	0.81	0.81
225	0.19	0.43	0.53	0.62	0.69	0.74	0.78	0.81	0.82	0.82	0.82
289	0.21	0.44	0.54	0.63	0.70	0.75	0.79	0.82	0.83	0.84	0.83
361	0.24	0.45	0.55	0.63	0.70	0.76	0.80	0.82	0.84	0.85	0.85
441	0.26	0.46	0.56	0.64	0.71	0.76	0.80	0.83	0.84	0.86	0.85
529	0.29	0.47	0.57	0.65	0.72	0.77	0.81	0.83	0.85	0.86	0.86
625	0.31	0.48	0.57	0.65	0.72	0.77	0.81	0.84	0.86	0.86	0.87
729	0.34	0.49	0.58	0.66	0.73	0.78	0.82	0.85	0.86	0.87	0.87
841	0.36	0.50	0.59	0.66	0.73	0.78	0.82	0.85	0.86	0.87	0.88

Table 10. Expected energy fraction $\epsilon(\lambda)$ for F/288 relay. Pixel centered. Normal pixel.

n	r''	1200Å	1400Å	1800Å	2100Å	2460Å	2960Å	3550Å	4260Å	5110Å	6130Å
1	0.004	0.007	0.010	0.016	0.02	0.021	0.021	0.019	0.016	0.013	0.010
9	0.012	0.05	0.07	0.11	0.14	0.15	0.16	0.15	0.13	0.11	0.08
25	0.021	0.11	0.16	0.22	0.25	0.28	0.30	0.31	0.28	0.25	0.20
49	0.029	0.17	0.23	0.31	0.34	0.37	0.40	0.41	0.41	0.38	0.33
81	0.036	0.22	0.30	0.38	0.42	0.45	0.46	0.47	0.48	0.47	0.44
121	0.047	0.26	0.35	0.44	0.48	0.51	0.53	0.52	0.52	0.52	0.51
169	0.053	0.28	0.38	0.49	0.54	0.57	0.59	0.58	0.56	0.55	0.55
225	0.063	0.31	0.40	0.52	0.57	0.61	0.63	0.63	0.61	0.58	0.57
228	0.070	0.32	0.42	0.54	0.59	0.63	0.67	0.68	0.66	0.62	0.59
361	0.080	0.34	0.44	0.56	0.61	0.65	0.69	0.71	0.70	0.67	0.62
441	0.087	0.35	0.45	0.57	0.63	0.67	0.70	0.73	0.73	0.71	0.66
529	0.097	0.36	0.46	0.58	0.64	0.68	0.72	0.74	0.75	0.74	0.70
625	0.103	0.37	0.47	0.59	0.65	0.69	0.73	0.75	0.76	0.76	0.73
729	0.113	0.37	0.48	0.60	0.65	0.70	0.74	0.76	0.77	0.78	0.76
841	0.120	0.38	0.48	0.60	0.66	0.71	0.75	0.77	0.78	0.79	0.78
961	0.128	0.39	0.49	0.61	0.67	0.71	0.75	0.77	0.79	0.79	0.79
1089	0.136	0.39	0.49	0.61	0.67	0.72	0.76	0.78	0.79	0.80	0.80
1225	0.144	0.40	0.50	0.62	0.68	0.72	0.76	0.79	0.80	0.81	0.81
1369	0.152	0.40	0.50	0.62	0.68	0.73	0.77	0.79	0.80	0.81	0.81

5.2 DYNAMIC RANGE

5.2.1 Uniform Illumination

The maximum count rate per pixel for spatially uniform illumination depends on the pixel scan rate which is constant and equal to 8.8×10^6 pixels sec^{-1} and the size of each photon event before processing by the VPU. For a photon event size of 3×3 pixels, the count rate that will show a departure from linearity not greater than 10% will be $\simeq 0.01$ times the individual pixel scan rate. Consequently, the FOC's range of linear response extends up to:

$$N_{\text{MAX}} = \frac{8.8 \cdot 10^4}{z(S \times L)} \text{counts sec}^{-1}\text{pixel}^{-1}$$

where $z = 1$ for normal and $z = 2$ for zoomed pixels.

Beyond this value, the photometric error introduced by the saturation function correction will exceed 10%. Values of N_{MAX} for the standard FOC formats are listed in Table 6. Correct and quantifiable operation of the FOC at count rates exceeding N_{MAX} cannot presently be guaranteed. A representative intensity transfer function of the FOC for uniform illumination is show in Figure 27*a*.

5.2.2 Non-Uniform Illumination

The more point-like the object on the detector, the greater the dynamic range of the peak. The maximum linear count rate at the peak of the profile is about 10 times the N_{MAX} defined in Section 5.2.1. For an object with a roughly Gaussian profile, based on data from the F/96 and F/48 detectors and for normal 512×512-pixel-format images, the situation is summarized in Table 11a. A representative intensity transfer function of the FOC for compact sources is shown in Figure 27*b*.

Table 11a. Limiting count rates.

FWHM (pixels)	Integrated count rate at which 20% nonlinearity is reached (counts sec^{-1})	Average count rate (counts pixel^{-1} sec^{-1})
1	10	10
3.5	60	4.9
5	80	3.2
6	100	2.8
8	120	1.9
10	140	1.4
12	200	1.4

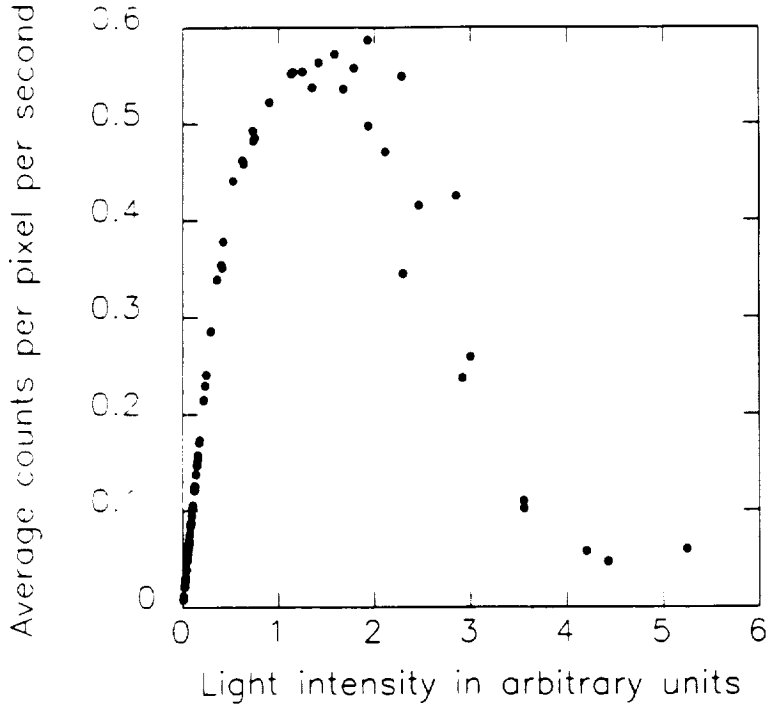

Figure 27*a*. An average intensity transfer function for the detectors in the F/48 and F/96 relays using a flat field of variable illumination.

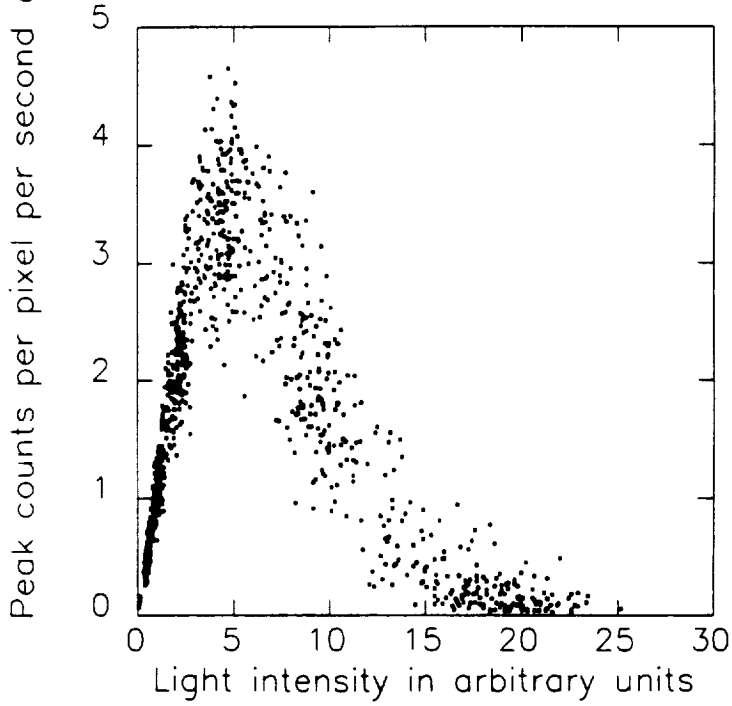

Figure 27*b*. An average intensity transfer function for the detectors in the F/48 and F/96 relay using pinhole illumination of variable intensity. The scatter is due to differing sizes of pinholes and positions on the detector in the array used for the test.

All count rates given in Table 11a and b will scale with N_{MAX} *i.e.*, they will increase as the inverse of the area of the format in pixels. The count rate for 20% nonlinearity increases as the counts are spread over a wider area, but it grows less slowly than the FWHM squared. All these numbers have an error of ±20% or less. Predictions for the F/48 chain are uncertain due to difficulties in producing a sufficiently small PSF with available ground test equipment. The PSF depends on the f-ratio and the effective wavelength. To give an idea of the scaling to be applied, the count rates and limiting magnitudes for an isolated A0V star imaged with the F430W filter are given in Table 11b. Count rates are determined by using FOCSIM (see section 7.0). Actual peak count rates may be less than these values by a factor of up to about 4 if the image peak is not exactly centered on a single pixel. Count rates half those giving 20% nonlinearity should give results with better than 10% nonlinearity, but twice the count rate will give nearer 70% nonlinearity. If the star is embedded in bright extended surroundings, the count rate at which 20% nonlinearity is reached decreases, approaching N_{MAX} as the surrounding count rate reaches N_{MAX}.

Table 11b. Limiting magnitudes.

	F/48	F/96
Peak count rate at $B = 22$ in counts pix^{-1} sec^{-1}	1.6	0.7
Integrated count rate at $B = 22$ in counts sec^{-1}	3	3
B magnitude for 20% nonlinear peaks	21	20
Estimated B magnitude limit for 20% nonlinear total counts in the star image	21	19

A simulated image of M51 taken with the F/48 camera with the 512×512 centered format at various intensity levels is shown in Figure A8 of the Appendix. Each panel represents a 161 × 115 pixel squared section of the format centered on the galaxy taken with intensities corresponding to 0.05 counts sec^{-1} $pixel^{-1}$ at the peak on the nucleus at minimuum (bottom left panel) to 7.3 counts sec^{-1} $pixel^{-1}$ at the peak at maximuum illumination (top right panel). The count rates shown are linearized *i.e.*, computed as if the response was actually linear. As expected from the size of the nuclear region of $\simeq$ 10 × 10 pixels squared and, therefore, the results shown in Figure 27*a*, saturation becomes noticeable in the 1.8 counts sec^{-1} $pixel^{-1}$ panel (top left) where the core is starting to develop a depression on

the right side and a bright arc on the left *i.e.*, on the upstream side of the beam scan direction due to beam pulling. The effect becomes very noticeable in the 2.7 and 3.6 panels where the core depression grows in size and more artifacts due to beam perturbations affect a larger area of the image. It is clear from this figure that extreme caution must be exercised when attempting to infer accurate brightness contours near the peak of the intensity tranfer functions appropriate to the size of the object as given in Table 11a and Figures 27*a* and *b*.

5.3 ABSOLUTE QUANTUM EFFICIENCY

The baseline overall (FOC + OTA) central absolute quantum efficiency $Q(\lambda)$ in counts photon^{-1} with no filters in the beam is plotted and tabulated as a function of wavelength in Figure 28 and Table 12 for the four FOC imaging and spectrographic configurations. The data represent the product of ground based measurements of the FOC absolute quantum efficiency, reflectance measurements of the OTA primary and secondary mirrors witness samples and an arbitrary dust covering factor of 10% . The values given correspond to the average response in a 31 × 31 pixel squared region at the center of the field of view of the corresponding optical chain. The spectrograph efficiency is shown for the four orders of the grating (I,II,III and IV) with no order sorting filters in the beam. Errors in the 2000–6500Å range for the imaging modes should not exceed ± 20% while for wavelengths below 2000Å they are expected to be of order ± 50%. This latter uncertainty should be applied to all the spectrograph data especially in the orders III and IV.

5.4 DETECTOR BACKGROUND

On the ground, the detector dark count rate averaged over the extended format is 6×10^{-4} counts s^{-1} pixel^{-1} or 1.2×10^{-3} counts s^{-1} pixel^{-1} for a zoomed pixel for the F/48 detector and 1.1×10^{-4} counts s^{-1} pixel^{-1} for the F/96 detector. The spatial distribution of dark counts over the extended format is quite uniform for both detectors. Shielding in the vicinity of the photocathodes of 7mm of Al equivalent is provided by a series of Carbon Fiber Reinforced Plastic blades mounted on the baffles and on the aft shroud. This shielding should insure that the contribution to the dark noise due to high energy electrons falls well below 10^{-4} counts sec^{-1} pixel^{-1} but cannot prevent high energy protons from contributing approximately 3×10^{-4} counts sec^{-1} pixel^{-1} in orbit. This contribution, moreover, could be quite variable during an orbit period especially for those orbits intersecting the South Atlantic Anomaly (SAA). In any case, expect the background not to be any less than 10^{-4} and, hopefully, not more than 10^{-3} counts sec^{-1} pixel^{-1}.

Table 12. Overall (OTA+FOC) central absolute quantum efficiency $Q(\lambda)$ in 10^{-3} counts photon^{-1}

λ(Å)	Q(F/48)	Q(F/96)	Q(F/288)	Q(SPI)	Q(SPII)	Q(SPIII)	Q(SPIV)
1150	3.6	3.6	0.9				0.5
1160	9.0	9.0	2.7				0.7
1170	13.5	13.5	3.6				0.8
1180	18.0	18.0	4.5				0.9
1190	20.7	20.7	5.4				1.1
1200	22.5	22.5	6.3			0.8	1.2
1250	31.5	31.5	9.9			1.0	1.5
1300	36.0	36.0	10.8			1.1	1.7
1400	36.0	36.0	11.7			1.4	2.0
1500	36.0	36.0	11.7			1.7	
1600	33.3	33.3	12.6			1.9	
1700	30.6	30.6	12.6			2.2	
1800	28.8	28.8	12.6		3.3	2.5	
1900	32.4	32.4	13.5		4.3		
2000	41.4	41.4	16.2		5.2		
2200	61.2	61.2	39.6		6.9		
2400	76.5	76.5	48.6		7.9		
2600	79.2	83.7	56.7		8.2		
2800	81.0	90.0	61.2		8.0		
3000	81.0	99.0	64.8				
3400	81.0	104	68.4	15			
3800	72.9	99.0	70.2	15			
4000	66.6	90.0	70.2	14.9			
4500	49.5	67.5	51.3	14.3			
5000	29.7	29.7	27.0	11.8			
5500	12.6	12.6	9.9	6.8			
6000	5.58	5.58	3.96				
6500	0.54	0.54	0.45				

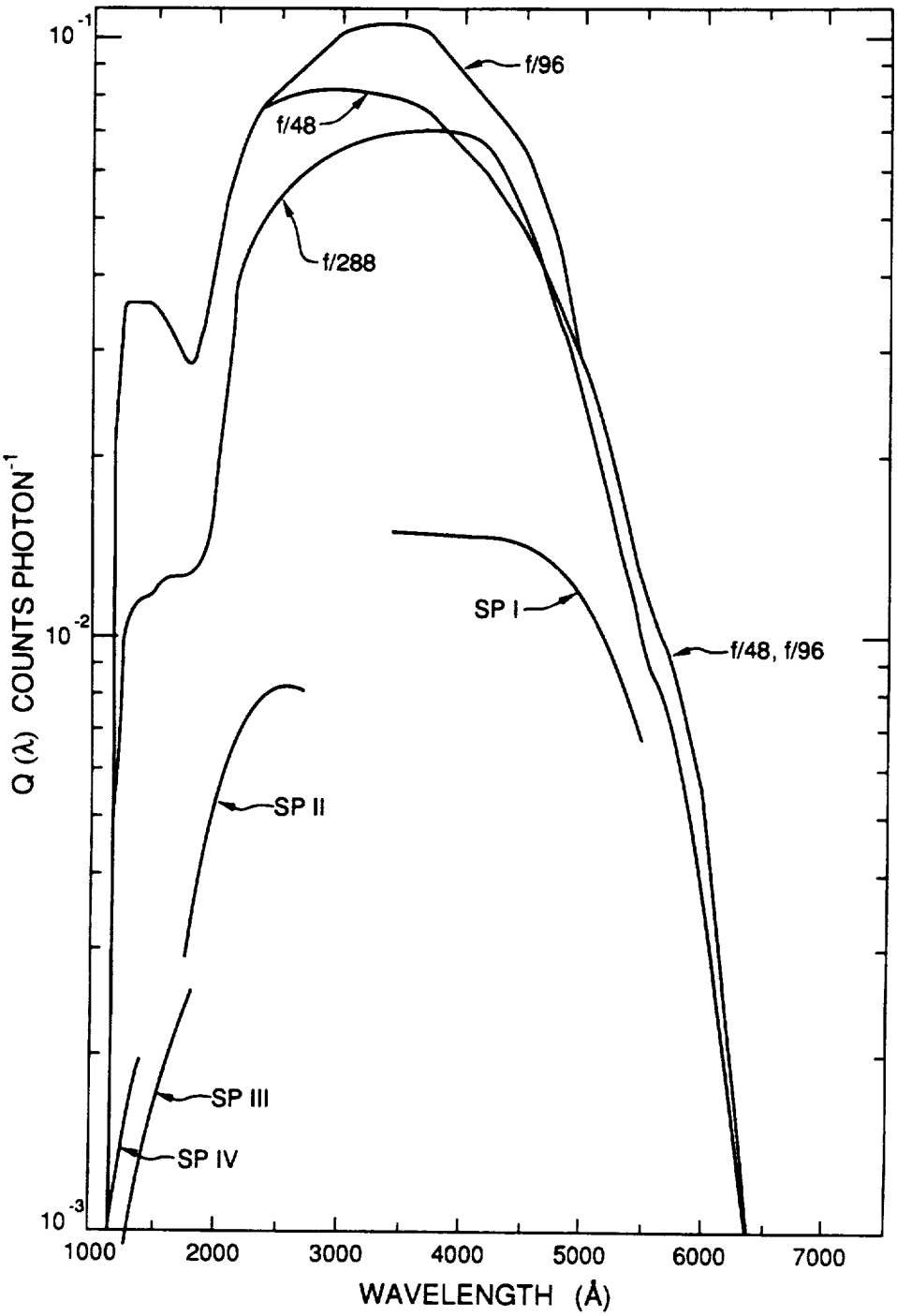

Figure 28. Baseline overall (OTA + FOC) central absolute quantum efficiency in counts photon^{-1} as a function of wavelength for the three imaging modes and the four long slit spectrograph orders.

5.5 STRAY LIGHT

Normally, the FOC background is dominated by the detector, by zodiacal light in the visible and by geocoronal Lyman alpha and diffuse galactic light in the far UV (see section 6 for detailed calculations of these components). When a bright object such as the sun, moon or the bright earth limb is nearby, however, it may be dominated by stray light reaching the OTA focal plane due to scattering from the baffle system, the OTA tube and dust on the mirror. The expected brightness of stray radiation at the OTA focal plane due to the proximity of the moon or bright earth limb in the daytime part of the orbit in V magnitudes arcsec^{-2} as a function of the angle between the moon or the limb and the OTA axis is shown in Figure 29. The two curves shown correspond to the two values of the primary mirror's dust coverage of 2% and 5% presently estimated to bracket the expected range of this parameter in orbit. The spectral shape of the stray radiation in the case of the earth can be assumed to be, for most practical purposes, that of the earth's average daylight nadir radiance given in Figure 30.

The average zodiacal light background of 120 S10 corresponding to $V \simeq 23$ magnitudes arcsec^{-2} is reached at angles greater than 80° to the limb, approximately. For viewing configurations in which the angle is less than this value, stray light will dominate in most situations. One of the most interesting of these is that encountered when observing in the continuous viewing zones (CVZ) which, in principle, allow for long uninterrupted integrations of very faint sources. Due to the altitude of the spacecraft and the depression of the horizon, the off-axis angle to the earth limb in the CVZ will be in the range $22° - 44°$, approximately. From Figure 29, the expected stray light illumination in this configuration in the visible will be between 18th and 20th magnitudes arcsec^{-2}. This means that observations in the visible will be limited mainly by this source of background. Specifically, assuming that one wishes to observe a $B = 25$ magnitude A0V star with the F/48 relay and the F430W blue filter with an accuracy of 10%, a background of this type of average brightness $V = 19$ magnitudes arcsec^{-2} in the CVZ requires an exposure time of 47 minutes or almost the entire daylit part of the orbit. At night, such an accuracy would be obtained in 11 minutes. Below 3000Å, this effect will be negligible as shown in Figure 30.

This particular example also shows that there is no advantage in exploiting the CVZ for long integrations or scheduling efficiency if the object is fainter than about 25th magnitude since the gain in signal is more than offset by the increased background. Closing the shutter during the daylight pass, in other words, is recommended in this scenario. It is, therefore, of more than passing interest to the observer to pay some attention to the maximum allowable background he can tolerate for his specific observation and to communicate this information to the ST ScI in the Phase II proposal submission.

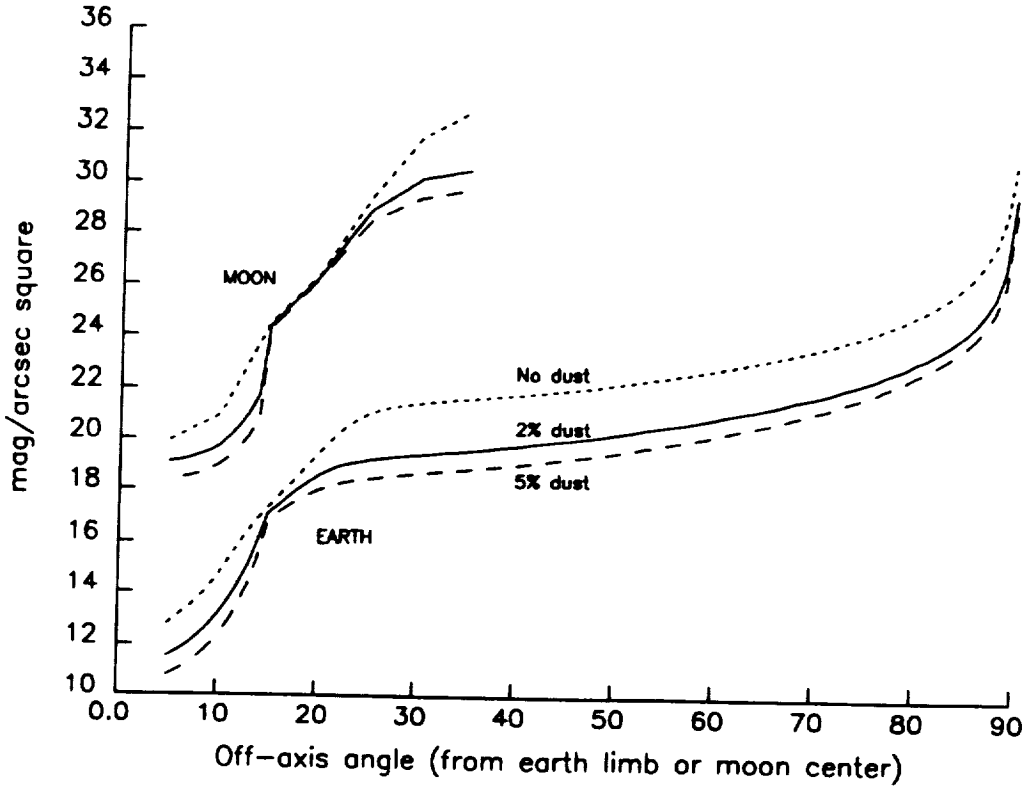

Figure 29. Stray light illumination in V magnitudes arcseconds^{-2} at the OTA focal plane due to the moon and daylit earth as a function of off-axis angle.

5.6 DETECTOR OVERLOAD

The FOC detectors described in section 3.7 may be damaged by illumination levels exceeding 10^7 photons s^{-1} pix^{-1} at the photocathode due to point sources and by an average illumination from a diffuse source over the whole photocathode exceeding 10^4 photons s^{-1} pix^{-1}. Because of this danger, the 36 kV HV power supply on the 3 stage image intensifier is set to trip off when the point source illumination exceeds the value given above or if the average illumination from a diffuse source exceeds 200 photons s^{-1} pix^{-1}. Thus, for safety reasons, no point source delivering more than 10^6 photons s^{-1} pix^{-1} at the photocathode or a diffuse source delivering more than an average rate of 100 photons s^{-1} pix^{-1} over the whole photocathode will be allowed to be imaged by the FOC. These values correspond to an 8th magnitude blue star or a diffuse source of surface brightness 11 magnitudes arcsec^{-2} viewed through the F430W filter on the F/48 relay.

5.7 OVERHEAD TIMES AND MULTIPLE EXPOSURES

Assuming that the standard science data dump operations at the 32 kHz rate apply, it will take a constant 3.7 minutes plus a variable component to transition from the absolute time tag to stop an exposure to the absolute time tag to start the next one. The variable component depends on the mode change required and can be up to another 3.4 minutes for F/96 worst case (4 filter wheels) to 1.6 minutes for F/48 worst case (2 filter wheels). Thus, it could take up to a total of 6.8 and 5.3 minutes of time between successive exposures with an average of approximately, 5 and 4 minutes for the F/96 and F/48 relays, respectively. In some specific situations, it may be advantageous, in order to save time, to take multiple exposures without closing shutter or dumping science data. Up to 11 consecutive exposures of this type can be made. If no changes to FOC Mechanisms are required, the time interval between exposures can be reduced to 16 seconds total. This is the fastest rate at which the FOC presently can be run provided the telescope can be slewed to a new position on the detector quickly enough to permit it.

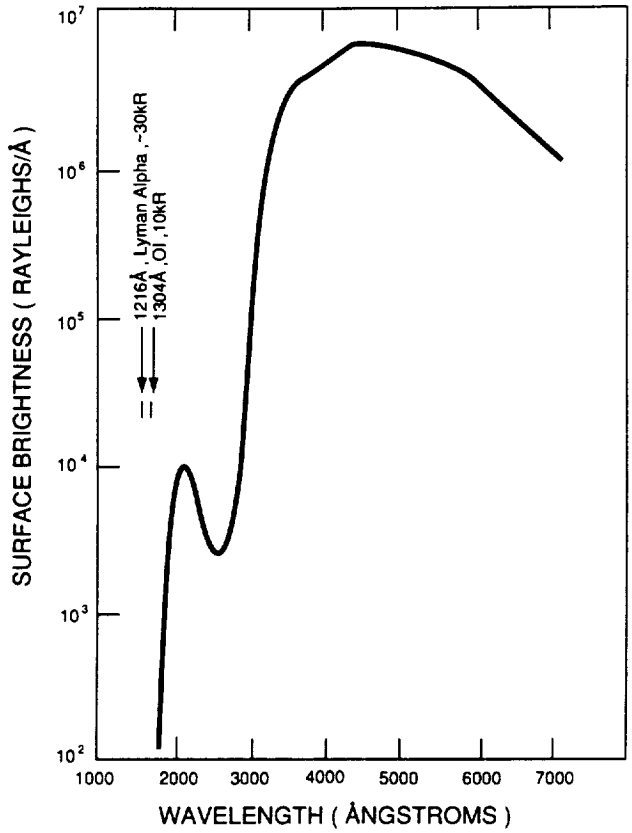

Figure 30. The earth's average daylight nadir radiance in Rayleighs $Å^{-1}$ *i.e.*, $10^6/4\pi$ photons $cm^{-2}\ s^{-1}\ Å^{-1}\ sr^{-1}$ as a function of wavelength.

5.8 GUIDING MODES WITH THE FOC

If no special requirements are placed on the guiding tolerance of the HST, (see HST Phase II Proposal Instructions), the FOC will default to coarse track (estimated RMS jitter of 0.02 arcseconds) for all F/48 IMAGE modes and to fine lock (estimated RMS jitter 0.007 arcseconds) for all other configurations. These defaults can be overriden with the guiding tolerance special requirements for situations which do not strictly require the highest possible guiding accuracies. Since this could prove quite beneficial in terms of overhead time (20 minutes for fine lock, 10 minutes for coarse track and 0 minutes for gyro hold), the user is encouraged to think carefully about his real requirements in this area. Gyro hold with an absolute position error of $\pm 60''$ arcseconds and a drift rate of 0.01 arcseconds is not expected to be used very often with the FOC but could find interesting applications for purely photometric measurements.

5.9 UNIFORMITY OF RESPONSE (FLAT FIELDING)

Extended format (512 zoom $\times$ 1024) images of a flat external source produced by a HgCdZn lamp with no filters in the beam with the F/48, F/96 and F/288 image and the F/48 Spectrograph configurations are shown in Figures A2–A5. Apart from the prominent features such as the occulting fingers in F/96 and F/288, the slit finger, and slit in the F/48 images and the reseau marks in all images, a number of other, sometimes more subtle, features are identifiable, the existence of which the user should be aware. In all images, the first 50 or so pixels from $L = 1$ to $L = 50$ in the line scan direction are corrupted by an incorrect beam scan rate due to the insufficient sharpness of the sawtooth applied voltage vs. time pattern. The faint horizontal stripes at small L values are due to a ripple instability of the coil drivers at the beginning of a frame while the narrow line running from the bottom left corner to the upper right corner is due to the read beam not being completely blanked when it is forced to flyback to $S = 0$, $L = 0$ at the end of the frame. This last feature is more noticeable with the smaller formats.

The narrow horizontal features especially noticeable at small sample numbers S occurring principally at $L = 256$, 512, 768 that can be discerned in Figure A2 are due to noise glitches on the scan coil driver caused by changes in the most significant bits of the line counter. In the large F/48 formats, the edges of the central 512 $\times$ 512 format can be discerned at the appropriate locations. This effect is due to a burn-in of that heavily used format in the camera target so that a charge discontinuity at the edges of the format has appeared. The F/96 detector has not been used enough for the effect to show up yet but it is expected to become more prominent with time. Finally, the edges of a square baffle located just in front of the detectors limit the extended F/96 and F/288 fields at the upper and lower left corners, the extended F/48 image field on the upper left corner and the extended F/48 spectrograph field at the bottom right corner.

Large and fine scale response variations across the useful area of the detectors can be identified with calibrated spatially uniform illumination either from the on-board LEDs (see section 3.3) in the visible or from external sources in the visible and UV. The large scale variations are due to a combination of distortion variations across the field of view and actual relative QE variations of the photocathode. An example of actual FOC flat field images used in RSDP pipeline processing (launch baseline version) is shown in Figures 31 and 32 for the F/48 and F/96 relays, respectively. The data refer to a wavelength of 2000Å and correspond to the extended $512z \times 1024$ field. The results are presented in the form of contour maps of the percentage deviation from unity of an image that has been smoothed to the 20×20 pixel squared level and normalized to 1 in a central 31×31 pixel squared area. Consequently, there are, approximately, 50×50 effective resolution elements in the frames shown in Figures 31 and 32. Division of the raw image taken in this format at this wavelength by these flats yields the photometrically correct frame where the large spatial scale response variations are effectively accounted for.

The general trend is for a large downward correction at low S values after the first 50 pixels decreasing slowly beyond $S \simeq 500$ for any L. The dependance of the large scale spatial response variations on wavelength is very weak in the 2000 to 6000Å region where no relative variations greater than ±10% peak to peak can be found. For the F/96 relay, in fact, the relative wavelength variations over most of the extended field are less than ±3% peak to peak as shown in Figure 33 where two smoothed flats taken at 2000 and 6000Å are divided and the percentage deviation from unity plotted as equal deviation contours–from +6% to −6% with 2% increments. Beyond 6000Å , nonuniformities become more pronounced for both relays. Reliable data below 2000Å exist only for the F/48 detector. The ratio of a 2500Å and a 1216Å flat field is shown in Figure 34 for this relay contoured at intervals the relative wavelength variations over most of the extended field are less than ±3% peak to peak as shown in Figure 33 where two smoothed flats taken at 2000 and 6000Å are divided and the percentage deviation from unity plotted as equal deviation contours—from +6% to −6% with 2% increments. Beyond 6000Å, nonuniformitites become much more pronounced of 0.05 with the usual normalization to 1 at the center. Excluding the first 50–100 pixels, variations are quite modest and well within ±10%. The data were taken when this detector was installed in the F/96 relay so that the occulting fingers are still present and should be ignored for the launch baseline. No data are available on the F/96 detector and the launch baseline will use the 2000Å flat shown in Figure 32 for the entire far UV region until the appropriate data can be gathered in orbit.

The effect of the entire response flattening process can be gauged by inspection of Figures 35 and 36 where a surface plot of a raw F/48 image at 2500Å (Figure 35) is flattened by division by the flat field shown in Figure 31 and results in the image shown in Figure 36. Count cross sections taken at $L = 200$ of the two images (uncorrected and corrected) are

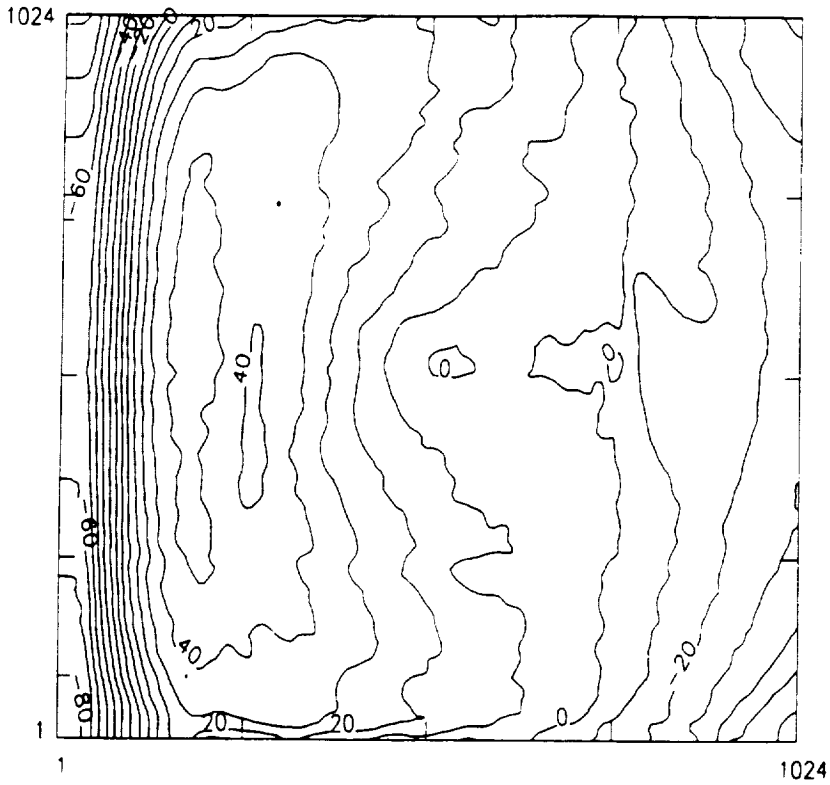

Figure 31. Percentage deviations from unity contours for an F/48 flat field at 2000Å.

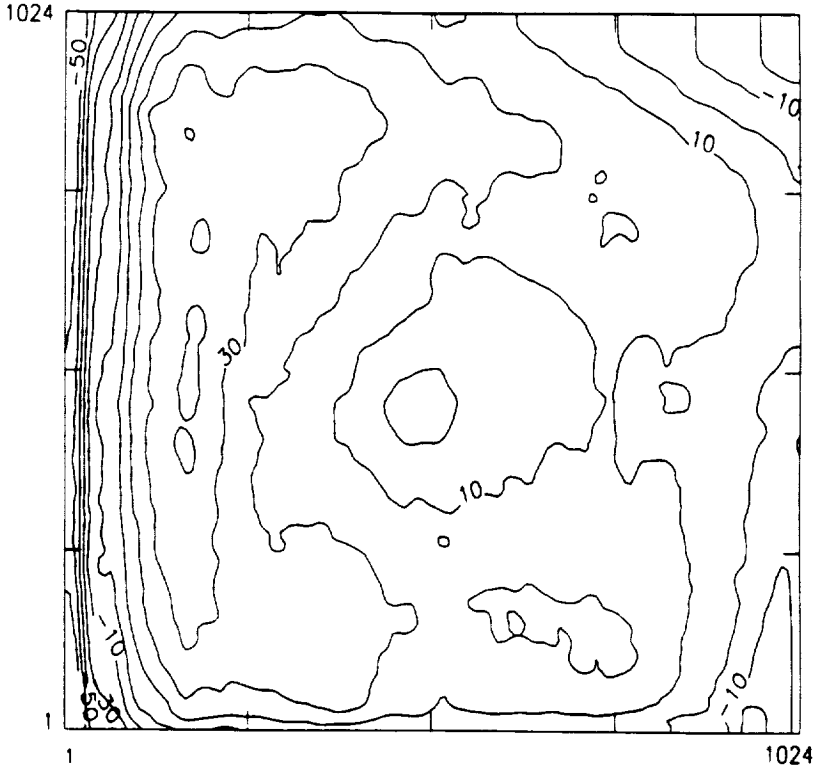

Figure 32. Percentage deviations from unity contours for an F/96 flat field at 2000Å.

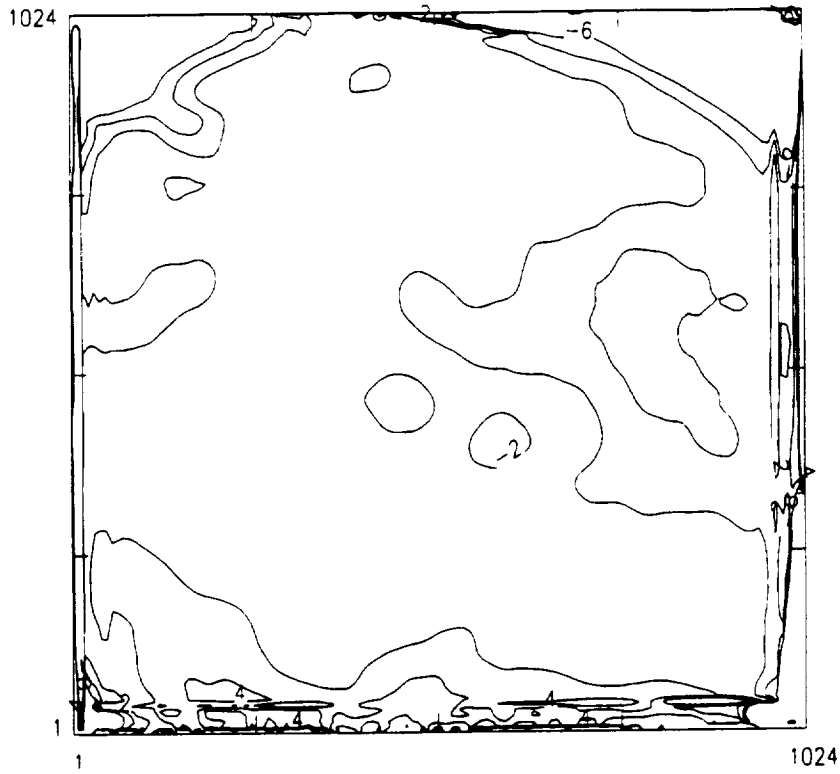

Figure 33. Percentage deviations from unity contours for the ratio of F/96 flats at 6000Å and 2000Å.

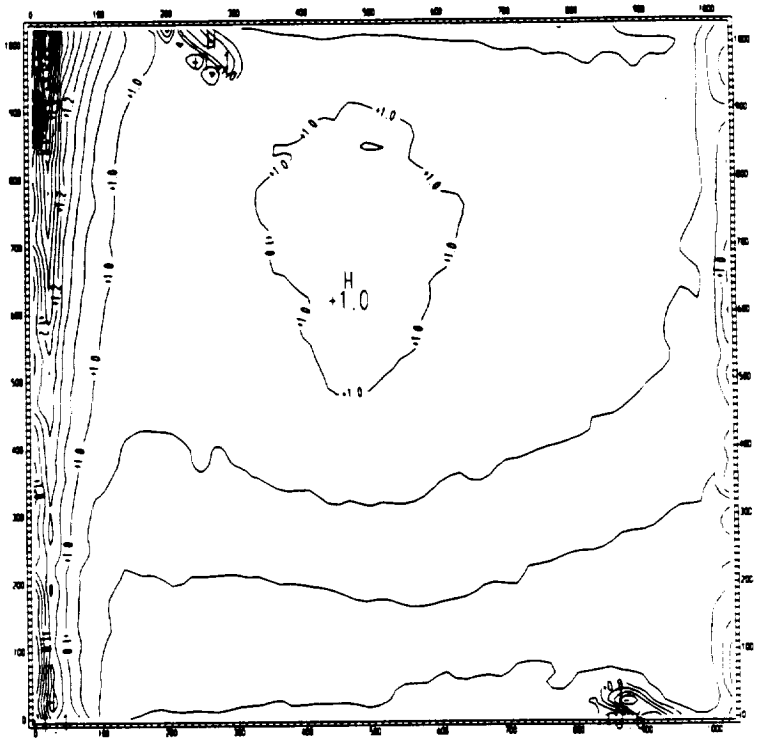

Figure 34. Ratio of F/48 flat fields at 2500Å and 1216Å contoured at intervals of 0.05.

shown in Figure 37. The procedure has left the fine scale variations intact but has properly flattened the image so that correct photometry can be executed in the next step of the calibration. The stability and reproducibility of the finer scale features are being currently investigated. These will need to be well understood, of course, if there is to be any hope for ±1% photometric accuracy. A fine scale, possibly fixed, inclined stripe pattern noise can be easily seen in bright F/96 images. It has a spatial frequency of 3 to 6 pixels and can amount to up to ±10% peak to peak variation for the F/96 detector. If this nuisance can be characterized properly, it could be corrected for in the near future. Finally, plans for a bad pixel list appended to each image and to be made available to the user are being made. This list should simplify the user's task of locating and dealing with corrupted pixels in his data.

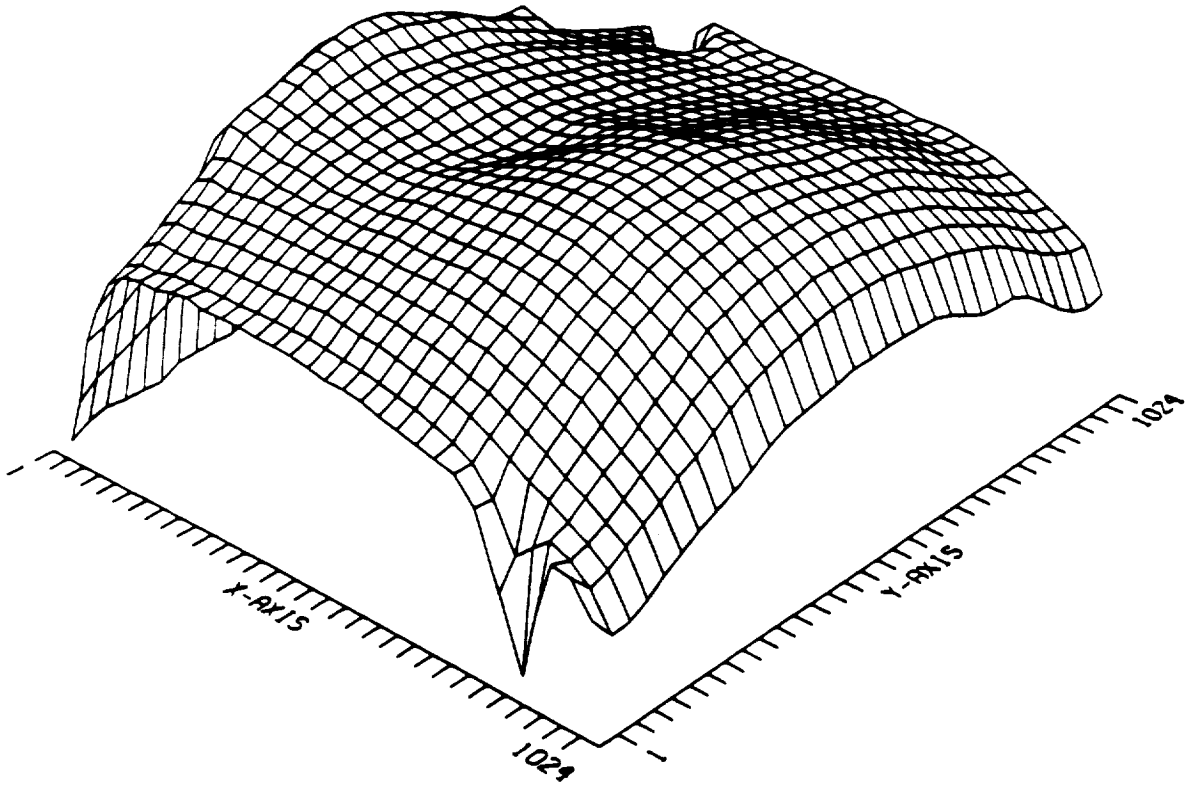

Figure 35. Three dimensional surface plot of a raw F/48 uniform illumination image at 2500Å ($z = 0$ to 130 counts).

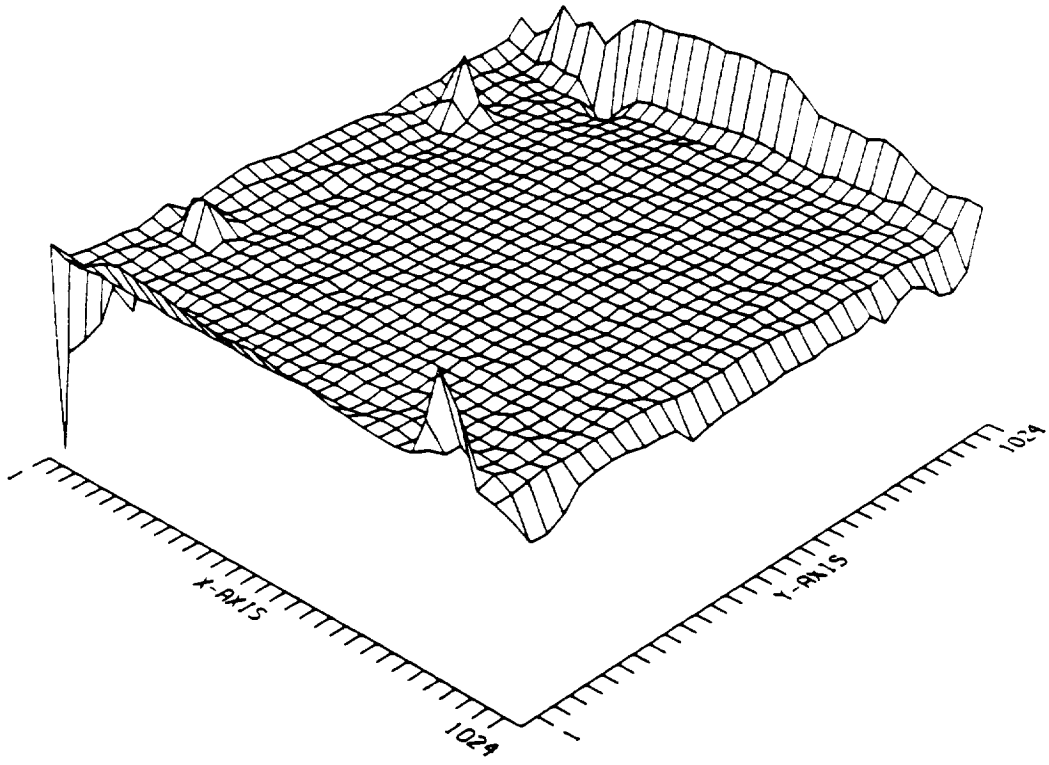

Figure 36. Three dimensional surface plot of the image shown in Figure 35 flattened by application of the flat shown in Figure 31.

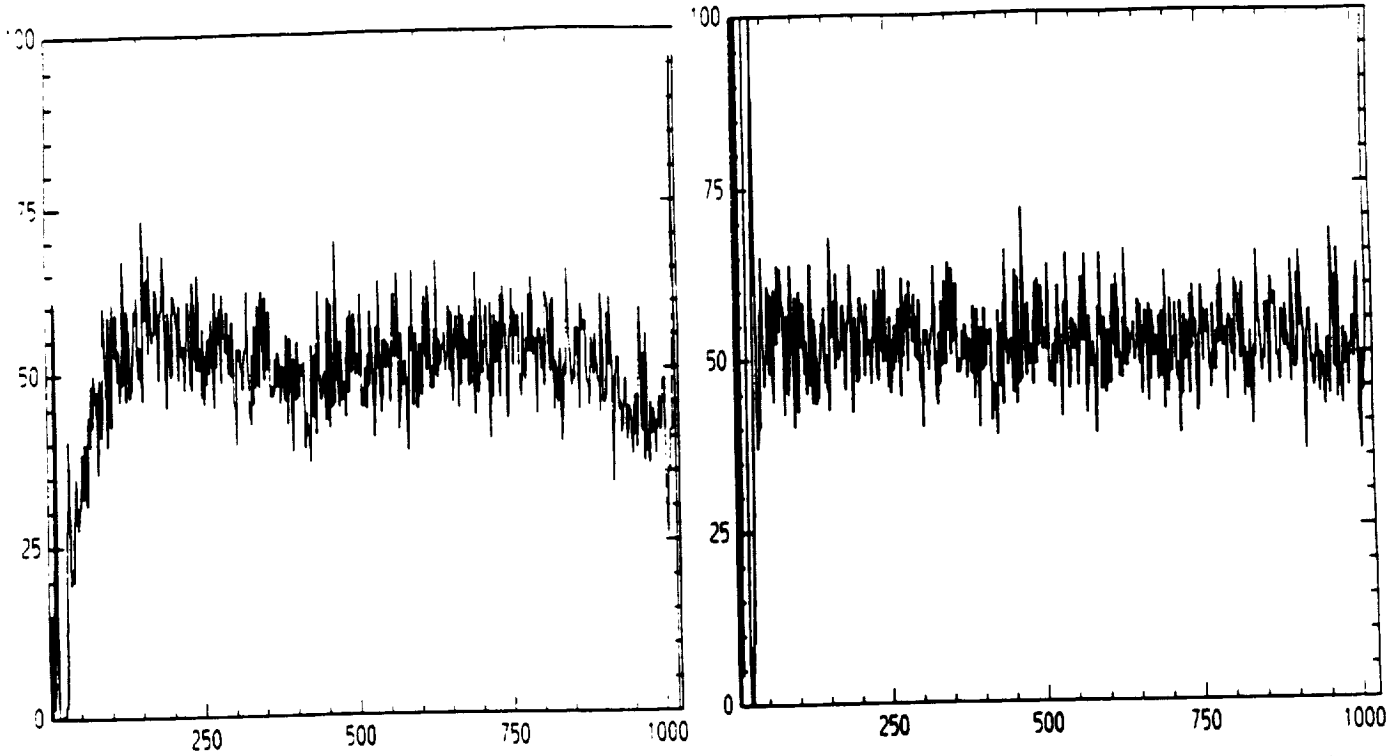

Figure 37. Count cross section at $L = 600$ of raw image shown in Figure 35 (left panel) and of flattened image shown in Figure 36 (right panel).

5.10 VISIBLE LEAKS

Although the FOC narrow and medium band filters are the very best present technology can provide, they do exhibit a residual transmission of $\simeq 10^{-3} - 10^{-4}$ between 5000 and 6000Å where the detectors are still relatively sensitive. Consequently, indiscriminate use of these filters to isolate faint UV features from a bright visible background can lead to serious errors. The magnitude of the error is, of course, very sensitive to the precise shape of the spectrum of the source to be observed throughout the sensitive range of the FOC. Thus, it is not always sufficient to know only the expected flux of the source in the range $\lambda_0 \pm \Delta\lambda/2$ in order to estimate the expected count rate.

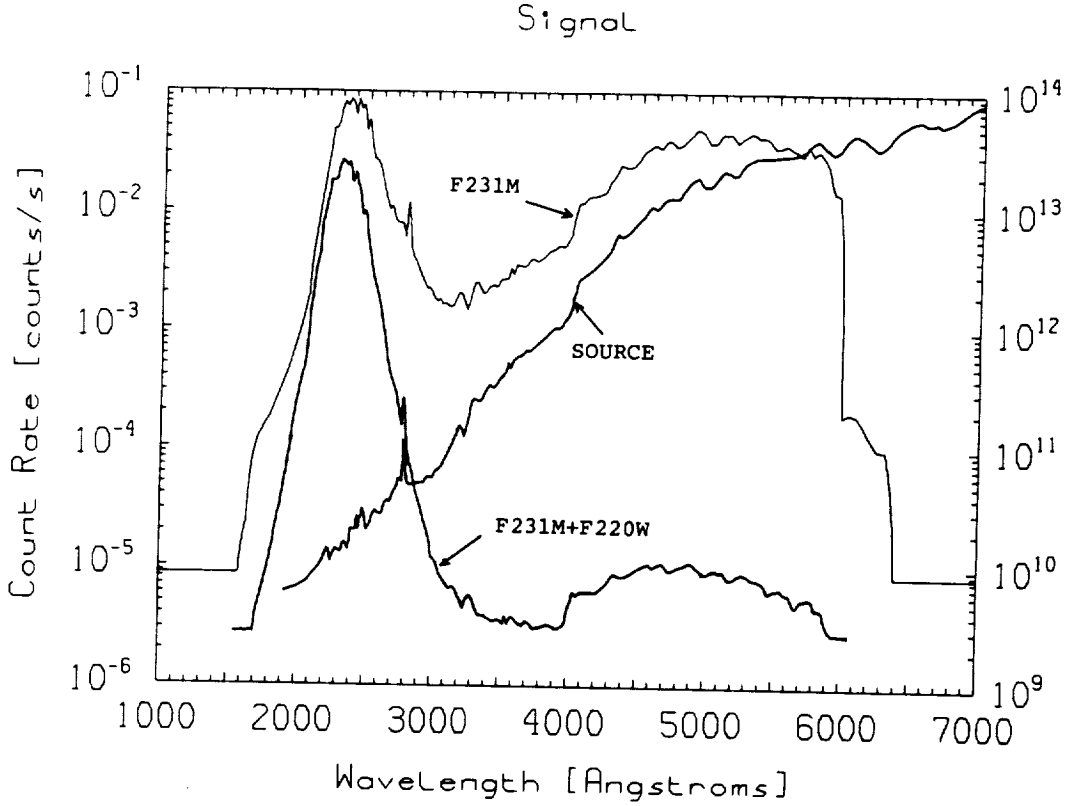

Figure 38. The expected monochromatic count rate (left ordinate scale) as a function of wavelength for the F/96 camera and the F231M filter or the F231M+F220W filters in the beam for an extended source whose spectrum varies as the curve marked SOURCE (right ordinate scale). The source flux units are photons $cm^{-2}sec^{-1}Å^{-1}sr^{-1}$.

A striking example of a possible observing scenario that can be expected when imaging a bright visible source in the UV is shown in Figure 38. In the example shown in this figure, the source spectrum marked SOURCE is assumed to increase sharply with increasing wavelength in the manner expected from an M supergiant star. If this source is fed into the F/96 camera with the F231M filter on FW#3 in the beam, the resulting monochromatic count rate as a function of wavelength through the entire OTA+FOC system is shown by the curve marked F231M. The actual observed count rate in this configuration, of course, corresponds to the integral of this curve.

If the F231M filter alone is used in this endeavour, the contribution of the flux within the band 2339 $\pm$ 120Å is only $\simeq$ 18% of the total of 94 counts sec^{-1}. The counts originating from the region $\lambda > 2580$Å represent, in contrast, 75% of the total. In this admittedly extreme case, the thus derived UV brightness would be highly suspect, to say the least. Solutions to this problem are not easy to find but, at least for the F/96 camera, one simple device would be to introduce a second cleverly selected filter into the beam in addition to the original one. This selection should be geared towards maximizing the suppression of the visible leak while minimizing absorption in the UV bandpass of interest.

In the case worked out in Figure 38, for example, the F220W filter on FW#2 is ideal as shown by the curve marked F231M+F220W. Now, the in-band fraction of counts amounts to 69% while the visible leak is only 5% or less of the total. The exposure time required to reach a S/N=10 in this case increases by a factor of six mainly because of the effective suppression of the visible counts.

Unfortunately, the F/48 camera with its much smaller filter complement has far less flexibility in this regard than the F/96 camera. In this case, another possible solution to the problem is to use the objective prisms to physically separate the UV from the visible. This technique works best for point or, at least, compact sources where spatial and spectral overlap is minimized. But even for extended sources, appropriate positioning of the target with respect to the dispersion axis of the prism can work quite well. At that point, the only remaining problem is to insure that the overload limit of the detector (described in section 5.6) is not violated for the visible part of the image.

5.11 GEOMETRIC DISTORTION

Spatial distortion of an image over the detector active area is due to two effects: the geometric distortion introduced by the OTA and FOC optics and the distortion introduced by the intensifier and camera itself. The former is difficult to measure because it is obtained as a residual distortion after the more significant detector distortion is removed and it requires very accurate measurements of external standards. This complex calibration will be performed in orbit but, in the meantime, it can be calculated theoretically by ray tracing the optics with the nominal prescription. Results of these computations indicate that the

optical distortion is such that the image scales in the S and L directions differ by about 2%. There is also a nonlinear component of distortion of about 1 or 2 pixels. The image is, thus, wider on one side than the other and both sides are displaced in the same direction relative to the middle.

The overall distortion (optical + detector) over the extended F/48 and F/96 extended fields of views is shown in Figure 39 and 40. These figures give the magnitudes and direction of the position of the distorted reseau marks with respect to the regular undistorted grid by means of vectors whose magnification is 1 (actual size). The distortion is arbitrarily assumed to be minimum at the center of the field where most users will generally want to place their targets. For the F/48 field, the distortion exceeds 1 pixel at about 40 pixels from the center, 5 pixels at about 150 pixels, 10 pixels at 350 and 20 pixels at about 500 pixels from the center. For the F/96 field, these numbers are considerably smaller *i.e.*, 1 at 25, 5 at 100, 10 at 150 and 20 pixels at 300 pixels from the center. The peak distortion for the F/96 field, however, is about 40 pixels while for the F/48 relay it is closer to 22. The F/288 distortion field is practically indistinguishable from that of the F/96 relay because the optical component is small with respect to the dominant detector part which is identical for the two relays, of course.

Due to a noticeable rotation of the format with respect to the reseau grid (see Figures A2–A5) there are areas of the extended field that are devoid of reseau marks and, for which, therefore, the geometric correction is expected to be poor. The solid lines in Figures 39 and 40 mark the boundary of the reseau grid while dashed lines indicate the edge of the camera format. Within the solid lines, the geometric correction carried out in the Routine Science Data Processing pipeline (see section 10) is expected to achieve an accuracy of order ± 0.25 pixels providing the detector is stable.

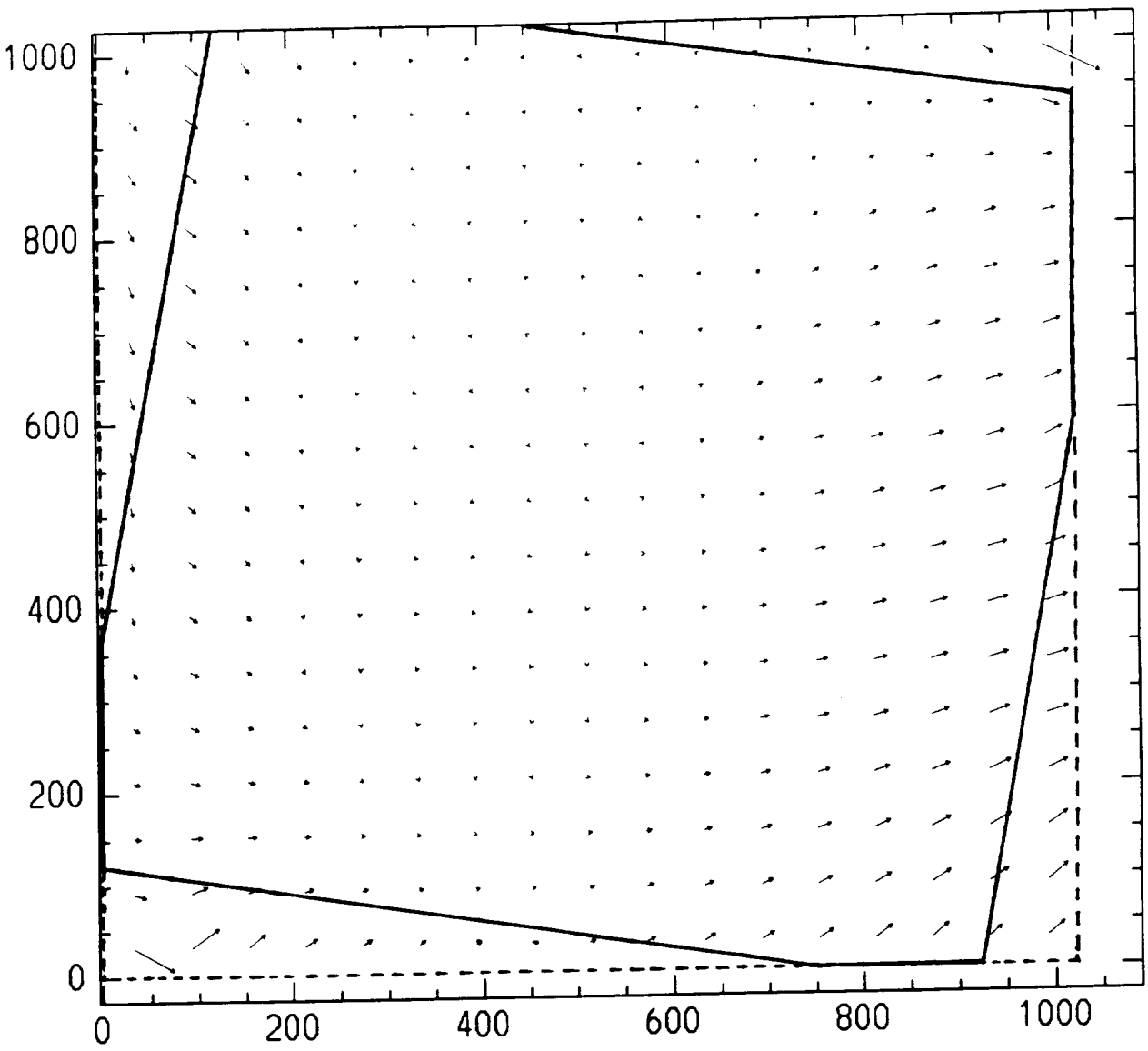

Figure 39. The overall (optical + detector) distortion field for the F/48 relay. Displacement vectors are displayed in actual size.

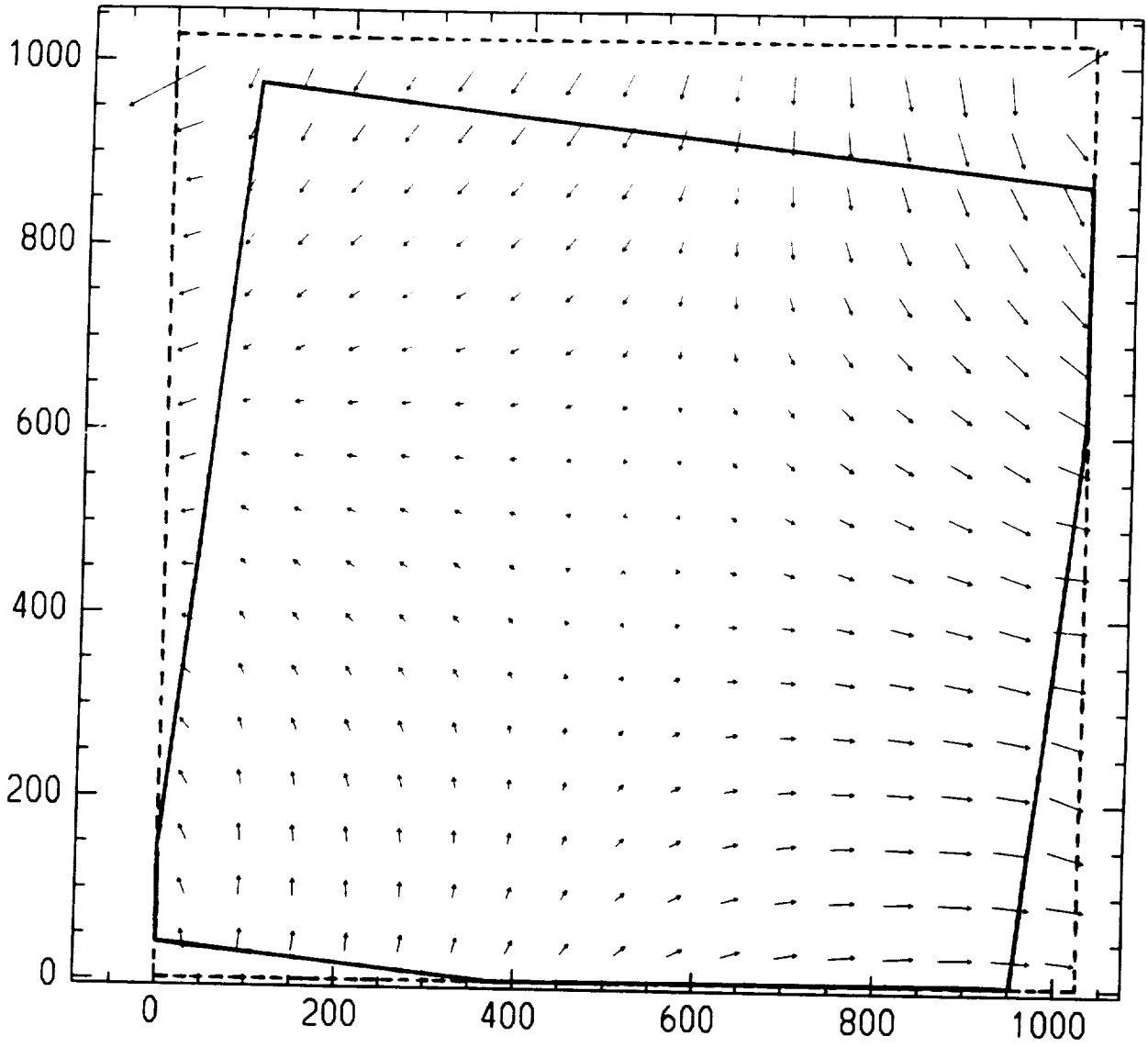

Figure 40. The overall (optical + detector) distortion field for the F/96 relay. Displacement vectors are displayed in actual size.

6.0 OBSERVER'S GUIDE (PRESCRIPTION FOR ESTIMATING EXPOSURE TIMES)

The first step consists in specifying the required signal to noise ratio S/N or the relative accuracy $\delta N/N = (S/N)^{-1}$ of the measurement. Then, the exposure time required to attain that accuracy is given, in general, for Poisson statistics, by:

$$t = (S/N)^2(R_S + 2R_B)R_S^{-2} \tag{1}$$

where R_S is the source rate and R_B the background rate in an appropriate resolution element in counts sec^{-1}. The problem then simply reduces to properly estimating R_S and R_B.

For a point source in the FOC field of view and for a count rate per pixel much less than N_{MAX} given in Table 11a, the source rate is given by:

$$R_S = \frac{\pi}{4}D^2(1-p)\int_o^\infty \epsilon(\lambda)F(\lambda)Q(\lambda)T(\lambda)d\lambda \tag{2}$$

where:

D = diameter of the ST primary = 2.4 meters
p = ratio of obscured area to total area of primary mirror = 0.138
$\epsilon(\lambda)$ = fraction of energy intercepted by the appropriate resolution element
$F(\lambda)$ = source flux at ST in photons $cm^{-2}sec^{-1}$ $Å^{-1}$
$Q(\lambda)$ = FOC+OTA response function for $T(\lambda)$ =1 in counts photon $^{-1}$
$T(\lambda)$ = transmission of filters or efficiency of dispersing elements

The terms in eq. (2) can be assumed to be appropriate averages over the pixel to pixel variations in the instrument response function. $Q(\lambda)$ and $T(\lambda)$ are plotted in Figures 27 and 10 through 14.

The background rate, on the other hand, can be expressed, in general, as:

$$R_B = nz\left[B_p + \frac{\pi}{4}D^2(1-p)\Omega^p\int_o^\infty I^B(\lambda)Q(\lambda)T(\lambda)d\lambda\right] \tag{3}$$

where:

n = number of normal (z=1) or zoomed (z=2) pixels in appropriate resolution element
B_p = inherent detector background count rate per normal pixel
$I^B(\lambda)$ = specific intensity of diffuse background at ST in photons $cm^{-2}sec^{-1}sr^{-1}$ $Å^{-1}$
Ω^p = solid angle subtended by a normal FOC pixel in steradians.

Equations (2) and (3) can be evaluated numerically or by approximating them by assuming that the spectral passband is sufficiently narrow. This permits the following simplifications:

$$R_S \simeq 3.9 \times 10^4 \epsilon(\lambda_0)F(\lambda_0)Q(\lambda_0)T(\lambda_0)\Delta\lambda \tag{4}$$

$$R_B \simeq nz\left[B_p + \frac{1.7 \times 10^{-9}}{K} I^B(\lambda_0)Q(\lambda_0)T(\lambda_0)\Delta\lambda\right] \quad (5)$$

where all the relevant functions are evaluated at wavelength λ_0 of peak response and $\Delta\lambda$ is the FWHM bandpass of the instrument in Ångstroms. The latter two parameters are listed in Table 3. K takes on the numerical values 1, 4, and 36 for the F/48, F/96 and F/288 relays, respectively.

For an extended source, the size of the resolution element nz is determined by the user according to his application. For a point source, the encircled energy tabulated in Tables 8, 9, and 10 should be used to determine $\epsilon(\lambda)$ and nz for each specific case. The precise area to be used depends in general on the S/N ratio. If it is very high, one can afford to increase the size of the resolution element nz to collect more photons, if it is low, nz should be kept as small as possible. For any particular situation, there is an optimum nz at which the S/N is maximum for a given exposure time t or at which t is minimum for a given S/N ratio. A few quick calculations should be enough to locate this condition once the background has been properly defined as indicated in the next paragraphs.

At least three sources of diffuse background have to be considered in estimating $I^B(\lambda_0)$ in eq. (5). The first is residual airglow above the ST altitude of 500-600 km. For the FOC bandpass of 1200–6000Å only two features need to be considered: the HI, Lyman α line at 1216Å and the OI, 1304Å triplet. The latter feature need only be considered for daytime observations. Their contribution to R_B can be evaluated via the graphs shown in Figure 41. In this graph, the second term in the brackets in eq. (5) is evaluated for the three FOC relays for the condition $T(\lambda_0) = 1$ as a function of spacecraft position in the orbit and for a zenith oriented line of sight. Solar zenith angle 0° corresponds to local noon, 180° local midnight. Lyman α intensities can be expected to increase approximately a factor of 40% if the line of sight drops to the horizon. R_B can be determined by multiplying the data on Figure 41 by the appropriate T(1216Å) or T(1304Å) and nz and adding to B_p.

The second source of background is diffuse galactic light (DGL). This source might be important between 1216 and 2000Å and can be estimated by means of the curves in Figure 42 which give the expected worst case background contribution of the DGL as a function of wavelength. The data shown in Figure 42 needs to be multiplied by the appropriate nz $T(\lambda_0)$ $\Delta\lambda$ to obtain R_B for this source and adding to B_p.

Finally, zodiacal light can be an important contributor to R_B in the 3000–6000Å range. This contribution as a function of wavelength is plotted in Figure 43 for the three relays. An intensity of 90 S10 units ($\simeq 3 \times 10^{-4}$ photons $cm^{-2}s^{-1}sr^{-1}Å^{-1}$) and a standard solar spectrum is assumed in these calculations. This corresponds to a line of sight direction of ecliptic latitude $\beta = 40°$ and helioecliptic longitude $\lambda - \lambda_\Theta$ =85°. Thus, R_B for the zodiacal light can be computed by multiplying the results shown in Figure 43 by the appropriate nz

$T(\lambda_0)\Delta\lambda$ and by the factor S/90 where S can be computed for any target position by means of the data tabulated by Levasseur-Regourd and Dumont (*Astr. Ap.*, **84**, 277, 1980) and reprinted here for convenience as Table 13.

How all this works in practice is best illustrated by some examples. Say that you are interested in observing an unreddened A0V star of m_B =25 with an accuracy of 10% using the F430W filter, and the F/96 camera with normal sized (unzoomed) pixels for which $z = 1$. From Table 3 for the F430W filter, you find that λ_0 =3960Å, $\Delta\lambda$ =870Å, $QT(\lambda_0)$ =0.081. The stellar flux $F(\lambda_0) = 1.2 \times 10^3 \times 10^{-0.4\times25} = 1.2 \times 10^{-7}$ photons $cm^{-2}sec^{-1}Å^{-1}$. Inserting these values into eq. (4), you get $R_S = 0.33 \times \epsilon(\lambda_0)$ counts sec^{-1}. This is the total count rate from that star spread out over a certain number of pixels corresponding to the $\epsilon(\lambda_0)$ chosen from Table 9. If the star is reddened by a given total extinction A_V, you should use a standard or average reddening curve (see Savage and Mathis, *Ann. Rev. Astr. Ap.*, **17**, 73, 1979 for an example) to deduce the appropriate $A_{\lambda 0}$. Then, R_S can be multiplied by $10^{-0.4A_{\lambda 0}}$ to take this effect into account in the simplest possible way. The possible inaccuracies introduced by this method are probably not worse than the uncertainties on the validity of the reddening curve itself and/or the prediction of the continuous flux to be observed.

Table 13. Zodiacal Light Intensities in S10 Units.

β / $\lambda - \lambda_\odot$	0°	10°	20°	30°	40°	50°	60°	70°	80°	90°
180°	180	152	127	105	89	76	66	59	58	63
170°	161	147	123	104	89	76	66	59	58	63
160°	147	134	113	98	86	75	65	59	59	63
150°	140	129	107	91	80	71	63	58	59	63
140°	139	129	105	87	75	67	62	58	60	63
130°	141	132	105	86	74	65	61	59	60	63
120°	147	138	108	88	75	66	61	59	61	63
110°	158	148	113	91	78	68	63	61	62	63
100°	175	160	120	96	82	72	65	62	62	63
90°	202	176	130	103	87	76	68	64	63	63
80°	239	197	144	113	94	82	72	67	64	63
70°	296	228	162	124	103	88	77	69	65	63
60°	394	275	190	143	116	96	82	72	66	63
50°	572	355	238	173	135	108	89	76	67	63
40°	920	510	316	220	160	123	95	80	68	63
30°	1930	825	475	285	194	140	103	84	70	63
20°				355	226	157	111	88	73	63
10°					260	167	117	90	74	63
0°					275	170	118	90	74	63

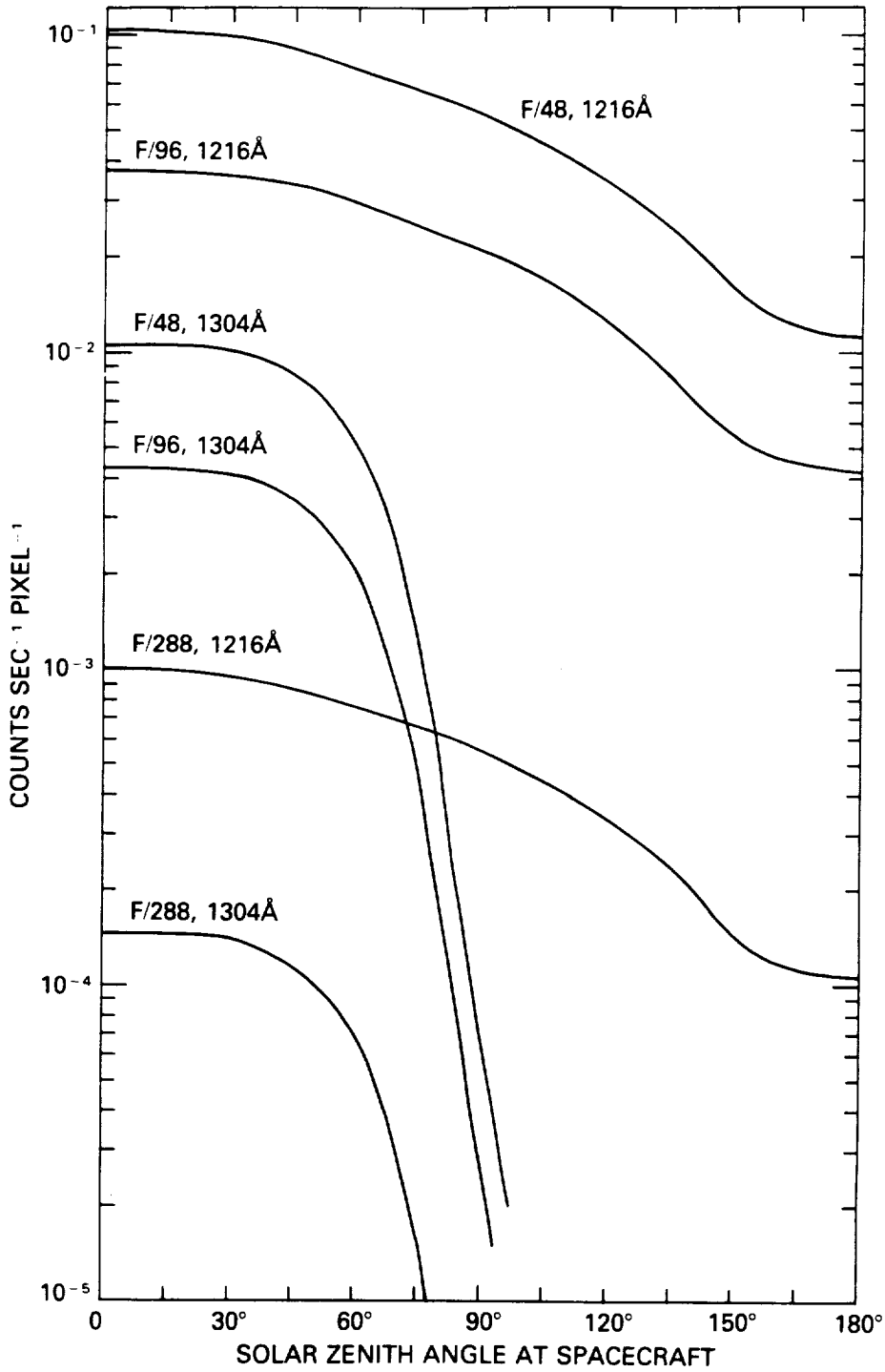

Figure 41. Residual 1216 and 1304Å airglow contribution to the FOC background counting rate with no filters in place in counts sec^{-1} per normal pixel as a function of the solar zenith angle at the spacecraft at 500km altitude. The line of sight is assumed to be oriented towards the zenith.

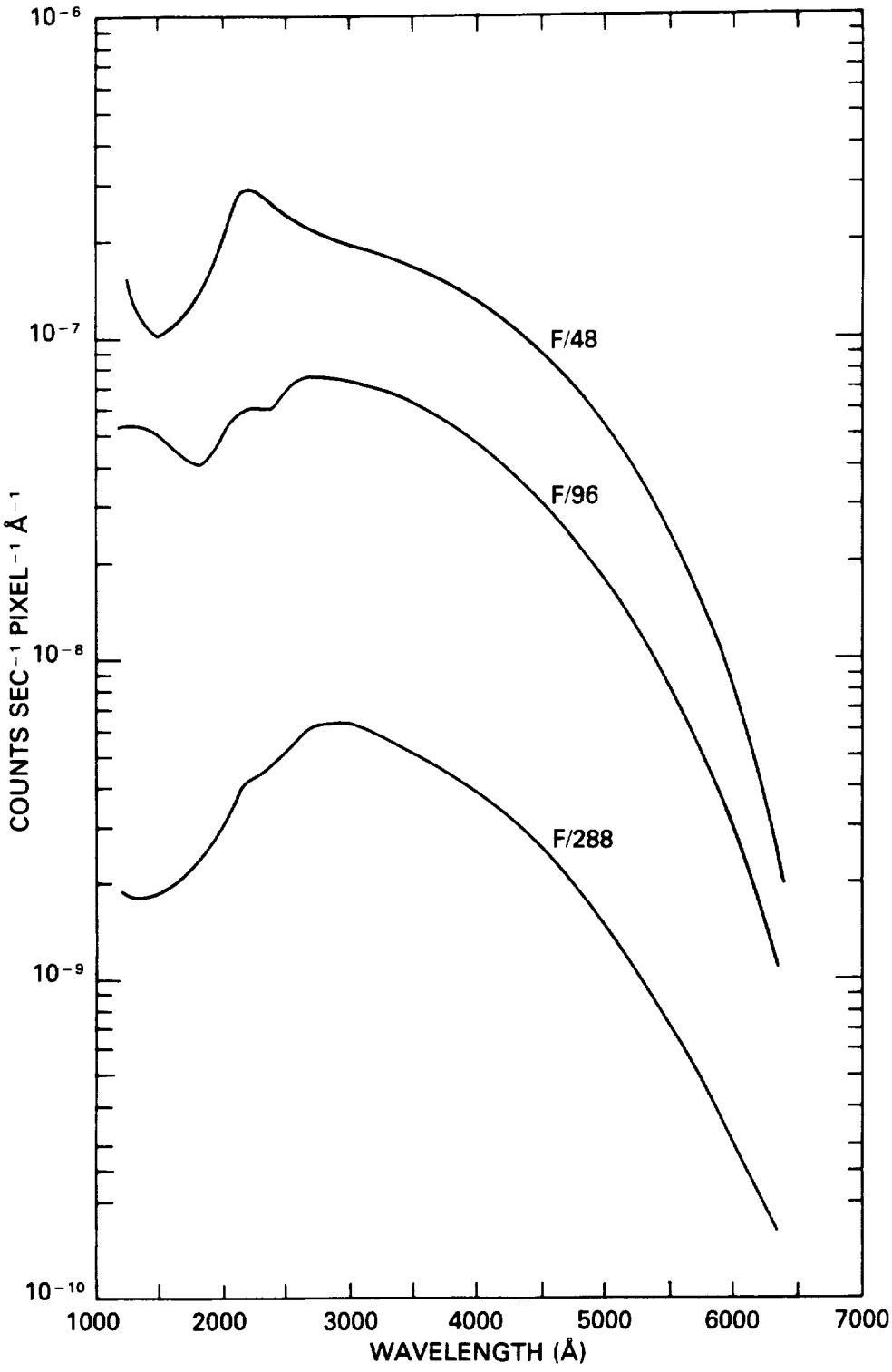

Figure 42. Maximum diffuse galactic light contribution to the FOC background counting rate with no filters in place in counts sec^{-1} Å^{-1} per normal pixel as a function of wavelength.

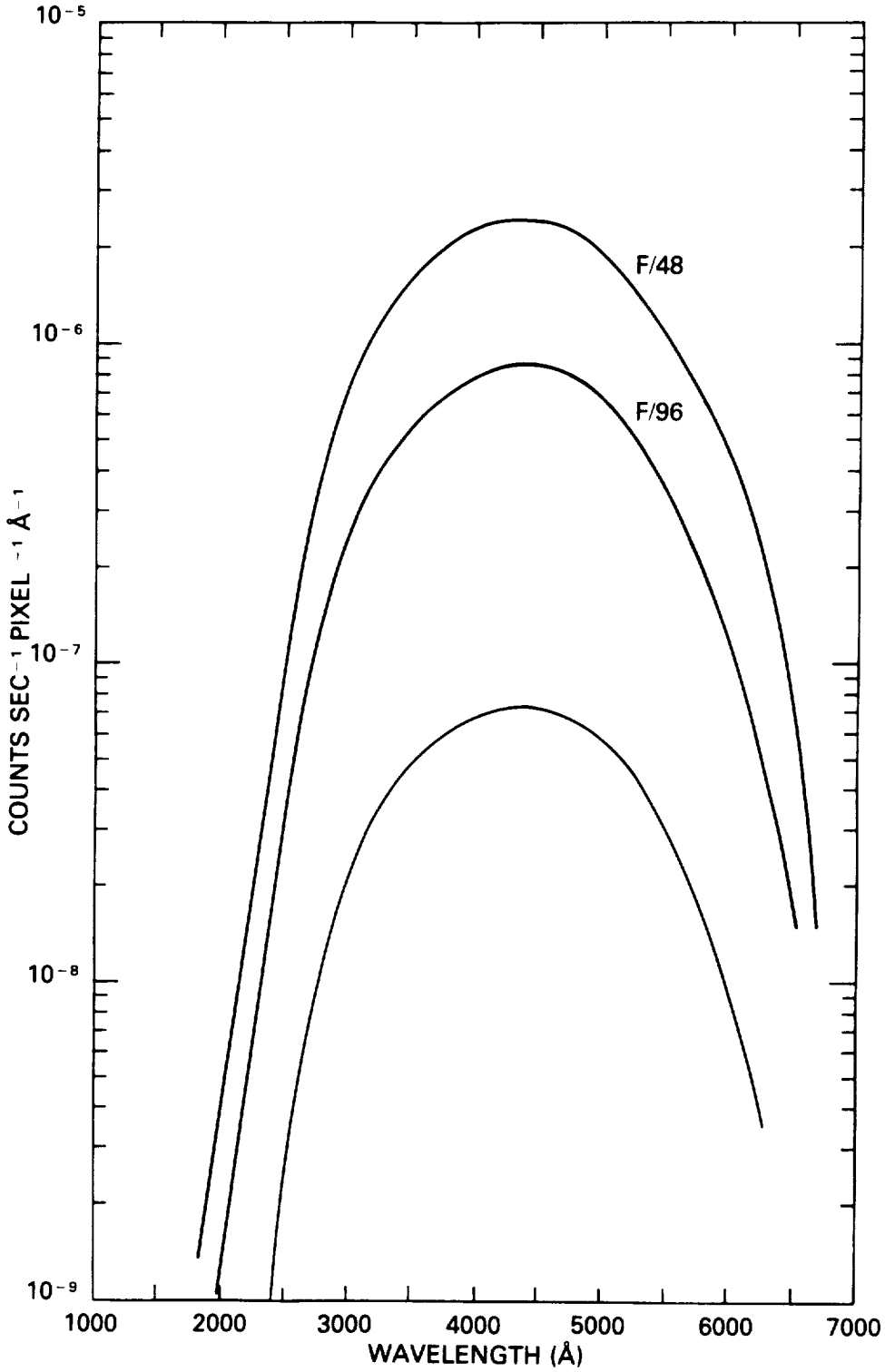

Figure 43. Zodiacal light contribution to the FOC background counting rate with no filters in place in counts sec^{-1} $Å^{-1}$ per normal pixel as a function of wavelength. The zodiacal light intensity is assumed to be 90 S10 units.

Next, calculate R_B from eq. (5) using the data in Figure 41–43. Far ultraviolet airglow is not going to be a factor in the B bandpass. The contribution of the diffuse galactic light from the data shown in Figure 42 (F/96 curve) is, at most, $4 \times 10^{-8} \times 0.74 \times 870 = 2.6 \times 10^{-5}$ counts $\text{sec}^{-1}\text{pixel}^{-1}$ where $T(\lambda_o) = 0.74$. The zodiacal light background per pixel can be estimated by means of the data graphed in Figure 43 and Table 13. Suppose the star is viewed at $\beta = 15°$ and $\lambda - \lambda_\odot = 120°$ for which S=120 S10 units. Then, this contribution is $5.8 \times 10^{-7} \times 120/90 \times 0.74 \times 870 = 5 \times 10^{-4}$ counts sec^{-1} per normal pixel so that, assuming $B_p = 5 \times 10^{-4}$ counts sec^{-1} per normal pixel, eq. (5) can be written as:

$$R_B/n \simeq 5 \times 10^{-4} + 2.6 \times 10^{-5} + 5 \times 10^{-4} = 1.03 \times 10^{-3} \text{ counts s}^{-1} \text{ pix}^{-1}$$

Then, the required exposure time can be easily computed from eq. (1) and the data in table 9 for $\epsilon(\lambda_o)$. Interpolating between the 3550Å and 4260Å data, one obtains:

n	ϵ(3960Å)	$R_S(cs^{-1})$	$R_B(cs^{-1})$	t(sec)
1	0.14	0.05	0.001	2080
9	0.49	0.16	0.009	695
25	0.62	0.20	0.026	630
49	0.73	0.24	0.050	590
81	0.76	0.25	0.083	667
121	0.79	0.26	0.125	753

Thus, integrating under the PSF out to a radius of 0.087 arcseconds at $n = 49$ provides enough flux for the required S/N to be achieved in a minimum exposure time of 590 seconds. If the background rate for some reason had been 5×10^{-3} counts s^{-1} pix^{-1} instead of 1.03×10^{-3}, the minimum exposure time would have been 977 seconds at $n = 9$.

The accuracy of this approximation is, of course, a sensitive function of the shape of the instrument bandpass and is, therefore, expected to be highest for the narrow, well-defined passband filters with negligible red and/or blue leaks. It will certainly only give rough order of magnitude estimates for the wide band pass filters for which a numerical integration of eq. (2) is required for higher confidence predictions. If there are other point sources within a few Airy radii of the primary source, their contribution to the background R_B must be evaluated by means of the appropriate system point spread function. It should also be kept in mind that some background sources may vary in intensity during an exposure. This will be the case for the airglow or scattered light emission sources for exposures lasting a good fraction of an ST orbit (see section 5.5). In this situation, it is advisable to pick the worse case intensity to evaluate the required exposure time.

Particular attention has to be paid, in any case, to the expected count rate since it may violate the assumption that $R_S n^{-1} \ll N_{\text{MAX}}$ (see Table 11a and section 5.2.2). If it does for the particular format chosen as indicated in Table 6, either the format must be changed

or a neutral density filter inserted in order to drop the expected rate below the threshold. This, of course, will also result in an increase in the exposure time required to reach the required S/N ratio.

Similar computations can be carried out for a point source in the slit of the F/48 spectrograph except that, of course, the long slit spectrograph efficiencies plotted in Figure 28 have to be used in equations (4) and (5). The bandpass $\Delta\lambda$ is now naturally limited by the projected slit width of 0.1 arcseconds corresponding to 4, 2, 1.3 and 1Å for first, second, third and fourth order, respectively. The transmission of the order sorting filter also has to be taken into account with special attention devoted to possible higher order confusion if the filter has an appreciable near uv and visible leak and the source has appreciable emission in these regions. This confusion can be eliminated completely for point or pseudo point objects with the use of the objective prism FOPCD as the cross disperser. In this case, the transmission and the dispersion of the prism given in Table 5 have to be factored into the calculations.

For the case of the objective prisms, eq. (4) can be rewritten in the form:

$$R_S(\lambda) = 3.9 \times 10^4 \varepsilon(\lambda) F(\lambda) Q(\lambda) T^{op}(\lambda) T(\lambda) \delta\lambda$$

where T^{op} is the transmission of the prism tabulated in Table 5 and $\delta\lambda$ is the wavelength interval in Å corresponding to the FOC spatial resolution. This interval can be expressed simply as:

$$\delta\lambda = 2r(\lambda) D(\lambda) PS^{-1}$$

where $D(\lambda)$ is the prism dispersion in Å mm^{-1} tabulated in Table 5, $r(\lambda)$ is the radius of the circle enclosing the required energy $\epsilon(\lambda)$ in arcseconds given in tables 8, 9, and 10 and PS is the plate scale of the appropriate relay in arcseconds mm^{-1} given on page 3. Then, the source count rate around λ is:

$$R_S(\lambda) = 7.8 \times 10^4 \epsilon(\lambda)(\lambda) D(\lambda) F(\lambda) Q(\lambda) T^{op}(\lambda) T(\lambda) PS^{-1} \qquad (7)$$

Equations (3) and (5) for the noise calculations remain the same except that some simplification can be introduced due to the fact that the overwhelming sources of background in the case $T(\lambda) = 1$ are the system integrated zodiacal light and the geocoronal Lyman α line. Thus, in this case, eq. (5) can be written as:

$$R_B = nz \left[B_p + \frac{6.7 \times 10^{-5} S}{K} + \frac{c}{b}(1.9 \times 10^{-3}) I^{kR} \right] \qquad (8)$$

where $c = 0$ for the NUVOPs and the FUVOP and FOPCD in the F/48 relay, $c = 1$ for the FUVOPs on the F/96 relay, $b = 1$ for the F/48 camera, and $b = 2$ for the F/96 camera. S

is the intensity of the zodiacal light in S10 units and I^{kR} is the intensity of the Lyman α airglow in kilorayleighs.

To see how this works, suppose you want to observe a 20th visual magnitude QSO with a ν^{-2} spectrum and you want to compute the required exposure time to obtain a S/N=10 at 1700Å with the F/96 FUVOP. In this case, F(1700Å)=10^{-5} photons $cm^{-2}s^{-1}Å^{-1}$. From the data tabulated in Table 8, you find r(1700Å)=0.174 arcseconds for ϵ(1700Å) = 0.6 and, from the data in Table 5, D(1700Å) = $13.2/24 \times 10^{-3}$ = 550Å mm^{-1} and T^{op}(1700Å) = 0.88 while Q(1700Å)=0.031 from Table 12. This means that the source rate from eq. (7) at 1700Å is 1.37 counts sec^{-1}. The count rate is spread over $n = 49$ pixels for $z = 1$ from Table (8). Assuming that S = 120 S10 for the zodiacal light, $I^{kR} = 5$ kilorayleighs, $B_p = 5 \times 10^{-4}$ counts sec^{-1} $pixel^{-1}$, and K=4, c=1, b=2, eq. (8) gives:

$$R_B = 49\left[5 \times 10^{-4} + \frac{6.7 \times 10^{-5} \times 120}{4} + \frac{1.9 \times 10^{-3} \times 5}{2}\right] =$$

$$49\left(5 \times 10^{-4} + 2 \times 10^{-3} + 4.8 \times 10^{-3}\right) = 0.36 \text{ counts sec}^{-1}$$

Finally, the required exposure time is:

$$t = \frac{100(1.37 + 2 \times 0.36)}{1.37^2} = 111 \text{ seconds.}$$

The prescription for an extended source deviates only slightly from the formulation discussed so far provided R_S is redefined as:

$$R_S = nz\frac{\pi}{4}D^2(1-p)\Omega^p \int_o^\infty I_S(\lambda)Q(\lambda)T(\lambda)d\lambda \qquad (9)$$

$$= nz\frac{1.7 \cdot 10^{-9}}{K} \int_o^\infty I_S(\lambda)Q(\lambda)T(\lambda)d\lambda$$

where n is now the chosen number of normal ($z = 1$) or zoomed ($z = 2$) pixels in the required resolution element and $I_S(\lambda)$ is the specific intensity of the extended source in photons $cm^{-2}sec^{-1}sr^{-1}$ $Å^{-1}$. Equations (3) and (5) for R_B need not be modified. Conversion of other specific intensity units into photons $cm^{-2}sec^{-1}sr^{-1}$ $Å^{-1}$ can be executed via the following relations:

Units	Photons cm^{-2} sec^{-1} sr^{-1} $Å^{-1}$
U magnitudes per arcseconds squared	$=3.2\times10^{13} \times 10^{-0.4U}$ at 3600Å
B magnitudes per arcseconds squared	$= 6.4\times10^{13} \times 10^{-0.4B}$ at 4470Å
V magnitudes per arcseconds squared	$= 4.3\times10^{13} \times 10^{-0.4V}$ at 5560Å
1 Rayleigh $Å^{-1}$	$= 8.1\times10^{4}$
1 erg $cm^{-2}s^{-1}sr^{-1}$ $Å^{-1}$	$= 5 \times10^{7}\lambda$ (Å)
1 $Wm^{-2}Hz^{-1}sr^{-1}$	$=1.5\times10^{29}[\lambda(Å)]^{-1}$
1 S10	=333

Suppose, for example, you want to observe a Lyman α aurora above the limb of Jupiter of intensity 20 kiloRayleighs with a spatial resolution of 0.22 arcseconds with a S/N = 10 with the F/96 camera. You will be using 100 F/96 pixels for this purpose. You should use the F120M filter because it has the highest transmission at Lyman α and the lowest transmission at the longer wavelengths where the disk Rayleigh scattering spectrum may overwhelm any far uv auroral features.

From Figure 12, you find that at λ =1216Å, the F120M filter has T=0.1 and from the graph in Figure 28 you deduce that Q(1216Å)=0.025. Then, since in this case the Jovian emission line of width $\leq$1Å is much narrower than the instrumental bandpass of 86Å, eq. (9) can be written simply as:

$$R_S \simeq \frac{100 \times 1.7 \times 10^{-9}}{4} \times 2 \times 10^4 \times 8.1 \times 10^4 \times 0.025 \times 0.1 \ = 0.17$$

counts sec^{-1}per resolution element

The background rate R_B will be dominated by the detector background and the geocoronal Lyman α airglow if the observation is carried out at night. The DGL contribution is negligible in all cases ($\leq 4.3 \times 10^{-5}$ counts sec^{-1} per resolution element.) From the curve marked F/96, 1216Å in Figure 41 for a typical observing configuration of 150° local solar zenith angle, you obtain 5.4×10^{-3} counts sec^{-1} $pixel^{-1}$ looking towards the zenith. This implies that, for $B_p = 3 \times 10^{-4}$ counts sec^{-1} $pixel^{-1}$, you have:

$$R_B = 100\left[3 \times 10^{-4} + 5.4 \times 10^{-3} \times 0.1\right] = 0.08$$

counts sec^{-1}per resolution element

This means that S/N=10 for this Jovian aurora and resolution can be reached in:

$$t = \frac{100(0.17 + 2 \times 0.08)}{0.17^2} = 1170 \text{ seconds}$$

Observations at higher spatial resolution would require correspondingly longer exposure times.

If this same aurora is to be observed against a planetary disk background of Lyman α emission of 15 kilorayleighs with the same accuracy, the relevant background rate becomes:

$$R_B = 100 \left[3 \times 10^{-4} + 5.4 \times 10^{-4} + \frac{1.7 \times 10^{-9}}{4} 15 \times 2 \times 10^4 \times 8.1 \times 10^4 \times 0.025 \times 0.1\right]$$

$$= 100 \left[3 \times 10^{-4} + 5.4 \times 10^{-4} + 1.3 \times 10^{-2}\right] = 0.34 \text{ counts sec}^{-1} \text{per res. el.}$$

so that:

$$t = \frac{100(0.17 + 2 \times 0.34)}{0.17^2} = 2956 \text{ seconds}$$

In this case, however, you might be looking onto the visible disk of the planet and the visible leak will dominate the count rate. To estimate the visible leak contribution notice that at $\simeq$5000Å, the F120M filter has a residual transmission of 10^{-4} and assume the Jovian spectrum to be solar with an intensity of $\simeq 2 \times 10^6$ Rayleighs Å^{-1} at 5000Å. Thus, you can approximate the effect by spreading this intensity over $\simeq$1500Å where Q(λ) $\simeq$0.03. Then, with these assumptions:

$$R_B \simeq 0.34 + 100 \left[\frac{1.7 \times 10^{-9}}{4} 2 \times 10^6 \times 8.1 \times 10^4 \times 0.03 \times 10^{-4} \times 1500\right]$$

$$\simeq 0.34 + 31 \text{ counts sec}^{-1} \text{per resolution element.}$$

A solution to this problem would be to insert another filter into the beam to suppress the visible contamination. A good choice would be F140W for which T(1216Å) = 0.05 and

T(5000Å)= 3×10^{-4} and:

$$R_S = 0.17 \times 0.05 = 8.5 \times 10^{-3} \text{count sec}^{-1} \text{per resolution element}$$

$$R_B = 0.34 \times 0.05 + 100 \left[\frac{1.7 \times 10^{-9}}{4} \times 2 \times 10^6 \times 8.1 \times 10^4 \times 0.03 \times 10^{-4} \times 3 \times 10^{-4} \times 1500 \right]$$

$$= 0.017 + 0.009 = 0.026 \text{ counts sec}^{-1} \text{per resolution element}$$

$$t = \frac{100(8.5 \times 10^{-3} + 2 \times 0.026)}{(8.5 \times 10^{-3})^2} = 8.37 \times 10^4 \text{seconds} = 23.3 \text{ hours}$$

Obviously, this hypothetical program cannot be accomplished with the FOC. To reduce the exposure time to physically realistic levels one needs to, say, reduce the required accuracy and/or spatial resolution. For example, halving both the accuracy and the resolution to 20% and 0.44 arcseconds respectively in this case, yields a more acceptable exposure time of 2.9 hours.

Finally, suppose you wish to image an extended object (a planetary nebula, for example) with the F/96 camera at the highest possible resolution in the zoomed configuration for the biggest possible field of view. Suppose the object exhibits a line spectrum with a surface brightness at Hβ of 5×10^{-13} ergs cm^{-2} s^{-1} arcsec^{-2} and you wish to use the F486N interference filter to isolate the line to an accuracy of 10%. From the data shown in Figures 11 and 28 you find that at 4861Å, $T = 0.6$, and $Q = 0.04$. From the conversion relations on page 85, you note that $I_s(4861) = 5 \times 10^{-13} \times 4.25 \times 10^{10} \times 5 \times 10^7 \times 4861 = 5.16 \times 10^9$ photonscm^{-2} s^{-1} sr^{-1}. Thus, eq. (9) becomes for $n = 1$, $z = 2$:

$$R_S = \frac{2 \times 1.7 \times 10^{-9}}{4} \times 5.16 \times 10^9 \times 0.6 \times 0.04 = 0.105 \text{ counts s}^{-1} \text{ per zoomed pixel}$$

From the data shown in Figure 43 and a zodiacal light brightness of 90 S10 and $B_p = 3 \times 10^{-4}$ counts s^{-1} per normal pixel, eq. (5) becomes:

$$R_B = 2[3 \times 10^{-4} + 7.3 \times 10^{-7} \times 0.63 \times 34] = 6.3 \times 10^{-4} \text{ counts s}^{-1} \text{ per zoomed pixel}$$

because $T(\lambda_o) = 0.63$ and $\Delta\lambda = 34$Å for the F486N filter from the data in Table 3. In consequence, finally:

$$t = \frac{100(0.105 + 2 \times 6.3 \times 10^{-4})}{0.105^2} = 964 \text{ seconds.}$$

7.0 THE FOC EXPOSURE TIME SIMULATOR, FOCSIM

Although the general procedures to compute the required exposure times for any FOC observing configuration and possible emission source outlined in the preceding section are perfectly adequate for most purposes including proposal preparation and feasibility verification, there are cases where it is useful to have available means of evaluating more precisely the integrals in eqs. (2), (3) and (9). This capability is especially important when the emission source spectrum is not well behaved outside the wavelength range of interest (see, for example, the situations described in sections 5.7 and 6 concerning visible leaks), when the precise spatial distribution of counts in the image is important as in crowded fields and for more precise planning envisaged in Phase II of proposal preparation. For these and other possibly more complex situations, an exposure time simulator for the FOC has been developed by the author and Y. Frankel of ST ScI. This program, called FOCSIM, presently evaluates exactly the exposure times and S/N ratio for any imaging exposure. It also allows computation of the actual expected spatial patterns of the FOC images and, therefore, evaluation of the correct S/N for wide bandpasses and/or crowded fields.

FOCSIM, as presently configured, is a menu driven interactive FORTRAN program which accepts user input describing the FOC observing configuration and the physical characteristics of an astronomical source to be observed and computes count rates, background levels and exposure times consistent with those inputs. The user may select from a number of synthetic spectra the radiation sources for the program or use his own file of wavelengths and fluxes in appropriate units. The sources resident in the program include 77 simulated stellar spectra covering a wide range of MK classes generated by the Kurucz (1979) stellar atmosphere models, a number of UV standard stellar spectra from IUE (*Ap. J. Suppl.*, **40**, 1, 1979), a flat continuum between two wavelengths, up to three emission lines, a blackbody source of arbitrary temperature and a power low spectrum of arbitrary index. The normalization factors of flux and wavelength can all be specified arbitrarily by the user. Any of these sources can be made artificially extended by an appropriate change in scale and normalization factors, if so desired.

The diffuse background can also be calculated precisely by FOCSIM. Presently, user supplied intensities of zodiacal light, for UV airglow, diffuse galactic light and inherent detector background can be accommodated and work is advanced on a subroutine to compute the zodiacal, far UV airglow and scattered light from sunlit earth, moon and sun components for any target position and HST observing configuration. This feature is expected to be available for Phase II planning and scheduling.

The output of FOCSIM includes all relevant information on the input parameters selected, the appropriate instrumental parameters and subsidiary data such as the individual components of background, the monochromatic count rate shown in Figure 38, restrictions such as N_{MAX}, data on the magnitude of the red and blue leaks, and, of course, the resultant

exposure times for the required accuracy. An NCAR graphics package also allows the user to plot the important functions on his graphics terminal. FOCSIM will be made available at the ST ScI to any interested and qualified users of the FOC. Please consult the FOC Simulator User Reference Manual available from the ST ScI for further details.

8.0 LIMITING MAGNITUDES

FOCSIM can be used to predict the limiting magnitude of any observing configuration. An example of this type of calculation is shown in Figures 44 and 45 for worst and best case observing scenarios expected to comfortably bracket the actual in-flight conditions. The former is defined by a zodiacal light intensity of S10 = 180 units and a detector background $B_p = 10^{-3}$ counts sec^{-1} $pixel^{-1}$ while, for the latter, these parameters are taken to be S10 = 60 units and $B_p = 10^{-4}$ counts sec^{-1} $pixel^{-1}$.

The predicted exposure time in seconds needed to reach a S/N = 10 for a specified visual magnitude of a B5V star through the F342W (U) filter for the two cameras is plotted in Figure 44. In the best observing conditions, we should expect to detect a B5V star of $m_V = 29$ with 10% accuracy with the U filter in about 10 hours of exposure. The limiting magnitude is $m_V = 30$ if a S/N = 5 is deemed sufficient. Similar calculations performed for extended sources are shown in Figure 45. For this case, the specific intensity of the source is expressed in terms of visual magnitudes per arcseconds squared and the spectrum is assumed to have the shape of a B5V star. The spatial resolution is taken to be 0.1 arcseconds corresponding to a little over 2 and 4 F/48 or F/96 pixels, respectively. One should be able to detect a source of intensity $\simeq$ 25 visual magnitudes per arcseconds squared at S/N = 10 and 0.1 arcsecond resolution in 10 hours of exposure with the U filter under the best observing conditions.

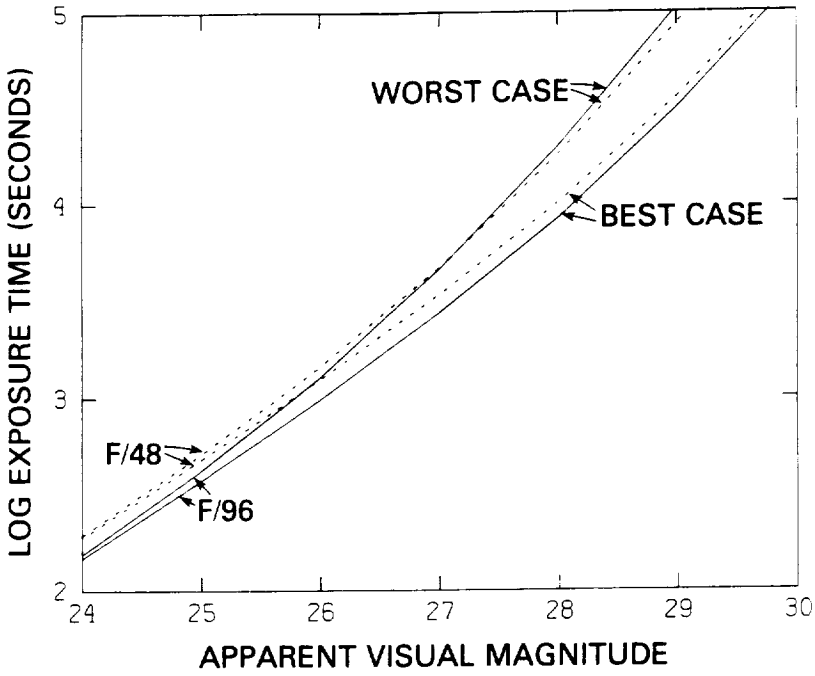

Figure 44. Exposure time required to reach a S/N = 10 on a B5V star with the U filter in two extreme observing conditions. Upper curves: $B_p = 10^{-3}$ counts sec^{-1} $pixel^{-1}$ and a zodiacal light intensity of 180 S10. Lower curves: $B_p = 10^{-4}$ counts sec^{-1} $pixel^{-1}$ and a zodiacal light intensity of 60 S10.

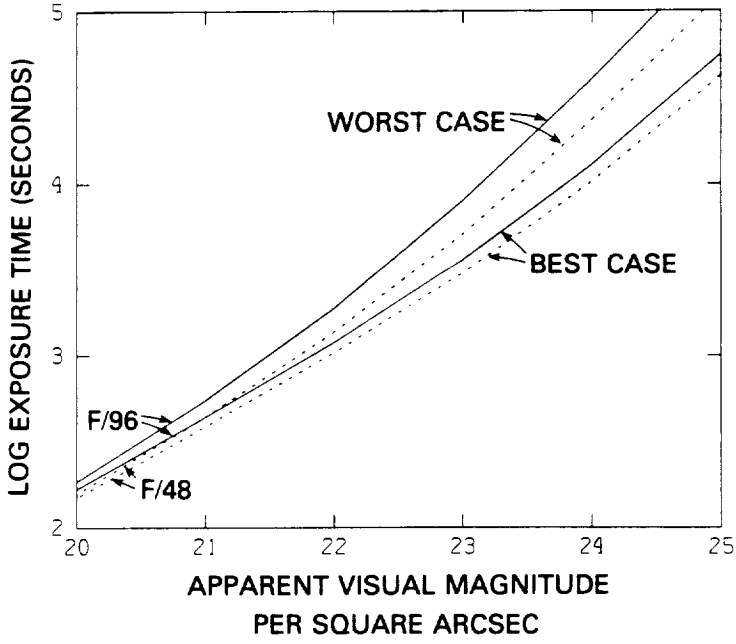

Figure 45. Exposure time required to reach a S/N = 10 on a B5V spectrum extended source with 0.1 arcsecond resolution with the U filter in the two extreme observing conditions listed in Figure 34.

9.0 FOC DATA ANALYSIS AND PRODUCTS

9.1 PIPELINE PROCESSING

All data taken by the FOC are automatically processed and calibrated by the Routine Science Data Processing (RSDP), also called the "pipeline". It is possible to repeat, off line, the calibration part of the pipeline processing by using an IRAF/STSDAS task called CALFOC (CALibration of FOC data), used automatically by the pipeline. For every observation, the user will receive two sets of data coming out of the pipeline: the input and output files to CALFOC. The input files to CALFOC are:

1) the raw image,
2) a mask image characterising the location of known bad pixels, reseaux, and likely data errors determined by online processing of transmitted data called the Data Quality File,
3) a file containing astronomical information related to the observation called the Standard Header Packet, and
4) a file containing engineering data related to the observation called the Unique Data Log.

The output files from CALFOC are:

1) the photometrically corrected image,
2) the geometrically corrected image, and
3) the reseau location file used for the geometric correction.

The data processing flow charts for normal imaging and spectrographic images are shown in Figures 46 and 47. CALFOC assumes that the processing parameters are in the image header, either directly from RSDP preprocessing, or inserted by task "cloadrsdpx" or "loadrsdpx". The processing parameters govern which correction steps are to be performed, and which calibration files are to be used. For normal imaging observations, the following steps are performed in order:

- dark count subtraction
- format dependent photometric correction (using ITF reference file)
- unzoom the zoomed image
- relative calibration or flat field correction (removing instrumental sensitivity variations) using UNI reference files, which are reciprocal of flat fields
- absolute calibration affecting header parameters only
- geometric distortion correction involving data interpolation and requiring a new mask image.

For spectrographic (long-slit) observations, the first three steps are the same as for imaging observations. But after dezooming, the following steps are performed in order:

- geometric distortion correction involving data interpolation

- spectrographic relative and absolute calibrations with flux and wavelength calibrations affecting both data and headers

In the spectrographic mode, several orders may overlap. The pipeline delivers separately calibrated data sets for each order, leaving line identification and order deconvolution to the user. The pipeline delivers the raw image and data sets corresponding to the results of the tasks as indicated in Figures 46 and 47. Detailed information on FOC calibration procedures and algorithms can be found in the "Requirements Section" of the "Design Manual, DRD-SOGS-SE-06-1," available from STScI. Some more general information is contained in the Calibration HST Data Set manual.

9.2 GENERAL PROCEDURES

All delivered images are REAL*4 datatype, to avoid integer rounding. The actual counts in each pixel are preserved as accurately as possible to permit immediate visualization of counting statistics and noise.

9.2.1 Dark-Count Subtraction

The dark-count reference file multiplied by the exposure time is subtracted from the input science file. The dark-count file is a full-frame image (512 × 1024), so if the science file is smaller than full frame then only the appropriate section of the dark-count file is used. Use "imarith" or "darkx" IRAF tasks.

9.2.2 Format-Dependent Photometric Correction (ITF)

These reference files are called ITF (Intensity Transfer Function) files for historical reasons. There is one such file for each format. The format-dependent correction is applied by multiplying the image from the previous step (i.e. the dark-count subtracted image) by the appropriate ITF file. Use "imarith" IRAF task.

9.2.3 Correct For Zoom Mode

If the image was taken in zoom mode, the next step is to split the data values along the first image axis (the sample direction). The length of the first axis (NAXIS1) is doubled, and the length of the second axis (NAXIS2) is not changed. Use "dezoomx" IRAF task.

9.2.4 Relative Calibration or Flat Field Correction (normal images only)

This correction is called the uniform detective efficiency (UNI) correction, and removes the nonuniform detective efficiency of the detector. It is applied by multiplying the image by the UNI reference file (format independent) , which is the reciprocal of a flat field. The UNI files are full-frame in size, which is 1024 x 1024 because it is dezoomed. As with the dark-count correction, if the science image is smaller than full-frame then only a subset of

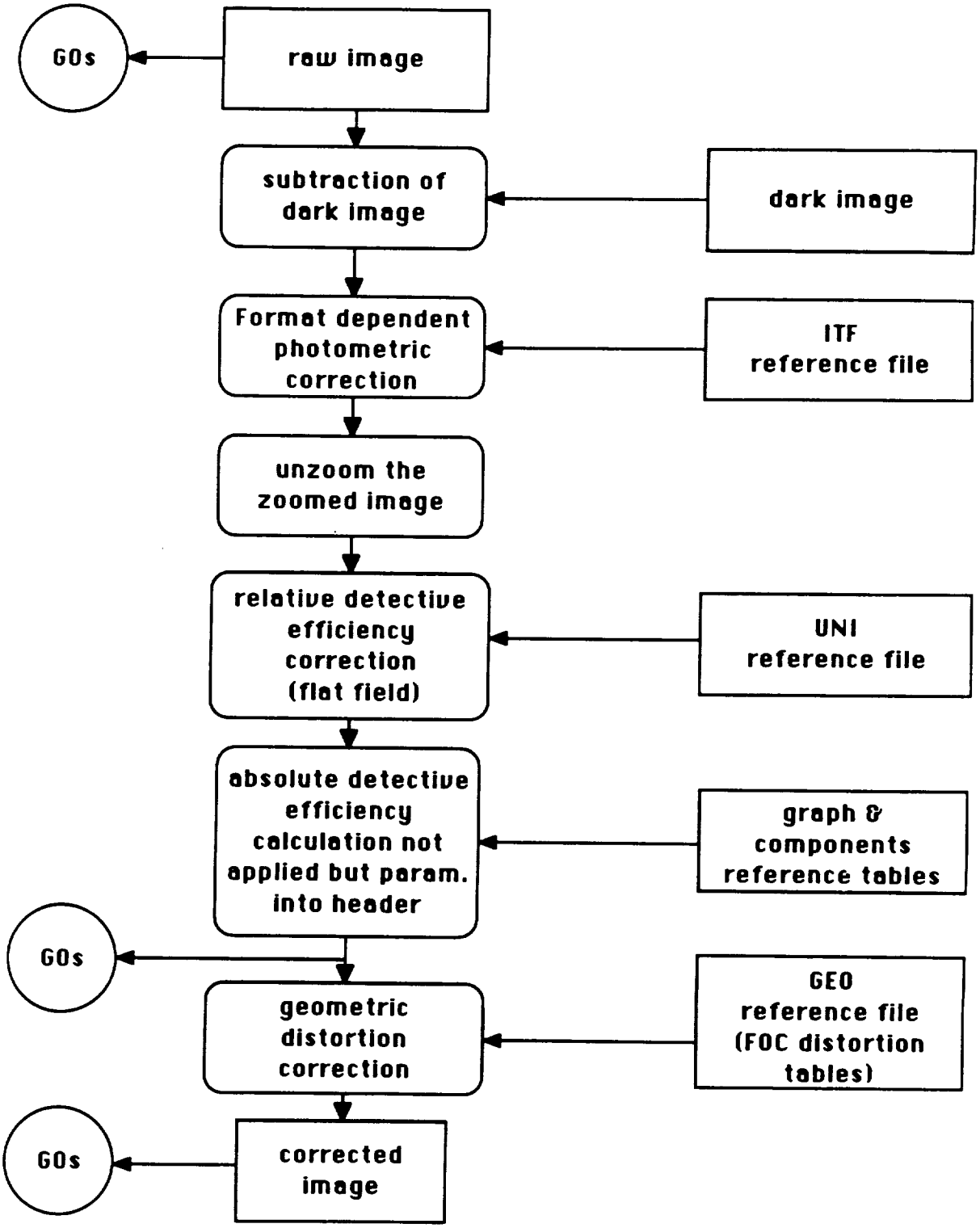

Figure 46. Flow diagram of FOC imaging data through the Routine Science Data Processing System.

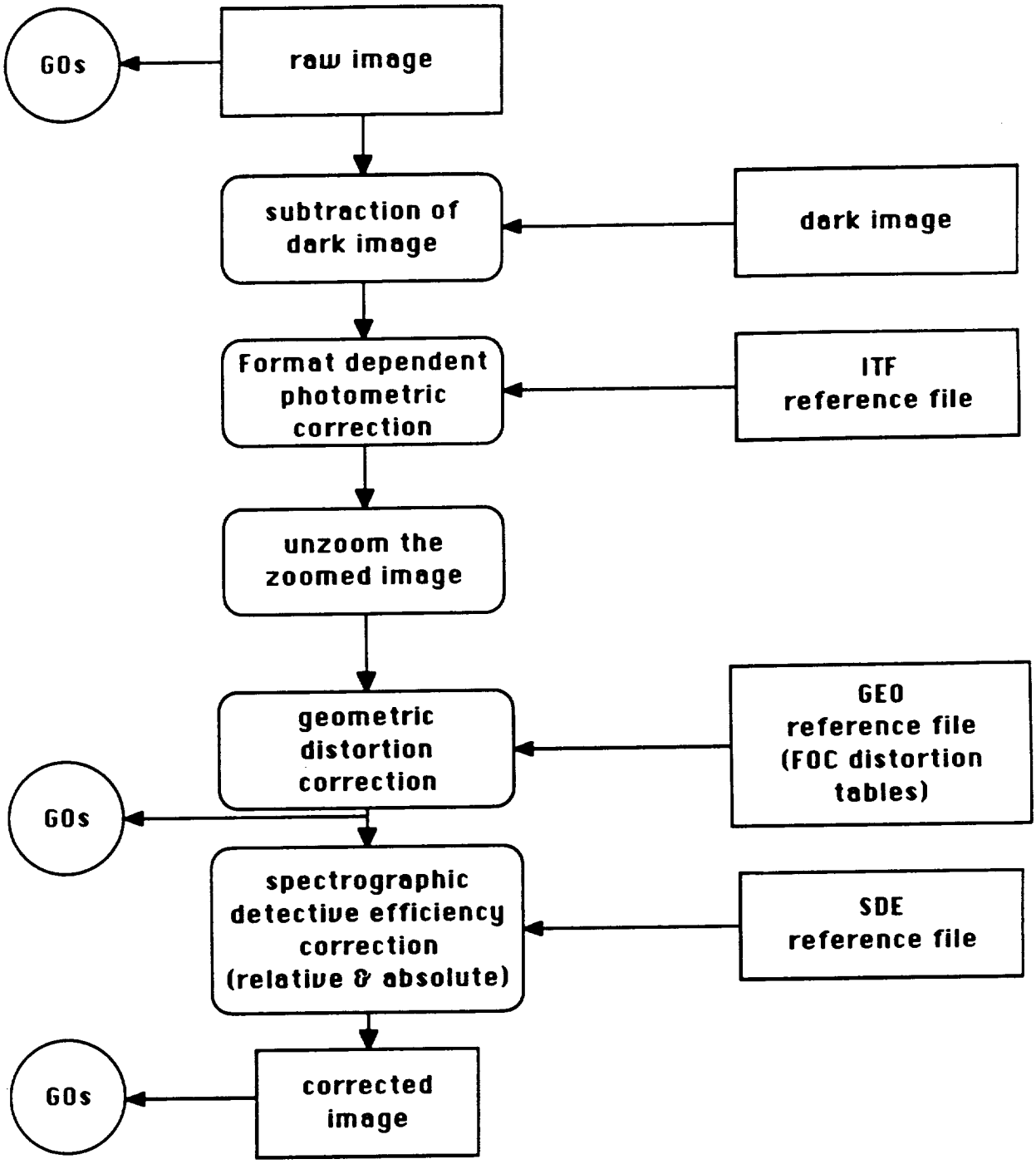

Figure 47. Flow diagram of FOC spectrograph data through the Routine Science Data Processing System.

the UNI file is used. Since the sensitivity of the detector depends on wavelength, six different UNI files are provided for different wavelengths. For the F/48 configuration, lambda = 2000 and 4800 angstroms are provided; for F/96 configuration, lambda = 2000, 4800, 5600, and 6600 angstroms are provided. The file to select is determined by comparing wavelengths of the UNI files with the pivot wavelength of the optical mode. Use "imarith" IRAF task.

9.2.5 Compute Absolute Sensitivity

This does not affect the data values. The inverse sensitivity, pivot wavelength and RMS bandwidth of the optical mode selected are computed and stored in the header of the output image. The zero-point magnitude and the observation mode are also saved in the output header. Multiplying the data numbers in the image by the value of the header parameter PHOTFLAM and dividing by the exposure time converts to flux density F in units of ergs per square centimeter per second per angstrom. Use "evalband" IRAF task.

9.2.6 Geometric Correction

A raw FOC image is distorted by a few percent for two reasons, the optics and the detector. Both distortions are comparable in magnitude. The optical distortion was computed by ray tracing, and the detector distortion is measured by taking flat-field images and observing the positions of reseau marks that are uniformly spaced on the photocathode. A geometric correction reference file includes both optical and detector distortion. It consists of two sets of positions: a uniform grid of reference positions (*i.e.*, on the plane of the sky) and the positions as observed in the raw FOC image. Once the positions have been corrected, the second step of the geometric correction involves the flux conservation. The reseau mark file, which maps the distortion, is used in order to establish a link between the position of a pixel in the input (distorted) image with its position in the output (undistorted) image. Count values are interpolated from neighbouring pixels, and then the counts are corrected using the jacobian of the distortion. Use "geomcorrx" IRAF task.

9.2.7 Spectrographic Detective Efficiency Correction

The SDE correction is only applied to spectrographic images. It includes both the flat-field correction and a conversion from counts to flux density. It is applied after geometric correction because the absolute sensitivity depends on wavelength, and a major function of the geometric correction for spectrographic images is to align the spectrum with the axes and set the dispersion. The correction is applied by multiplying by a spectrographic detective efficiency reference file. The use of an order-selecting filter can change the location of a given wavelength on the photocathode, so there are several reference files; the appropriate one is selected based on the filters used. These files are full-frame (1024 $\times$ 1024), so only a subset will be used if the science image is smaller than this. Use "imarith" IRAF task.

10.0 ACKNOWLEDGEMENTS

This handbook could not have been written without the expert advice and assistance of my colleagues on the FOC team at the ST ScI. In particular, I am indebted to A. Nota, D. Baxter, P. Hodge, W. Sparks, N. Towers, M. Miebach, G. Meylan, P. Greenfield, R. Jedrzejewski, D. Schertl and Th. Reinheimer for supplying me with much of the information presented here.

The FOC has been brought to its present status by the devoted efforts of many groups including the ESA/ST Project Office Staff, the FOC Investigation Definition Team (IDT) and various industrial contractors (especially British Aerospace, Matra-Espace and Dornier System GmbH). The author is particularly grateful to a number of people in these and other organizations that gave generous amounts of their time to assist me in producing this handbook. These are, in particular, the entire IDT, M. Anderegg, R. Laurance, H. Schroeter, R. Thomas, M. Verdant, and T. Westrup of ESA, S. di Serego Alighieri and Richard Hook of ST/ECF,M. Saisse of the LAS/Marseille, P. Amadieu and C. Fayard of Matra-Espace, W. Mill of Dornier, D. Giaretta of RAL, J. Evans, and R. Bushell of British Aerospace, and my colleagues P. Bely, J. Bohlin, C. Burrows, C. Cacciari, J. Crocker, O. Lupie, A. Pickles, and M. Rafal at the ST ScI. I am also very grateful for the patient and expert editorial assistance of R. Miller and D. Whitman.

The FOC/IDT members are:. R. Albrecht, C. Barbieri, J. C. Blades, A. Boksenberg, P. Crane, J. M. Deharveng, M. Disney, H. C. v. d. Hulst, P. Jakobsen, T. Kamperman, I. R. King, F. Macchetto (Principal Investigator), C. D. Mackay, F. Paresce, and G. Weigelt.

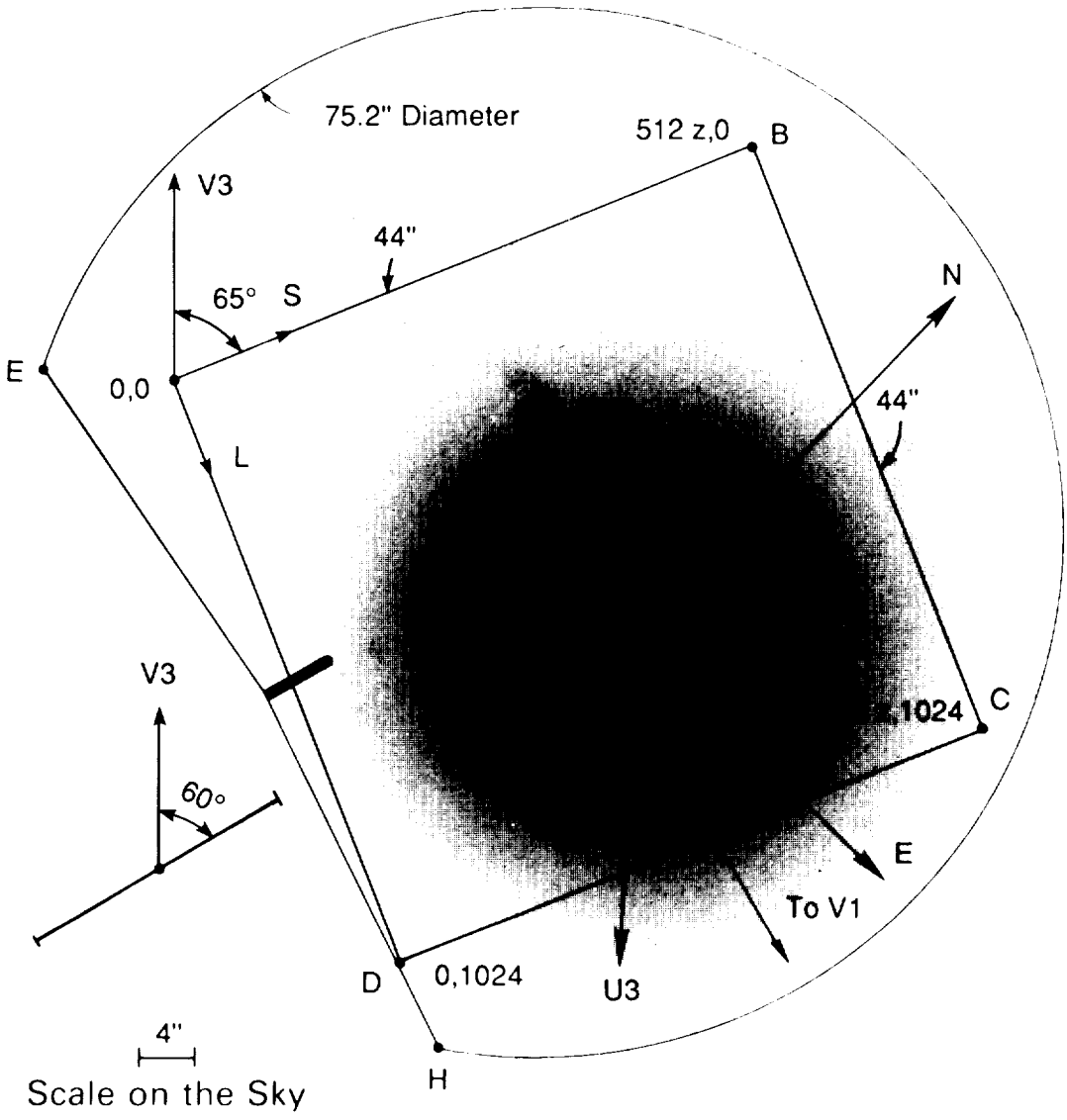

Figure A1. Area of the sky around M87 imaged through a V filter superimposed on which is the F/48 extended aperture oriented such that the jet lies along –L direction.

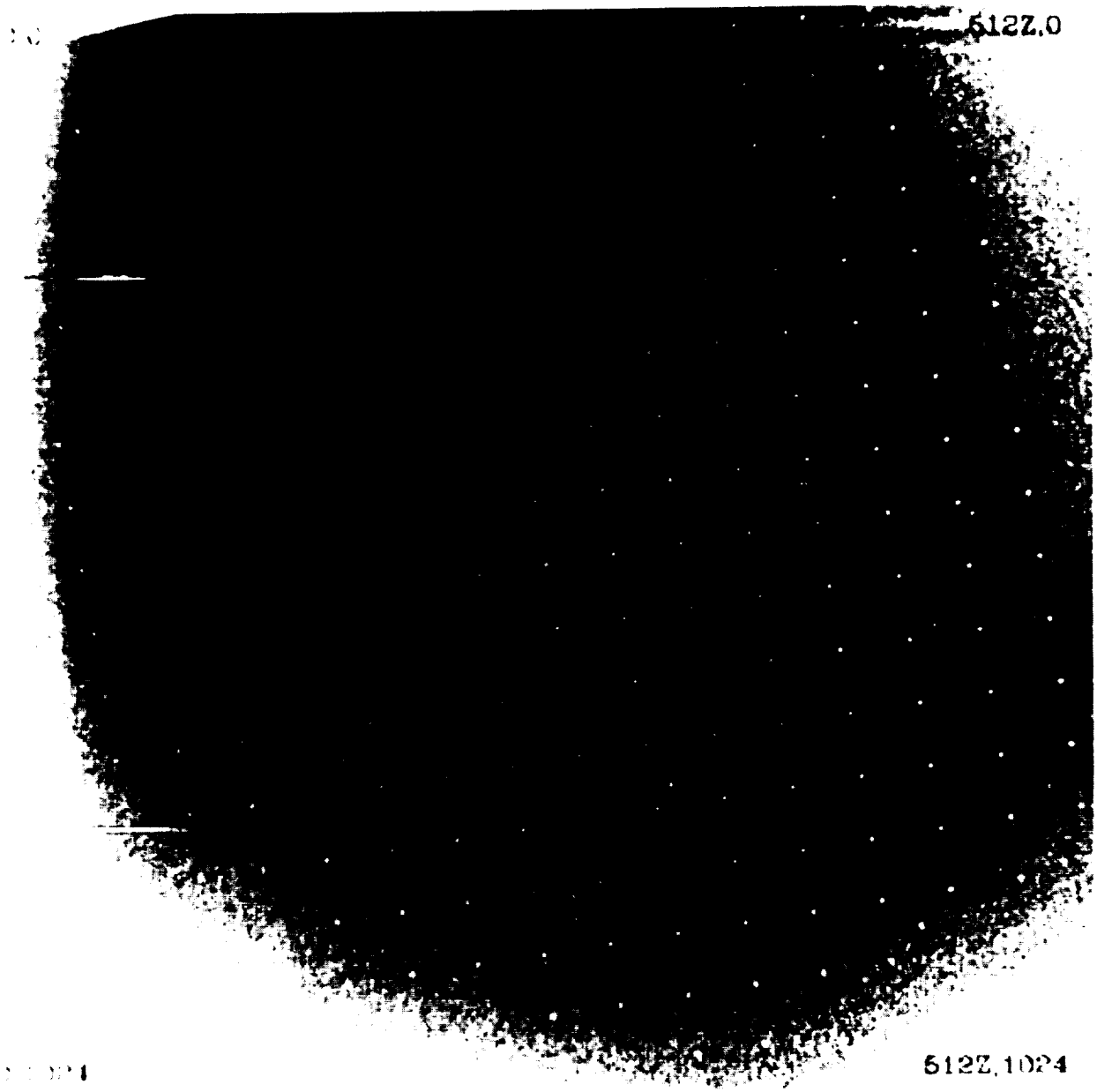

Figure A2. Extended format ($512z \times 1024$) negative image taken with the F/48 relay under uniform external illumination. The slit finger is just visible at the left center edge. Every other line L of the image is not displayed to fit in the 512×512 screen.

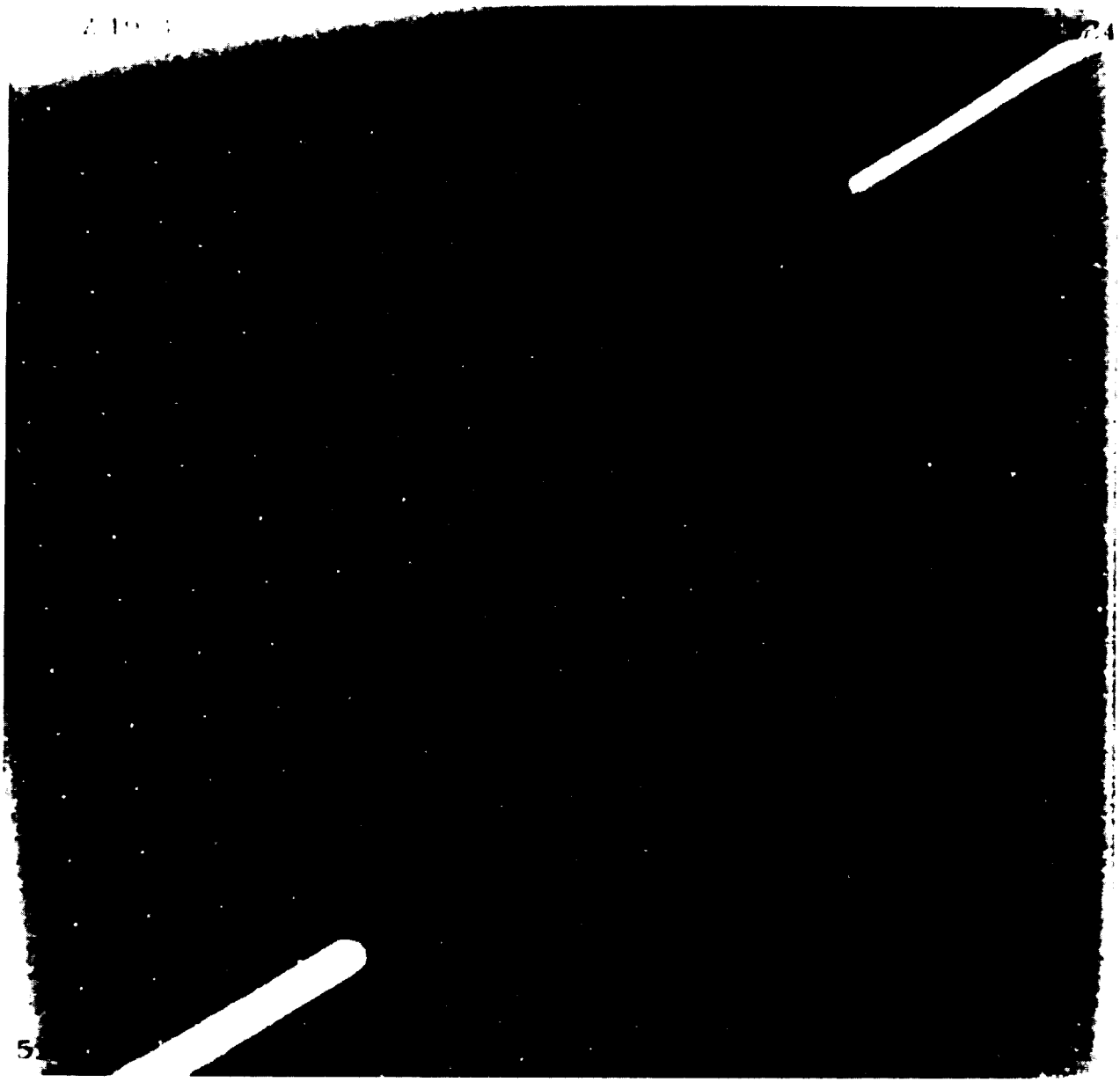

Figure A3. Extended format ($512z \times 1024$) negative image taken with the F/96 relay under uniform external illumination. The occulting fingers and clipping of the frame due to the baffle are clearly visible. Every other line L of the image is not displayed to fit in the 512×512 screen.

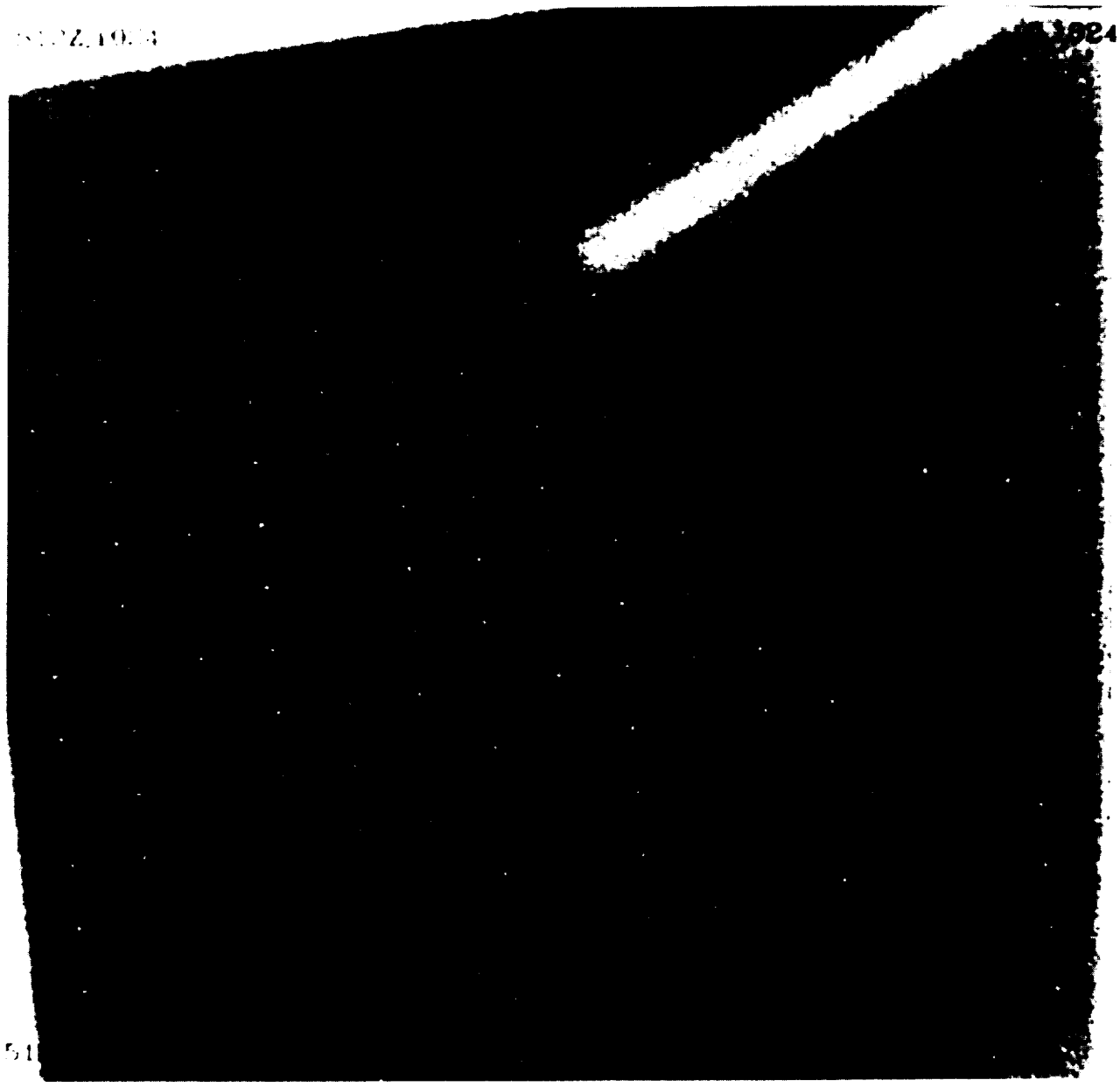

Figure A4. Extended format ($512z \times 1024$) negative image taken with the F/288 relay under uniform external illumination. The 0.4 arcsecond finger is visible in the upper right corner. Every other line L of the image is not displayed to fit in the 512×512 screen.

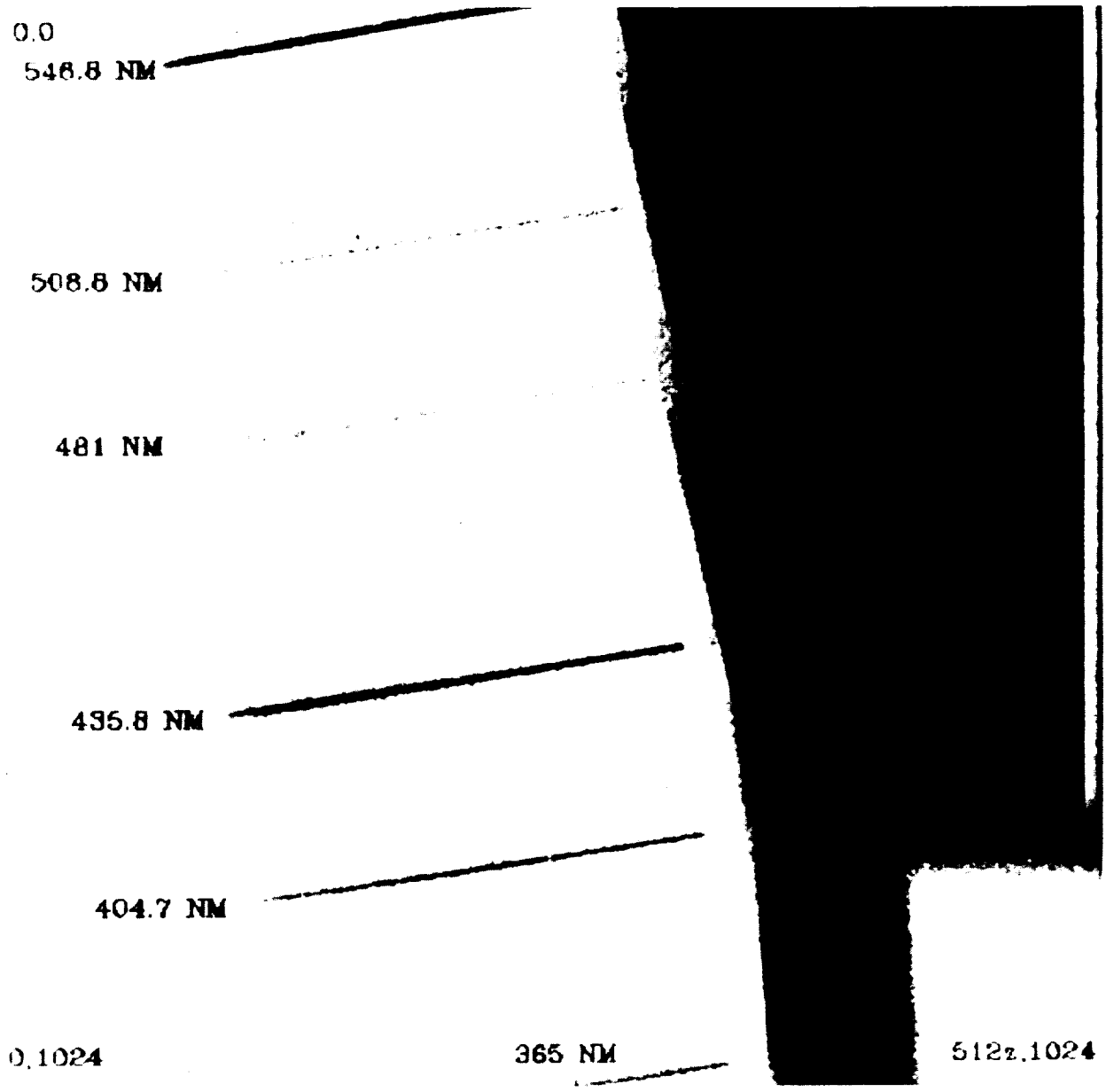

Figure A5. Extended format ($512z \times 1024$) negative image taken with the F/48 relay in spectrograph mode under uniform external illumination by a Hg vapor lamp. Every other line L of the image is not displayed to fit in the 512×512 screen.

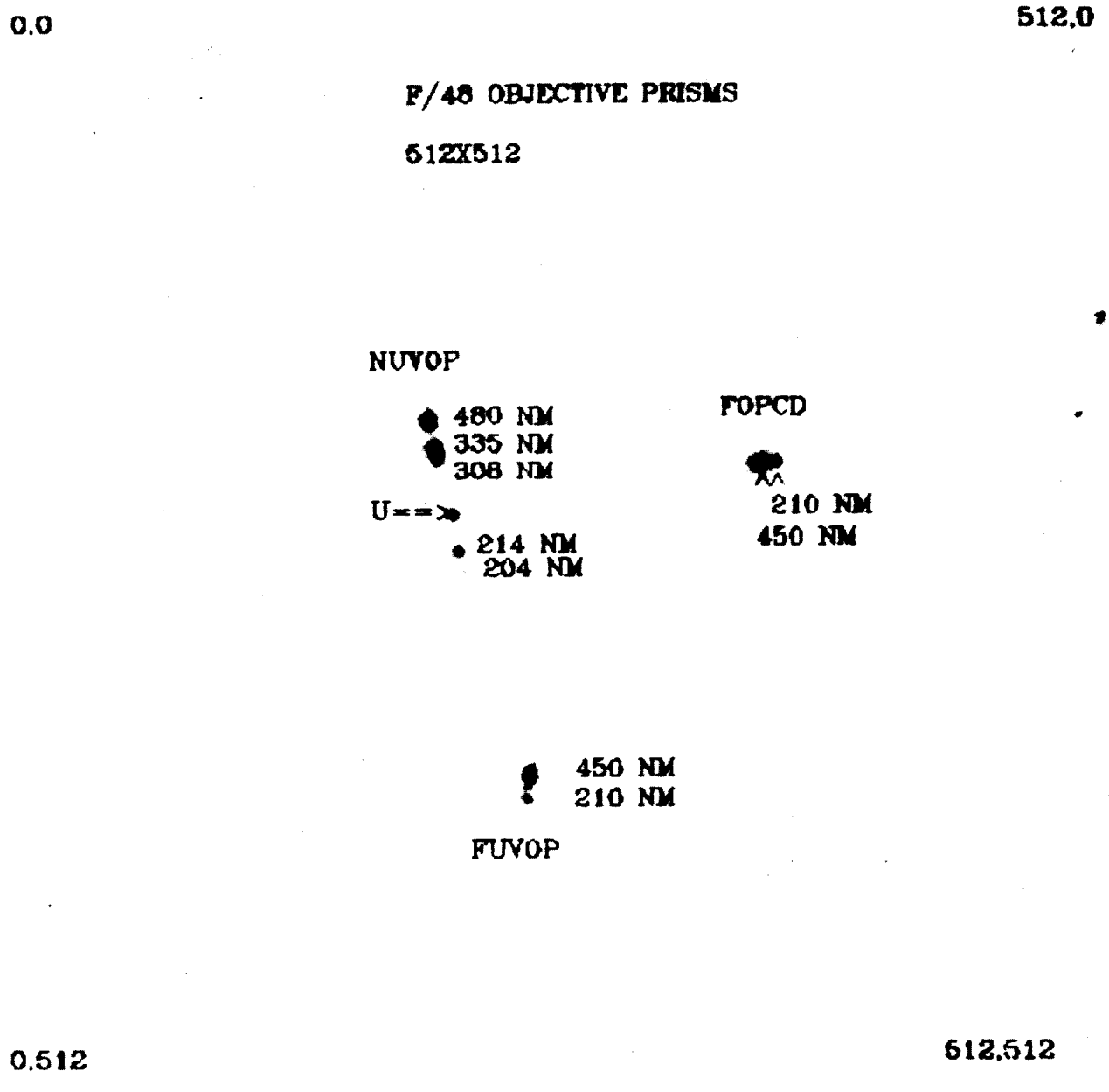

Figure A6. Extended ($512z \times 512$) negative image of the F/48 objective prism spectral configurations for a star located at U (undispersed position) with external point source illumination provided by a Zn line emission lamp. Measurements made in air ($\lambda > 2000$Å).

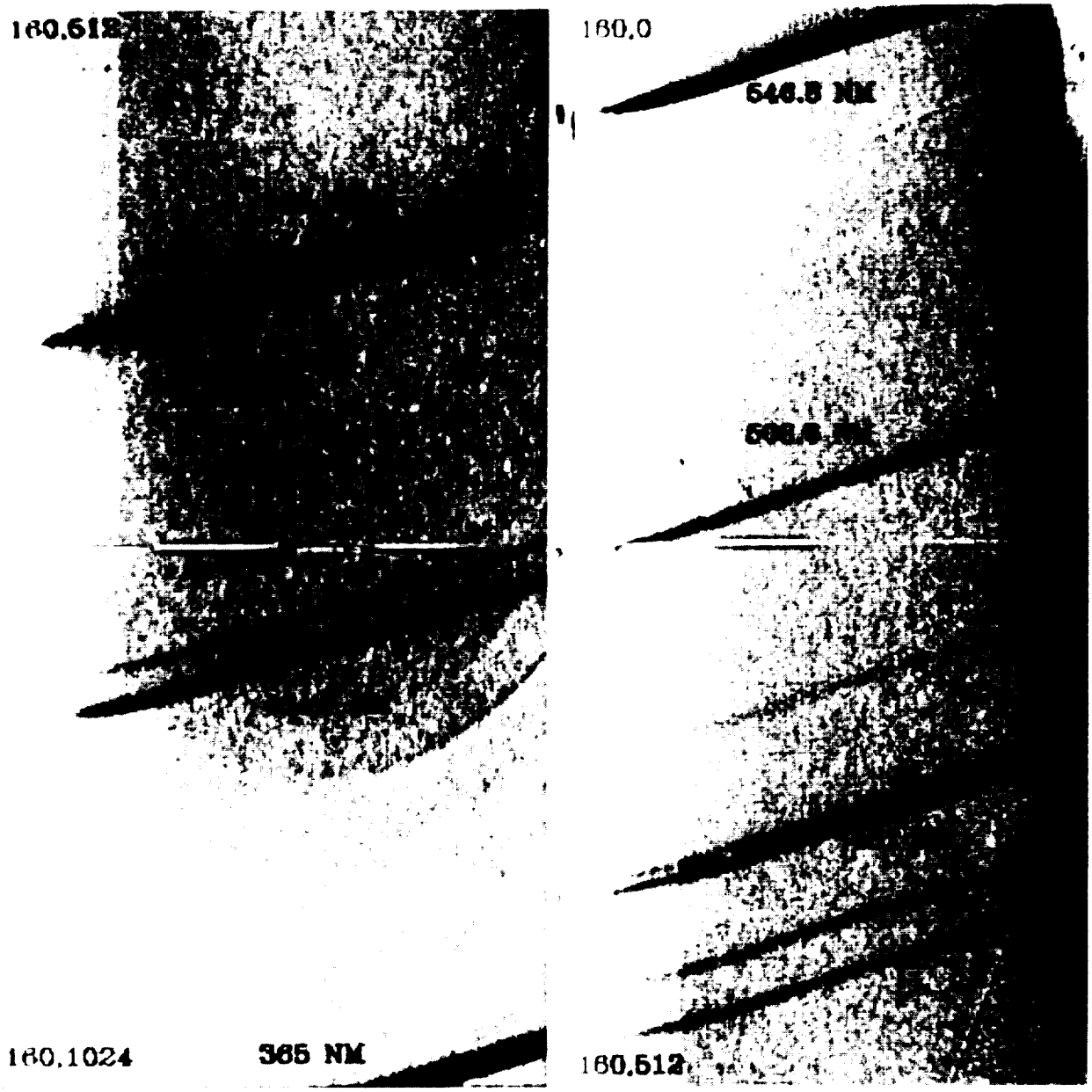

Figure A7. Standard F/48 spectrograph ($256z \times 1024$) format negative image under uniform external illumination by a Hg vapor lamp. The right half of the image corresponds to the first 512 lines ($L = 0 - 512$) while the left half corresponds to the last 512 lines ($L = 512 - 1024$). The spectrum is the same as that shown in Figure A5.

Figure A8. Negative images of M51 taken with the F/48 relay at various linearized intensity levels of the nucleus ranging from 0.05 counts sec^{-1} $pixel^{-1}$ in the the lower left to 7.3 counts sec^{-1} $pixel^{-1}$ in the upper right.